

AD-A171 220

EFFECTS OF STRONG DIFFRACTION ON THE FOCUSING AND
SCATTERING OF ACOUSTIC WAVES(U) PENNSYLVANIA STATE UNIV
STATE COLLEGE APPLIED RESEARCH LAB

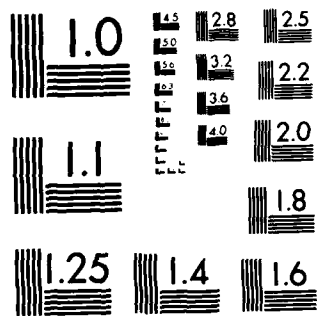
1/2

UNCLASSIFIED

T B GABRIELSON ET AL. JUN 86 TR-86-004

F/G 20/1

NL



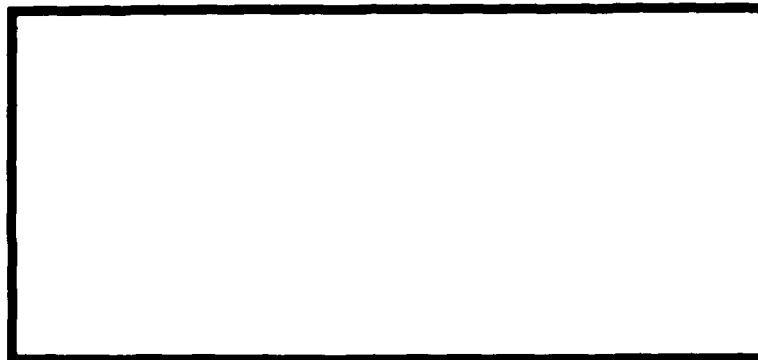
MICROCOPY RESOLUTION TEST CHART
NATIONAL BUREAU OF STANDARDS 1963-A

11



Applied Research Laboratory
The Pennsylvania State University

AD-A171 220



DTIC FILE COPY

DTIC
SELECTED
AUG 23 1986
S E

has been approved
for sale; its
distribution is unlimited.

ARLPSU

TECHNICAL REPORT

The Pennsylvania State University
Intercollege Research Programs and Facilities
APPLIED RESEARCH LABORATORY
P. O. Box 30
State College, PA 16804

EFFECTS OF STRONG DIFFRACTION ON THE FOCUSING
AND SCATTERING OF ACOUSTIC WAVES

by

T. B. Gabrielson, S. T. McDaniel,
D. W. Thomson

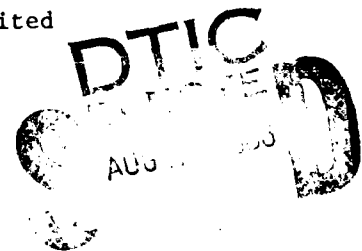
Technical Report TR 86-004

June 1986

Supported by: Naval Scientific Technical
Exchange Program

L. R. Hettche, Director
Applied Research Laboratory

Approved for public release; distribution unlimited



UNCLASSIFIED

SECURITY CLASSIFICATION OF THIS PAGE

REPORT DOCUMENTATION PAGE

1a. REPORT SECURITY CLASSIFICATION UNCLASSIFIED			1b. RESTRICTIVE MARKINGS		
2a. SECURITY CLASSIFICATION AUTHORITY			3. DISTRIBUTION/AVAILABILITY OF REPORT		
2b. DECLASSIFICATION/DOWNGRADING SCHEDULE					
4. PERFORMING ORGANIZATION REPORT NUMBER(S)			5. MONITORING ORGANIZATION REPORT NUMBER(S)		
6a. NAME OF PERFORMING ORGANIZATION Applied Research Laboratory Penna. State University		6b. OFFICE SYMBOL (If applicable) ARL	7a. NAME OF MONITORING ORGANIZATION		
6c. ADDRESS (City, State, and ZIP Code) P. O. Box 30 State College, PA 16804			7b. ADDRESS (City, State, and ZIP Code)		
8a. NAME OF FUNDING/SPONSORING ORGANIZATION		8b. OFFICE SYMBOL (If applicable)	9. PROCUREMENT INSTRUMENT IDENTIFICATION NUMBER		
8c. ADDRESS (City, State, and ZIP Code)			10. SOURCE OF FUNDING NUMBERS		
			PROGRAM ELEMENT NO.	PROJECT NO.	TASK NO.
			WORK UNIT ACCESSION NO.		
11. TITLE (Include Security Classification) Effects of Strong Diffraction on the Focusing and Scattering of Acoustic Waves (Uncl.)					
12. PERSONAL AUTHOR(S) T. B. Gabrielson, S. T. McDaniel, D. W. Thomson					
13a. TYPE OF REPORT Technical		13b. TIME COVERED FROM _____ TO _____		14. DATE OF REPORT (Year, Month, Day) June 1986	
				15. PAGE COUNT 162	
16. SUPPLEMENTARY NOTATION					
17. COSATI CODES			18. SUBJECT TERMS (Continue on reverse if necessary and identify by block number)		
FIELD	GROUP	SUB-GROUP	acoustics, wave propagation, diffraction, finite-difference, asymptotic, ray theory, nomal-mode		
19. ABSTRACT (Continue on reverse if necessary and identify by block number) In many wave propagation problems, diffraction is considered to be a second order effect that diffuses the sharp shadows and focal surfaces predicted by ray theory. However, if the frequency is low enough so that the wavelength is comparable to the size of the focusing region, structured fields of significant level can be found in classical shadows and smooth, featureless enhancement can replace the sharp, multiple convergences common at higher frequencies. This study examines the effects of strong diffraction on refractive focusing of acoustic waves. In addition, signal fluctuations caused by perturbations of the refractive index are considered where the spatial extent of a particular perturbation "patch" is comparable to the wavelength. Consequently, the perturbation mechanism is primarily diffractive also.					
20. DISTRIBUTION/AVAILABILITY OF ABSTRACT <input type="checkbox"/> UNCLASSIFIED/UNLIMITED <input type="checkbox"/> SAME AS RPT. <input type="checkbox"/> DTIC USERS			21. ABSTRACT SECURITY CLASSIFICATION		
22a. NAME OF RESPONSIBLE INDIVIDUAL			22b. TELEPHONE (Include Area Code)		22c. OFFICE SYMBOL

In order to study these strong diffraction effects, several tools are developed. A range-dependent finite-difference solution to the time-dependent wave equation is constructed. By driving this model with a time-limited pulse, the frequency response over more than a decade is given automatically at each grid point. Also, a method based on range-dependent normal-mode theory is developed that leads to a simple interpretation of the signal fluctuations and the underlying field structure. Two other methods used for auxiliary tests are introduced: a second-order asymptotic correction to ray theory for regions of multiple focusing and an integral solution for time-dependent diffraction by a two-dimensional wedge.

By using both the finite-difference model and the normal-mode model, the field structure in the shadow zone is determined to be the result of interference between several distinct mode groups that represent diffractive spreading of classical rays. While these interfering components are roughly equal in magnitude in the shadow, a single dominant component is isolated in the enhancement region between focal surfaces. As a result, there is little spatial variation in the field in the enhancement region while the variation in the shadow is quite rapid. A simple two-component model is developed for the purpose of describing signal fluctuations. This model successfully describes the relative insensitivity to fluctuation in the strong enhancement region while at the same time describing the strong level changes and fades in the shadow.

FOREWORD

This report presents the results of independent reseach conducted by T. B. Gabrielson in partial fulfillment of the requirements for a doctoral degree in Acoustics at The Pennsylvania State University. Drs. McDaniel and Thomson co-advised Dr. Gabrielson's research. This manuscript is issued as an ARL Technical Report to provide ready access to a wide audience.

Accession For	
NTIS GPO&I	<input checked="" type="checkbox"/>
DTIC TAB	<input type="checkbox"/>
Unannounced	<input type="checkbox"/>
Justification	
By	
Distribution/	
Availability Codes	
Dist	Avail and/or Special
A-1	



TABLE OF CONTENTS

ABSTRACT	i,11
LIST OF FIGURES	v
ACKNOWLEDGEMENTS	viii

<u>Chapter</u>	<u>page</u>
I. INTRODUCTION	1
II. SOLUTIONS FOR THE FIELD NEAR A COMPLEX FOCUS	7
2.1 Governing Equations	7
2.2 Normal-mode Methods	10
2.2.1 Simple two-layer model	10
2.2.2 Matrix iteration method	14
2.3 Asymptotic Approximations	15
2.3.1 Simple caustic	20
2.3.2 Multiple caustic	22
III. METHODS FOR RANGE-DEPENDENT PERTURBATIONS	24
3.1 Field Solutions	24
3.1.1 Single-frequency (CW) techniques	24
3.1.2 Time-dependent solutions	25
3.1.3 Direct finite-difference solutions	28
3.2 Special Methods for Fluctuations	36
3.2.1 Homogeneous isotropic turbulence models	38
3.2.2 Strength and diffraction parameters for fluctuations	39
3.2.3 Range-dependent Normal-mode Theory	44
IV. VALIDATION OF FINITE-DIFFERENCE SOLUTION	48
4.1 Boundary Conditions and Source Diffusion	48
4.2 Corner Diffraction	51
4.2.1 Integral solution for diffraction by a wedge	51
4.2.2 Comparison with finite-difference model	58
4.3 Focusing at Simple and Cusped Caustics	60
4.4 Limitations of the Finite-difference Solution	63
V. SOLUTION CONTEXT	64
5.1 Focusing in the Planetary Boundary Layer	65
5.1.1 Effects of wind on sound speed	65
5.1.2 The planetary boundary layer	67

5.2	Perturbation Model	71
5.3	Source characteristics	77
5.4	Configuration for the PBL Model	78
VI.	STRUCTURE OF THE UNPERTURBED FIELD	82
6.1	Overall Field Structure	82
6.2	Structure in the Shadow Zone	88
6.2.1	Finite-difference results	88
6.2.2	Cumulative mode-sum analysis	90
6.2.3	Asymptotic analysis	95
6.3	Structure of the Multiple Caustic	97
6.3.1	Mode-sum analysis	97
6.3.2	Asymptotic analysis	99
6.4	Structure near the Cusp	101
VII.	SIGNAL FLUCTUATIONS	104
7.1	Calculated Fluctuations	105
7.1.1	Time history of received levels	106
7.1.2	Normalized fluctuation magnitude	111
7.2	Mode Analysis of Fluctuations	113
7.2.1	Equivalent fluctuation magnitude	114
7.2.2	Modal analysis	117
7.3	Two-component Model	126
7.3.1	Predictions at saturation	129
7.3.2	Predictions below saturation	134
7.4	Correspondence to Fluctuation Parameters	136
VIII.	CONCLUSIONS	142
	REFERENCES	148
 <u>Appendix</u>		
A.	TRANSPARENT-BOUNDARY CONDITION	152
B.	GRADIENT SCALING	153

LIST OF FIGURES

<u>Figure</u>	<u>page</u>
1. Sound-speed profile for two-layer normal-mode model	12
2. Typical plot of range as a function of wave number for rays near two closely-spaced caustics	17
3. Prediction of reflected pressure waveform from impulse incident to a one-dimensional gradient layer	26
4. Interior grid point and nearest neighbors for finite- difference calculation	30
5. Apparent phase speed ratio c^*/c as a function of the angle of the wavefront normal with respect to horizontal	34
6. Phase speed ratio c^*/c as a function of normalized grid spacing for $\beta = 0.4$	35
7. Comparison of the dissipation and dispersion characteristics of the finite-difference method, the weighted-characteristics method, and a predictor-corrector method	37
8. Level predicted by finite-difference calculation relative to free-field spreading for a constant sound-speed channel with transparent boundaries	50
9. Geometry for the two-dimensional wedge problem	52
10. Diffraction into the shadow of a pressure-release wedge	59
11. Comparison of finite-difference and normal-mode solutions	62
12. Measured temperature and wind speed profiles for a period of strong focusing in the planetary boundary layer	70
13. Sound-speed profile corresponding to temperature and wind speed profiles in figure 12	72
14. Ray diagram for sound-speed profile in figure 13	73
15. Location of ray-theory caustics and groups of observation points	74

16. Vertical distribution of normalized perturbation component u/\hat{u}	76
17. Field in the vicinity of the multiple caustic (5Hz)	84
18. Field in the vicinity of the multiple caustic (10Hz)	85
19. Field in the vicinity of the multiple caustic (20Hz)	86
20. Finite-difference model predictions of pulse shape at receiver points 1 through 7 in shadow region	89
21. Spectra corresponding to the waveforms shown in figure 20 . . .	91
22. Mode-sum plots (20Hz) for points 2, 3, 4 and 5 in the shadow region	93
23. First-order asymptotic correction compared to spectra from finite-difference model at points 4 and 7 in the shadow region	96
24. Mode-sum plots (20Hz) for points 1, 3, 5 and 7 in the inter-caustic zone	98
25. Prediction of field level at 20Hz by second-order asymptotic correction to ray theory	100
26. Mode-sum plots (20Hz) for points 1, 2, 3 and 4 in the cusp region	103
27. Signal level fluctuations at point 1 in the inter-caustic zone	107
28. Signal level fluctuations at point 5 in the inter-caustic zone	108
29. Signal level fluctuations at point 2 in the shadow region . .	109
30. Signal level fluctuations at point 5 in the shadow region . .	110
31. Fluctuation magnitude computed by the finite-difference method at 2, 5, 10 and 20Hz	112
32. Comparison between fluctuation magnitudes at 5 and 20Hz as computed by the finite-difference model and by eigenvalue shift	116
33. Perturbation weight function for the normal-mode solutions at points 1 and 5 in the inter-caustic zone (5Hz)	120

34. Perturbation weight function for the normal-mode solutions at points 1 and 5 in the inter-caustic zone (20Hz)	121
35. Perturbation weight function for the normal-mode solutions at points 1 and 5 in the inter-caustic zone (50Hz)	122
36. Relative excitation of 5Hz modes for receiver at the altitude of the inter-caustic region points	124
37. Relative excitation of 20Hz modes for receiver at the altitude of the inter-caustic region points	125
38. Relative excitation of 20Hz modes for receivers at points 2 and 5 in the shadow region	127
39. Prediction of fluctuation magnitude at saturation by two-component model	131
40. Fluctuation magnitude calculations by the two-component model and by the complete eigenvalue-shifted mode sum at 20Hz	133
41. Fluctuation magnitude calculations by the two-component model and by the complete eigenvalue-shifted mode sum at 5Hz	135
42. Fluctuation diffraction parameter Δ computed by standard form and by caustic-extended calculation	138
43. Δ - ϕ space showing range of fluctuation parameters encountered in this investigation	139

ACKNOWLEDGEMENTS

One of the authors (TBG) wishes to acknowledge partial support by the Naval Scientific Technical Exchange Program. He also wishes to thank Drs. R. E. Llorens, S. I. Hayek, A. D. Stuart, A. B. Coppens and J. Sanders for a careful review of the manuscript.

Chapter I

INTRODUCTION

In many wave propagation problems, diffraction is considered to be a second-order effect that diffuses the sharp shadows and focal surfaces of ray theory. However, if the frequency is low enough so that the wavelength is comparable to the size of the focusing region, structured fields of significant levels can be found in classical shadows and smooth, featureless enhancement can replace sharp, multiple convergences common at higher frequencies.

This investigation examines strong diffraction in regions of complex refractive focusing by quantitative analysis of low-frequency wave propagation. Focal surfaces form because of gradients in the refractive index such as are common in the atmosphere or the ocean (either for acoustic or electromagnetic waves) and the frequency range considered is such that the wavelength is of the same order as the separation of these surfaces.

Most of the work done on acoustic (or electromagnetic) focusing has been in simple cases where normal-mode expansion (Ewing, et al., 1957) is practical or asymptotic methods (Sachs and Silbiger, 1971) can be used. Long-wavelength focusing in inhomogeneous media has been avoided for good reason: if the wavelength is comparable to some characteristic length, the wave nature of the field dominates and neither small nor large value asymptotic approximations are useful.

While analysis of long-wavelength focusing can be difficult, the phenomenon is not uncommon either in ocean acoustics (Brekhovskikh and Lysanov, 1982) or atmospheric acoustics (Thomson, 1983). Furthermore, when conditions exist for long-wavelength focusing, the effects of perturbations on signal fluctuations can be primarily diffractive. The usual multiple scattering theories assume that the spatial scale of the perturbations is either much smaller or much larger than a wavelength (for example, Skudrzyk, 1957 or Flatte, 1979). In the present analysis, the perturbation scale is of the same order as the acoustic wavelength and so these limiting cases are not applicable. Since very little analysis of strong diffraction effects has been done either for deterministic focusing or for perturbation-induced fluctuations, this research considers both phenomena.

Three critical areas are considered: long-wavelength focusing, signal fluctuations caused by perturbations in sound speed, and the transition in fluctuation strength from small amplitude variation to a large, but limiting, amplitude fluctuation. Normally, the degree of signal fluctuation is related to the sound-speed variation introduced by the perturbations. There comes a point, however, when the wavefront has become so distorted that maximum phase interference is taking place and increased perturbation only relocates the interference minima and maxima. This is termed the saturation regime and is the subject of the last area of consideration.

Deterministic propagation and signal fluctuation are usually considered separately, but the common theme of strong diffraction suggests that they be treated together. If unperturbed focusing phenomena were

the only interest of this investigation, the problem could be cast in nondimensional terms. Perturbations, however, are peculiar to the particular physical problem. To treat realistic values of perturbation scale, strength, and rate of change, a simple physical situation is modeled. Thomson (1983) has shown that strong focusing can occur in the planetary boundary layer and Brown (1980) and Thomson have provided a detailed set of meteorological measurements in connection with noise interference studies of the DOE/NASA wind turbine generator near Boone, North Carolina. This example provides an excellent basis for the present studies in long-wavelength focusing and scattering but the methodology and many of the results are applicable to strong diffraction problems in general. Other examples include long-range refractive focusing of acoustic waves by temperature gradients in the thermosphere, short- and long-range focusing of sound in the ocean, and ionospheric refraction of very low frequency electromagnetic radiation.

Several tools were developed specifically for this investigation. Much of the analysis of the unperturbed field is performed using a normal-mode solution based on standard theory (for example, Ewing, et al., 1957); however, because as many as 4000 modes must be calculated in some instances, a very efficient eigenvalue search procedure was required. Consequently, a matrix estimation scheme introduced by Cooney, et al. (1981) for locating bound-state energy levels for the time-independent Schrodinger equation is adapted to drive an iterative search procedure. The resulting technique is reliable and fast.

Since the focal surfaces or caustics are closely spaced in terms of the acoustic wavelength, the usual first-order asymptotic correction to

ray theory for a simple caustic produces a very poor approximation to the actual field. This failure prompted the development of a second-order correction that not only handles the multiple focus well but also provides a criterion for deciding when the second-order scheme should be used and, also, when the detailed structure of a multiple focus will be seen.

In order to solve for the perturbed field, a range-dependent solution must be used. This requirement, along with the desire to investigate the nature of the field over a broad range of frequencies, motivated the development of a finite-difference approximation for the time-dependent acoustic wave equation. By using time-limited pulses, radiation conditions are easily satisfied and the frequency response over more than a decade is given at every one of the grid points. This particular technique introduces no artificial dissipation and a modification suggested by Vichnevetsky and Bowles (1982) makes the numerically-induced dispersion controllable and virtually independent of grid orientation. Of the range-dependent techniques used here, the finite-difference method is the most accurate so it is used as a baseline against which the other methods are compared.

Since this finite-difference method has not been applied previously to time-dependent acoustic propagation problems, some effort is spent to verify the results. During this validation process, a new solution for time-dependent wedge diffraction in two dimensions was developed. The solution is based on the method of normal coordinates outlined by Biot and Tolstoy (1957) but the usual sum of Legendre functions of non-integer degree has such poor convergence that even 30 decimal-digit preci-

sion is inadequate to calculate it except in very special cases. Here, an integral transformation is introduced and the result is a simple and rapidly convergent integral of elementary functions instead of a summation of special functions. This wedge solution is used to evaluate the finite-difference method for diffraction into a shadow. Several other tests are performed to evaluate the boundary conditions, source treatment, and refraction treatment.

Some of the more important results from the analysis of the unperturbed field concern the underlying field structure. For example, there is a definite interference structure in the shadow zone. Here, diffractive spreading from classical rays on the illuminated side of the caustic and the evanescent "tails" of low-order modes combine to produce a spatially complicated field. In contrast, in the strong enhancement region, the field is dominated by a single component and so this region is generally featureless. The transition from a highly structured multiple focus at high frequency to this smooth enhancement region at low frequency is illustrated by the behavior of the second-order asymptotic correction to ray theory. Everywhere in the field, the structure is defined by distinct groups of modes and the interference of these groups.

Once perturbations are introduced into the sound speed, the signal levels at any point fluctuate according to the reaction of the field components to these perturbations. While the fluctuations resulting from these perturbations can be calculated easily using the finite-difference method, this method gives no physical insight into the specific origins of fluctuation; therefore, an eigenvalue shift method is introduced. Based on range-dependent normal-mode theory, the eigenvalue

shift technique isolates the major effects of sound-speed perturbation by identifying the modal components of the field that are most affected by the perturbations. Coupled with a knowledge of the underlying field structure, the mechanisms of fluctuation can be determined. The important features producing the fluctuations are: the presence of a dominant mode group identified by a maximum in the eigenvalue shift function; the phase shift between this dominant component and a component consisting of the remainder of the mode sum; and, the relative magnitudes of these two components. By modeling the fluctuations as the interference of two unequal components with a changing relative phase, results very close to those of the complete eigenvalue shift solution are obtained with significantly less computational effort. This simplified two-component model gives excellent results in the region of strong enhancement and weaker but adequate agreement with the finite-difference results in the shadow zone.

Because this analysis of strong diffraction led to the development of a number of tools, the actual analysis is not considered until Chapters V through VII. The first several chapters develop these tools and establish their validity. If only a general overview of the analysis is desired, Chapters II through IV can be skipped on the first reading and referred to as necessary through the equation references in the subsequent chapters.

Chapter II

SOLUTIONS FOR THE FIELD NEAR A COMPLEX FOCUS

A region of complex focusing in which there are several areas of convergence in close proximity is particularly interesting when the frequency is sufficiently low that strong diffraction occurs. In this chapter, the basic governing equations for acoustics are briefly reviewed along with a simple normal-mode method and the usual first-order asymptotic correction to ray theory. In addition, a second-order asymptotic correction that allows calculation in the vicinity of two nearby caustics is developed. The tools described in this chapter will permit a detailed investigation of this region before adding the complications of perturbations.

2.1 Governing Equations

The equations governing the behavior of acoustic disturbances in a compressible fluid are the mass conservation equation

$$\partial \rho / \partial t + \vec{v} \cdot (\rho \vec{v}) = 0, \quad (2.1)$$

where ρ is the density and \vec{v} is the particle velocity; the equation of motion for an inviscid fluid (neglecting gravitational effects)

$$\partial \vec{v}_i / \partial t + (\vec{v}_i \cdot \vec{\nabla}) \vec{v}_i + \vec{\nabla} p_i / \rho_i = 0, \quad (2.2)$$

where p_i is the total pressure; and the isentropic relation for sufficiently slow, reversible compression and rarefaction

$$(\partial p / \partial \rho)_s = c^2, \quad (2.3)$$

where c is the sound speed.

If we express the pressure, density and particle velocity each as a static term plus a small variation (e.g., $\vec{v}_i = \vec{v}_0 + \vec{v}$) and neglect flow rotation and second-order terms, we have

$$\partial p / \partial t + \rho_0 c^2 \vec{\nabla} \cdot \vec{v} + \vec{v}_0 \cdot \vec{\nabla} p = 0, \quad (2.4)$$

and

$$\partial \vec{v} / \partial t + \vec{\nabla} p / \rho_0 + \vec{\nabla} (\vec{v}_0 \cdot \vec{v}) = 0, \quad (2.5)$$

where p is the acoustic pressure and \vec{v} is the acoustic particle velocity.

At this point, we can neglect the bulk flow \vec{v}_0 (although this will be reintroduced in Chapter V), differentiate Equation (2.4) with respect to

time, take the divergence of Equation (2.5), and subtract the results to get the usual wave equation for acoustics

$$\nabla^2 p = c^2 \partial_p^2 / \partial t^2 . \quad (2.6)$$

It is interesting to note the consequences of this last manipulation. The extra differentiation of the two coupled equations in p and \vec{v} is a mathematical artifice designed to combine them into a single equation. However, this new equation has second derivatives in both space and time whereas only first derivatives appear in the original coupled set. Consequently, discontinuities in first derivatives of physical properties are not admissible solutions to this new equation while they are perfectly acceptable in Equations (2.4) and (2.5).

In the next chapter, we will briefly consider the method of characteristics, a technique applied directly to Equations (2.4) and (2.5) (or, for that matter, to the nonlinear set of Equations (2.1) and (2.2)). The concept of propagating discontinuities in the first derivatives of the physical properties is vital to the development of signal flow in this method. Not only are discontinuous derivatives allowed but they can grow to be so large that the properties themselves approach discontinuity and form shock fronts.

Finally, the wave equation driven by a point source at z_0 is

$$\nabla^2 p = c^2 \partial_p^2 / \partial t^2 - \delta(x) \delta(z - z_0) f(t) , \quad (2.7)$$

where $f(t)$ is the source driver waveform.

2.2 Normal-mode Methods

2.2.1 Simple two-layer model

The mode solution in two-dimensions is derived by taking Fourier transforms of Equation (2.7) in both time and range and solving the resulting inhomogeneous differential equation by variation of parameters. The harmonic pressure amplitude is then given by

$$P(\omega) = i F(\omega) \sum_n \frac{u_n(z_u) v_n(z_l)}{(\partial W_{uv} / \partial \gamma)_n} \exp(i \gamma_n x) , \quad (2.8)$$

where u and v are solutions of the depth equation

$$\left[d^2/dz^2 + k^2 - \gamma^2 \right] \begin{pmatrix} u \\ v \end{pmatrix} = 0 , \quad (2.9)$$

and u , in general, satisfies the upper boundary condition while v satisfies the lower condition. The Wronskian W_{uv} of u and v is zero at each eigenvalue γ_n . (At an eigenvalue, u and v each satisfy both boundary conditions.) The source and receiver depths are renamed as the upper point z_u and the lower point z_l . In the cases to be considered here, all of the modes are completely trapped and there is no branch line integral to compute (Brekhovskikh, 1980). Evanescent modes are, however, important.

In order to study the wave structure of a focused field, a two-layer normal-mode model will be used in which the inverse of sound speed squared varies linearly with depth in each layer. In this case, the solutions to the depth Equation (2.9) are Airy functions. A typical two-layer profile is shown in Figure 1. The physical model (i.e., the model for the sound-speed profile of the atmospheric boundary layer) introduced in Chapter V matches this profile for z/H greater than zero and less than unity. Above and below this region, the sound speed is constant for the physical model (dashed line) while the profile used in the normal-mode model (solid line) is extended until the sound speed becomes infinite. The gradient of the lower layer is very small so the errors introduced by this mismatch between the physical model and the normal-mode model are negligible except for ranges well beyond those considered in this study. The errors introduced by the mismatch in the upper layer are confined to the region near the upper boundary (z/H equal to unity) and to ranges shorter than those of interest here. (For the purpose of validating the finite-difference method, the normal-mode profile is modified in Chapter IV by terminating the layers at the upper and lower boundaries with perfectly reflecting boundaries.)

Since the sound speed goes to infinity both above and below the layer interface, the depth functions u and v must decay exponentially with distance from the interface. Consequently, the solutions are

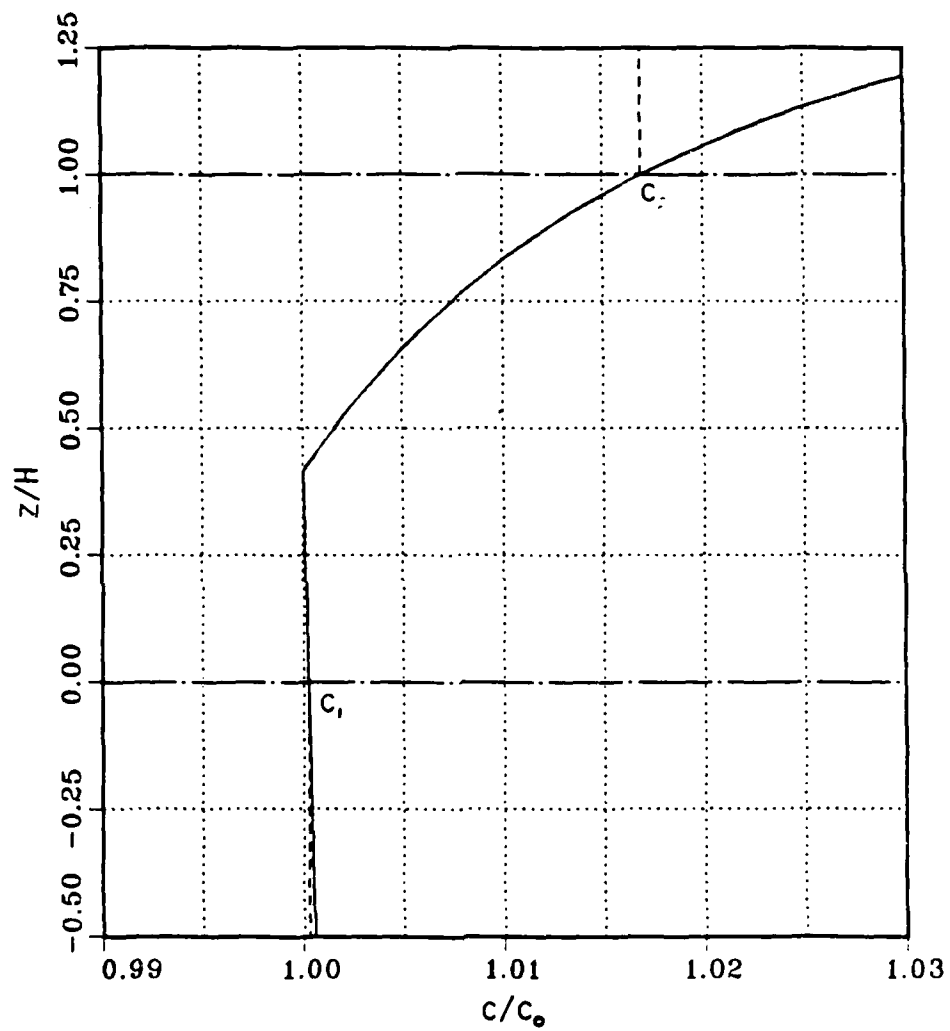


Figure 1. Sound-speed profile for two-layer normal-mode model (solid line). Profile for physical model is also shown (dashed line).

$$u(z) = \text{Ai}(Z_1) , \quad (2.10)$$

$$v(z) = \text{Ai}(Z_2) ,$$

where

$$Z_{1,2} = \eta_{1,2}(z - z_0) - (\omega^2/c_0^2 - \gamma^2)/\eta_{1,2}^2 , \quad (2.11)$$

and

$$\eta_{1,2} = (-g_{1,2}\omega^2)^{1/3} , \quad (2.12)$$

$$g_{1,2} = (1/c_{1,2}^2 - 1/c_0^2)/(z_{1,2} - z_0) .$$

The eigenvalue condition is given by setting the Wronskian of u and v to zero, or

$$\eta_2 \text{Ai}(Z_1) \text{Ai}'(Z_2) - \eta_1 \text{Ai}(Z_2) \text{Ai}'(Z_1) = 0 , \quad (2.13)$$

where the prime denotes the derivative with respect to Z .

Once the eigenvalues are located for a sufficient number of modes, the pressure can be calculated from Equation (2.8). The procedure for computing the Airy functions is discussed in detail by Gabrielson (1983).

2.2.2 Matrix iteration method

Because of the severe computational load imposed by using many single-frequency mode solutions to cover the spectrum of a single time-dependent waveform, a very efficient mode-calculation procedure is essential. Iterations to locate exact eigenvalues are, by themselves, intensive, requiring many calculations of Airy functions per mode. Furthermore, finding reasonably accurate estimates to initiate the iteration process can be just as time consuming. The popular WKB method still requires complicated calculations and can be effectively used only in single ducts.

Cooney, et al. (1981) have proposed a matrix technique for estimating the bound states of the one-dimensional Schrodinger equation. This problem is identical to mode location. By writing simple difference-equation approximations to the depth Equation (2.9) at many uniformly spaced depths, a tridiagonal system of simultaneous equations is formed. Many efficient computer algorithms exist for locating the eigenvalues of such systems so the estimation problem is rather simple. Even if the modes are degenerate or nearly so, the matrix technique locates all eigenvalues in order. It even locates evanescent-mode eigenvalues with equal ease.

Once the estimates have been computed, it is a simple matter in a single-channel profile to refine these estimates by Newtonian iteration. The Wronskian derivative is used to correct the original estimates; this derivative is also used in each term of the mode sum of Equation (2.8). The entire mode solution done in this way is fast enough to make calculation of thousands of modes practical.

Some time after this procedure was perfected, Porter and Reiss (1984) published a similar method for ocean acoustics. They estimate the eigenvalues in the same way but iterate to refine the estimates by further matrix operations. If the sound-speed profile can be approximated by some tractable functional form, Newtonian iteration is considerably faster. Even for arbitrary profiles, it may be advisable to use a correction scheme like that of Guthrie (1974) based on numerical integration of Equation (2.9) and the eigenfunction orthogonality condition.

2.3 Asymptotic Approximations

An asymptotic correction to ray theory is described by Brekhovskikh (1980) for computing the field in the vicinity of a simple caustic. The development of this correction is reviewed below in order to provide the framework for deriving a second-order correction for computing the field in the vicinity of two nearby caustics. We will follow Brekhovskikh's treatment for the first-order correction except that we will use an expression for the field in two dimensions not three. This only involves dropping a factor of the square root of horizontal distance.

The field can be written as a superposition of elementary waves as follows

$$P = \int_{-\infty}^{\infty} \phi(\gamma) \exp [i(g + \gamma x)] d\gamma, \quad (2.14)$$

where ϕ is a slowly varying amplitude factor, and g is a slowly varying phase factor. The independent variable in both cases is the horizontal wave number.

Differentiating the exponent with respect to γ , we can locate the saddle point of the integral

$$\partial g / \partial \gamma = -x, \quad (2.15)$$

so that at the saddle point

$$g = - \int x d\gamma. \quad (2.16)$$

Consequently, one way of finding g is to find the relation between x and γ by ray tracing.

A representative diagram of ray range as a function of horizontal wave number is shown in Figure 2. Where the slope is zero, a caustic forms: there are two in this diagram. In the top diagram, the region at some reference wave number γ_0 is approximated by a straight line with the appropriate slope, or

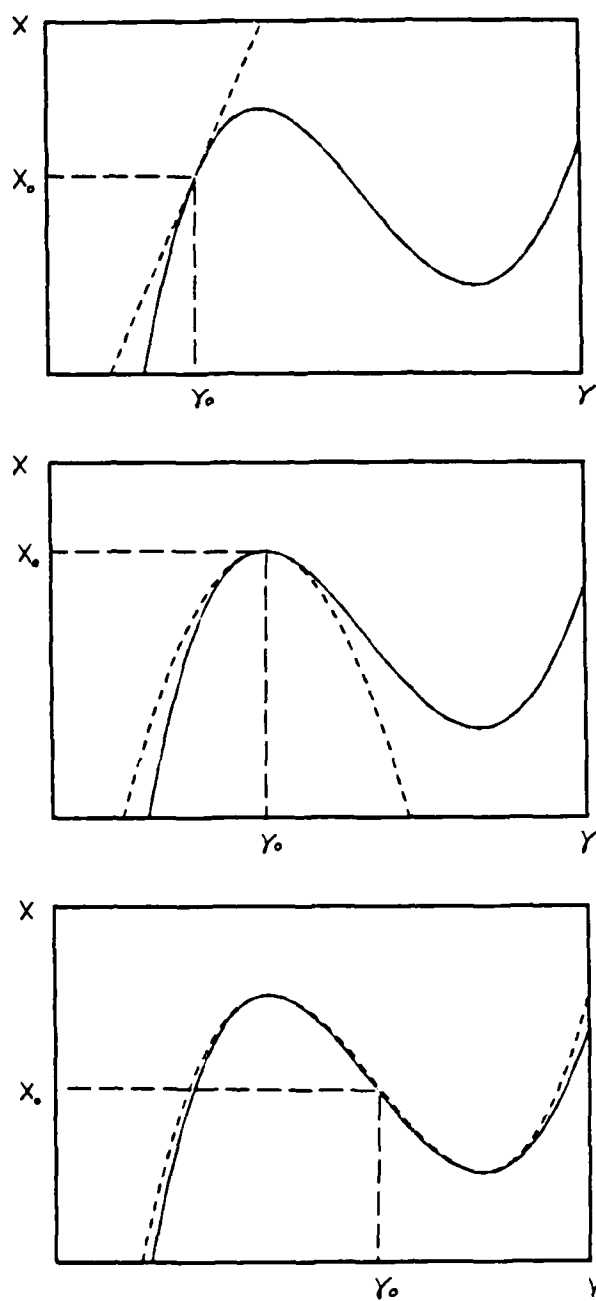


Figure 2. Typical plot of range as a function of wave number for rays near two closely-spaced caustics. Dashed lines show approximate curves for asymptotic analysis: from top to bottom they represent simple ray theory, first-order caustic correction, and second-order caustic correction.

$$x = x_0 + x'_0(\gamma - \gamma_0) \quad (2.17)$$

Here, x'_0 is the derivative of x with respect to γ at γ_0 . Inserting this equation into Equation (2.16), we can then write an approximation to the field as

$$P \simeq \exp(i\gamma_0 x_0) \bar{\Phi}(\gamma_0) \int_{-\infty}^{\infty} \exp\left[i(x-x_0)(\gamma-\gamma_0) - ix'_0(\gamma-\gamma_0)^2/2\right] d\gamma \quad (2.18)$$

If we deform the contour by rotating it by $-\pi/4$, the endpoints will coincide with the steepest descent path and the integral can be calculated

$$P \simeq (2\pi/\pm x'_0)^{1/2} \bar{\Phi}(\gamma_0) \exp\left[i(\gamma_0 x_0 \mp \pi/4 \pm Q^2/4)\right] \quad (2.19)$$

where

$$Q = (x - x_0)(2/\pm x'_0)^{1/2} \quad (2.20)$$

The sign is chosen so that the quantity under the square root is positive.

It is instructive at this point to define a ray "width" as the range difference required to produce a $\pi/2$ phase change in the field. This can be evaluated from the necessary change in Q in Equation (2.19)

$$W = \sqrt{\pi |x_o'|} \quad , \quad (2.21)$$

where W is the width parameter. Here, W gives some indication of the low-frequency spreading of rays. This definition is limited to large values of x_o' ; the derivative should really be evaluated from the change in coordinate perpendicular to the ray path rather than horizontal range.

A value for $\Phi(\gamma_o)$ can be calculated from ray theory. For x equal to x_o , the field intensity is proportional to

$$P^2 \approx (2\pi/\pm x_o') \Phi^2(\gamma_o) \quad . \quad (2.22)$$

The field can also be calculated by standard ray-tube spreading arguments

$$P^2 = c_v \left[8\pi k \gamma_o c_R \sqrt{(c_v/c_s)^2 - 1} \sqrt{(c_v/c_R)^2 - 1} |x_o'| \right]^{-1} \quad , \quad (2.23)$$

where c_s and c_R are the sound speeds at the source and receiver respectively and c_v is the vertex speed. Therefore

$$\Phi^2(\gamma_o) = c_v \left[16\pi^2 k \gamma_o c_R \sqrt{(c_v/c_s)^2 - 1} \sqrt{(c_v/c_R)^2 - 1} \right]^{-1} \quad . \quad (2.24)$$

This expression for $\bar{\phi}$ can be used in expressions that follow to relate the asymptotic expansions for the field integral to ray theory.

2.3.1 Simple caustic

At a caustic, x'_0 goes to zero and the field, according to Equation (2.22), becomes infinite. This is, of course, just a symptom of the breakdown of the approximation in Equation (2.17). In order to approximate the field near a caustic, we can fit the range curve (Figure 2, middle diagram) with a parabola at the caustic point. Then

$$x = x_0 + x''_0(\gamma - \gamma_0)^2/2 \quad . \quad (2.25)$$

Proceeding as before

$$P \simeq \exp(i\gamma_0 x_0) \bar{\phi}(\gamma_0) \int_{-\infty}^{\infty} \exp \left[i(x-x_0)(\gamma-\gamma_0) - x''_0(\gamma-\gamma_0)^3/6 \right] d\gamma \quad . \quad (2.26)$$

This can be transformed to the Airy integral and solved

$$P \simeq (2/-x''_0)^{1/3} \bar{\phi}(\gamma_0) \exp(i\gamma_0 x_0) 2\pi \text{Ai}(S) \quad , \quad (2.27)$$

where Ai is the Airy function of the first kind and

$$S = (x - x_0)(2/-x_0'')^{1/3} . \quad (2.28)$$

Here, the real root of the cube root is taken. Now, with Equations (2.27) and (2.24), we can compute the magnitude of the field near the caustic.

Let us consider how far two caustics must be separated for them to be treated as distinct. As seen in Figure 2, there are three rays at any range between the two caustics so this region is illuminated, not in shadow, and, from the shape of the parabola in the middle diagram, x_0'' is negative for this caustic. The zone in between the two caustics covers ranges less than x_0 , therefore, from Equation (2.28), S is negative there. (S is also negative for the intervening region when calculated for the other caustic.) For negative arguments, A_i is oscillatory and the first half-cycle of these oscillations is complete for S equals $-\pi$. If we take this, somewhat arbitrarily, to be the range interval C_0 needed for the caustic to be distinct, we find from Equation (2.28) that

$$C_0 = \left| x_0''/2 \right|^{1/3} \pi . \quad (2.29)$$

2.3.2 Multiple caustic

If there are two caustics closer than C_D , then a further modification to this asymptotic theory is required. Instead of fitting one caustic with a parabola, we can fit the pair with a cubic. This is illustrated in the bottom diagram of Figure 2. The range equation is

$$x = x_0 + x_0'(\gamma - \gamma_0) + x_0'''(\gamma - \gamma_0)^3/6, \quad (2.30)$$

and the field integral can be approximated as

$$P \approx (24/x_0''')^{1/4} \phi(\gamma_0) \exp(i\gamma_0 x_0) \int_{-\infty}^{\infty} \exp[i(Yt - Xt^2 - t^4)] dt, \quad (2.31)$$

where

$$t = (x_0'''/24)^{1/4} (\gamma - \gamma_0), \quad (2.32)$$

and the parameters X and Y are given by

$$X = x_0' (6/x_0''')^{1/2}, \quad (2.33)$$

$$Y = (x - x_0)(24/x_0''')^{1/4}.$$

The integral in Equation (2.31) can be integrated numerically if the contour is first rotated by $-\pi/8$. The convergence is then quite rapid.

A similar integral is used by Pearcey (1946) to evaluate the field near a cusp which is just a limiting case of two caustics. Pearcey fits the cubic by point, slope, and first and second derivative at the cusp while, in the above analysis, the cubic is fit by point and slope at each caustic. In this way, the caustic locations are preserved; however, they are forced to be equal in strength.

Incidentally, a plot of the magnitude of the integral in Equation (2.31) is given by Brekhovskikh (1980). The integral there is slightly different (all of the signs in the exponent are positive), but the result is exactly equal to the complex conjugate of that obtained here.

These asymptotic approximations will be compared to a normal-mode solution in Chapter VI where we will see that the multiple caustic approximation does generally predict the correct structure. On the other hand, the first-order asymptotic correction results are consistently poor.

The techniques developed in this chapter will be applied in Chapter VI to the investigation of the field near a complex focus. In that chapter, both mode theory and asymptotic ray theory will be used to analyze the structure of the unperturbed field. The next chapter (Chapter III) will summarize the tools that are used for the analysis of perturbations.

Chapter III

METHODS FOR RANGE-DEPENDENT PERTURBATIONS

3.1 Field Solutions

Once spatial perturbations are introduced into the sound-speed profile, the problem becomes range-dependent and, in the problem considered in Chapter V, strongly so. To correctly analyze acoustic propagation, the solution must account for rather large variations in sound speed over one wavelength. We will first consider single-frequency methods and then those techniques that yield a direct solution in the time domain.

3.1.1 Single-frequency (CW) techniques

Ray tracing programs have been developed for media with range as well as depth dependence (Andersen and Kak, 1982); however, they do not fully account for diffraction even with wave corrections for simple caustics. Adiabatic-mode formulations (Pierce, 1965) and parabolic-equation solutions (Tappert, 1977) can cope with slow variations of parameters in range but they are single-frequency models; broadband representation is difficult and expensive (see Chapter IV). In addition, phase errors (for example, Brekhovskikh and Lysanov, 1982) in the parabolic method could alter the physical phase fluctuations near the focusing regions. A coupled-mode approach (Milder, 1969) may handle the variations in range encountered but only at an even greater cost. Note that range-de-

pendent normal-mode theory will, however, be used to estimate fluctuations.

3.1.2 Time-dependent solutions

The time-dependent wave equation is a hyperbolic partial differential equation and, therefore, can be reduced by the method of characteristics to a simpler problem of signal progression along certain surfaces (von Mises, 1958). In one space dimension, this approach works very well even for nonlinear partial differential equations.

As an example, consider a plane wave incident on a region in a fluid in which the sound speed changes linearly over some finite distance (see Figure 3). There is no impedance discontinuity to produce a reflection but there is weak diffractive backscatter from the sound-speed gradient. As shown in the figure, the method of characteristics (dashed line) produces an accurate calculation of the pressure impulse response of such a layer as compared to a much more expensive superposition of single-frequency plane wave reflection responses (solid line). Also notice that the superposition solution suffers from oscillatory "ringing" at the edges of sharp level changes (Gibbs' phenomenon).

For more than one spatial dimension, Butler (1960) has shown that the method of characteristics can still be used but the resulting algorithm introduces a great deal of dissipation (false absorption) and dispersion (phase speed errors). Furthermore, the code is complicated and boundary conditions are difficult to implement.

Moretti (1979) has developed a much simpler finite-difference scheme that is weighted so that signals are propagated in the proper character-

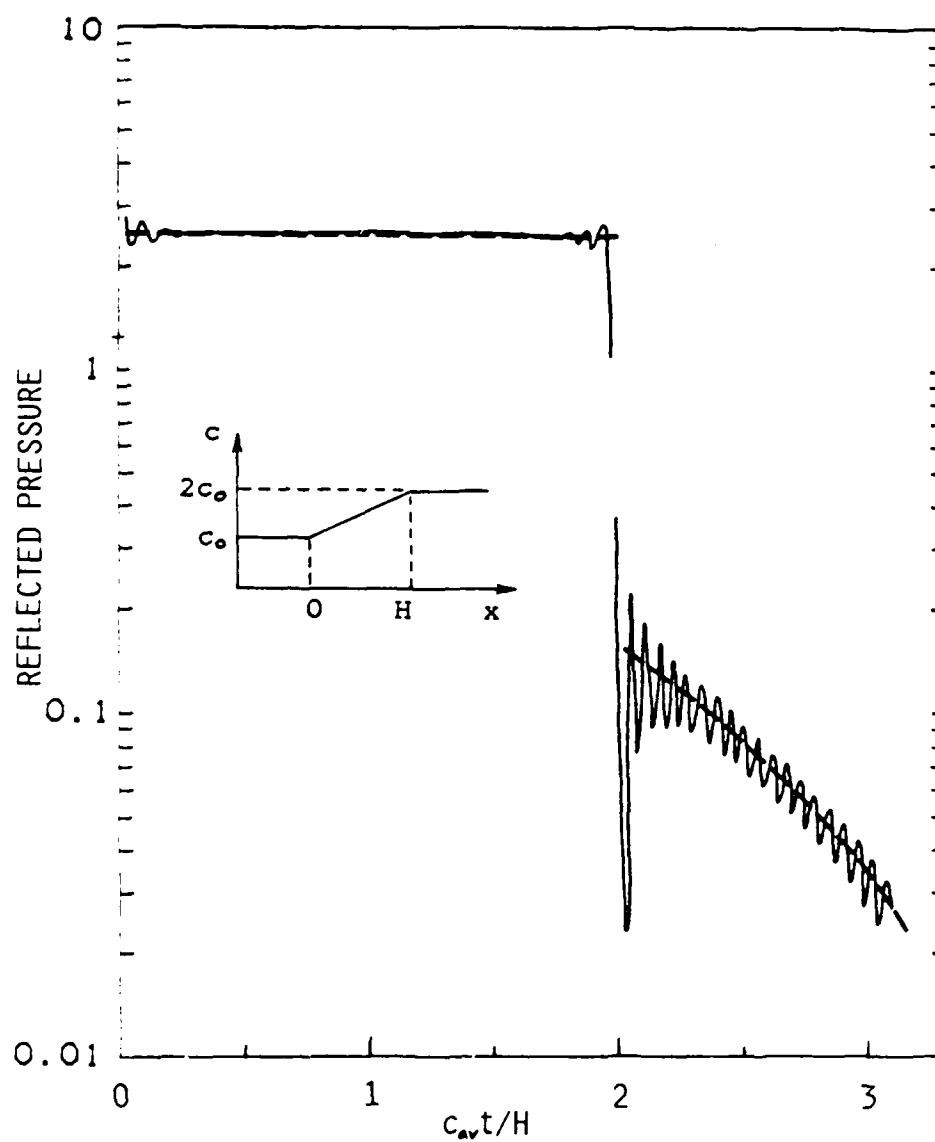


Figure 3. Prediction of reflected pressure waveform from impulse incident to a one-dimensional gradient layer. Solid line shows Fourier analysis results and dashed line gives results of the method of characteristics. The average sound speed in the gradient layer is c_{av} .

istic directions; the method has proven quite successful for time-dependent fluid flow problems. For acoustics, however, dissipation in the numerical code rapidly distorts the waveshape. This will be illustrated below.

One important advantage of the method of characteristics is that the physics of signal propagation is respected; the numerical grid advances in the direction of local signal flow rather than in an arbitrary direction. Many codes advance the signal using data from field points that could not physically affect the signal (e.g., using points that the signal could not have reached yet). This turns out not to be too critical for linear acoustics but if there are finite amplitude signals, these will be seriously distorted. With a small enough grid to combat the dissipation, Moretti's technique may be useful for problems in nonlinear acoustics.

Hyperbolic partial differential equations lend themselves to analysis based on signal dissipation and dispersion. Numerical solutions can be tested by introducing the Fourier components of a pulse and examining the level change and phase shift as the solution proceeds in time (von Neumann and Richtmyer, 1950). Using this procedure, a number of finite-difference solutions to either the wave Equation (2.6) or the coupled governing Equations (2.4) and (2.5) were evaluated. Among them were Euler and MacCormack predictor-corrector schemes (MacCormack, 1970), first- and second-order Moretti algorithms and a direct finite-difference solution of the wave equation. This Fourier analysis is outlined in the next section along with the development of the direct solution method.

3.1.3 Direct finite-difference solutions

The selection of a direct finite-difference approximation to the wave equation was motivated by the ability of this approach to model short duration impulse-like signals (very large bandwidth) in a range-dependent environment with no numerically induced dissipation and only a small, predictable amount of dispersion. In addition, for low frequencies, the method has about the same computational expense as a normal-mode solution in a range-independent duct. This latter point was only evident after the algorithm was fully verified; however, the dissipation/dispersion characteristics can be determined from the basic approximation. Hence, we will consider these characteristics along with the development of the finite-difference approximation.

Some special notation is convenient for describing finite-difference equations: let the pressure be given at discrete points (in space and time) by the symbol

$$p_{lm}^n = p(l\Delta x, m\Delta y, n\Delta t) \quad . \quad (3.1)$$

To further reduce the complexity, denote the local reference point as $p_{00}^0 = p_{lm}^n$ and, for example, $p_{0-1}^1 = p_{l,m-1}^{n+1}$.

The wave equation in two dimensions is

$$p_{xx} + p_{yy} = p_{tt}/c^2 \quad . \quad (3.2)$$

By replacing the partial derivatives with their first-order finite-difference approximations and solving for the pressure at the (n+1) time increment, we can write

$$p'_{oo} = 2(1 - 2q^2)p_{oo}^o - p_{oo}^{-1} + q^2(p_{io}^o + p_{o,i}^o + p_{io}^o + p_{o,-i}^o) , \quad (3.3)$$

where $q = cat/\Delta x$ and Δx and Δy are equal for a square grid. This is the fundamental equation for computing the field points at advancing time but there are several ways to select the grid points. Figure 4 shows a field point and its nearest eight neighbors. If the x axis is horizontal, the open circles are used as grid points in Equation (3.3) with $\Delta x = h$. If, on the other hand, the coordinate system is rotated 45 degrees, the dark circles are used with $\Delta x = \sqrt{2} h$. Normally dissipation/dispersion characteristics are functions of the angle of propagation with respect to the grid; however, Vichnevetsky and Bowles (1982) have suggested a weighted average of difference equations for the two grids discussed above. The resulting equation for p at the (n+1) step in time is

$$p'_{oo} = 2p_{oo}^o - p_{oo}^{-1} + q^2 \left[\beta G_{45}/2 + (1 - \beta) G_o \right]$$

$$G_o = p_{oi}^o + p_{io}^o + p_{io}^o + p_{o,-i}^o - 4p_{oo}^o$$

$$G_{45} = p_{ii}^o + p_{i,-i}^o + p_{-ii}^o + p_{-i,-i}^o - 4p_{oo}^o , \quad (3.4)$$

where β is a weighting factor that ranges from 0 to 1.

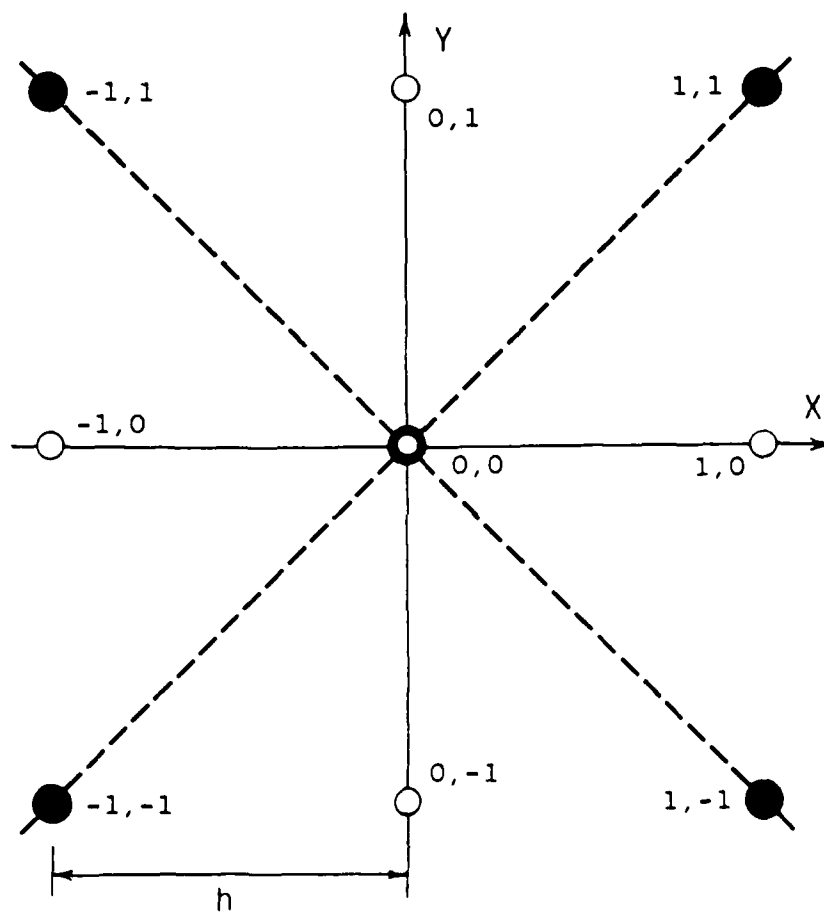


Figure 4. Interior grid point and nearest neighbors for finite-difference calculation. Dark circles and dashed axes show rotated secondary grid.

Consider the effects of this differential equation on a plane wave propagating through the grid. Let

$$p_{oo}^o = \exp[(\alpha - ikc^*)n\Delta t] \exp[i(k_x l + k_y m)h] , \quad (3.5)$$

where \vec{k} is the wave number vector with components k_x and k_y , α is the apparent absorption, c^* is the apparent phase speed and h is the grid spacing. If this form for p is substituted into Equation (3.4) and solved for the pressure ratio per time step, the wave shape change is given by

$$p'_{oo}/p_{oo}^o = \exp(\alpha\Delta t) \exp(-ikc^*\Delta t) . \quad (3.6)$$

By defining an amplification factor

$$A = \left| p'_{oo}/p_{oo}^o \right| , \quad (3.7)$$

and an apparent phase speed

$$c^* = \arg(p'_{oo}/p_{oo}^o)/k\Delta t , \quad (3.8)$$

the dissipation and dispersion effects can be separated. Ideally, the amplification factor A should be unity and c^* should be equal to the true local sound speed c .

For Equation (3.4)

$$A = \left| D + i\sqrt{1 - D^2} \right|, \quad (3.9)$$

and

$$D = 1 - q^2 \left[2 - \beta(1 + \cos \theta_x \cos \theta_y) - (1 - \beta)(\cos \theta_x + \cos \theta_y) \right], \quad (3.10)$$

where $\theta_x = kh \cos \phi$, $\theta_y = kh \sin \phi$ and ϕ is the angle of the wave number vector with respect to the x axis. Here, A is identically unity as long as the magnitude of D is less than one. As described below, the parameter β is selected to keep the dispersion errors independent of the direction of propagation. Also, the high-frequency limit of the source spectrum sets an upper limit on kh for a particular grid spacing. Consequently, the solution's stability is controlled by q .

For a hyperbolic differential equation, the Courant-Friedrichs-Lewy (Courant, et al., 1956) condition (CFL condition) sets an upper limit of one on q . (This is a necessary but not sufficient condition for stabil-

ity.) Physically, the CFL condition insures that the numerical solution keeps up with the signal propagation. The parameter q is the ratio of the distance the actual signal travels in one time step ($c\Delta t$) to the spatial advance of the grid (h). If the grid doesn't advance in space faster than the signal, the signal will eventually pass completely out of the solution region.

In practice, q must be somewhat less than one in order to insure that the magnitude of D in Equation (3.10) remains less than one. A practical limit for this particular finite-difference scheme is 0.8.

The apparent phase speed ratio is given by

$$c^*/c = \tan^{-1}(\sqrt{1 - D^2}/D)/khq \quad (3.11)$$

where q has been used to replace the Δt from Equation (3.8) with h . This ratio (which should be unity) is plotted in Figure 5 as a function of the wavevector angle for several values of β . For β of roughly 0.4, the dispersion curve is very nearly isotropic. In Figure 6, the value $\beta = 0.4$ is taken and the apparent phase speed ratio is shown as a function of the normalized grid size kh/π for various values of q .

This direct finite-difference algorithm introduces no artificial absorption and is stable as long as the time step is chosen to restrict the magnitude of q . There is some dispersion but it can be limited by proper choice of the spatial grid size h and its effects are virtually independent of the direction of propagation.

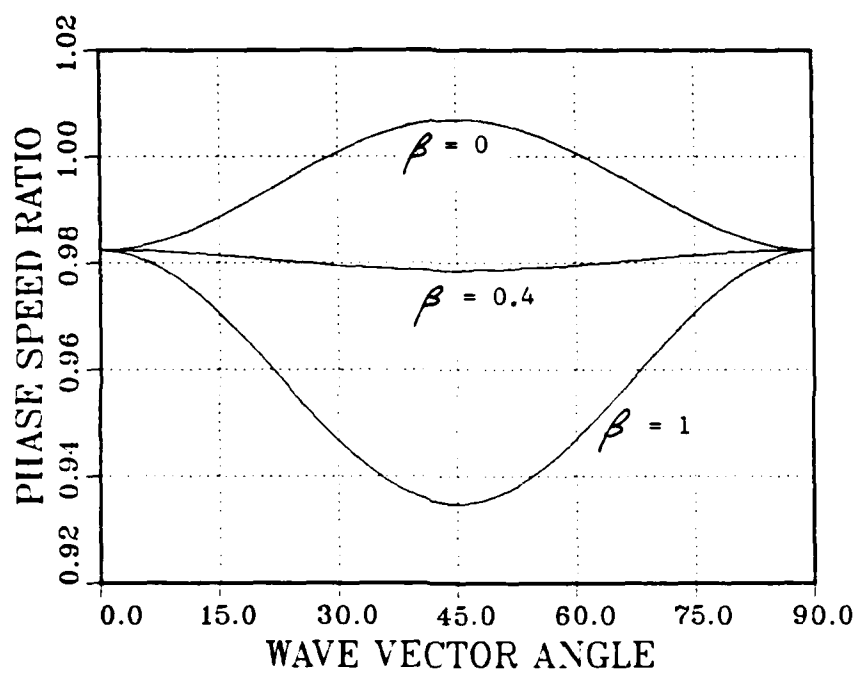


Figure 5. Apparent phase speed ratio c^*/c as a function of the angle of the wavefront normal with respect to horizontal. Each curve corresponds to a different weight β and $kh = \pi/3$.

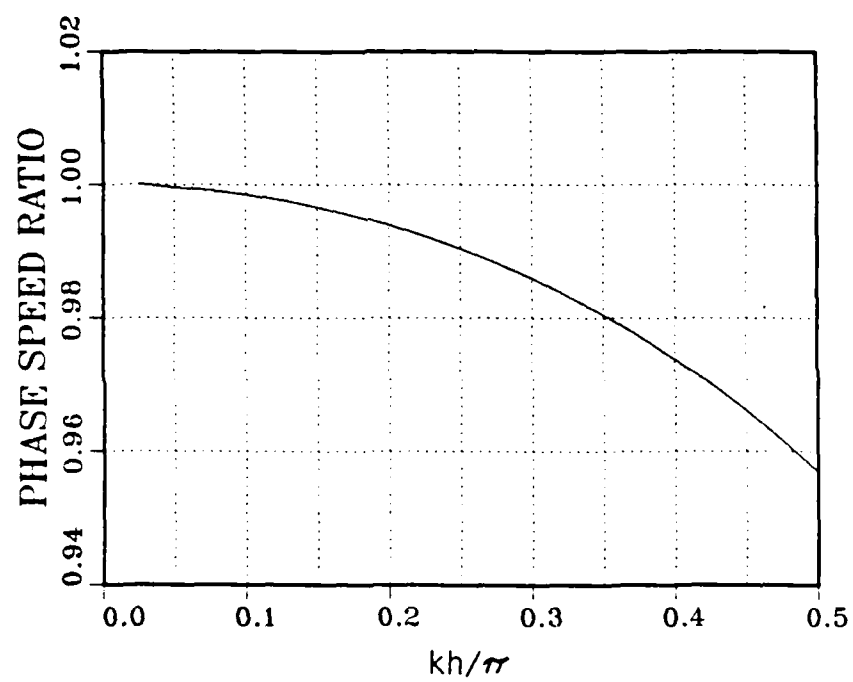


Figure 6. Phase speed ratio c^*/c as a function of normalized grid spacing for $\beta = 0.4$.

By way of comparison, two other plots are shown in Figure 7 of the dissipation and dispersion characteristics of several other solution techniques. A simple weighted-characteristics code is shown along with a simple predictor-corrector scheme and, for reference, the curves for the direct finite-difference method. Notice that, even though the predictor-corrector scheme is a second-order method (halving the step size theoretically cuts the error by a factor of four), its dissipation renders it less accurate than the direct method which is only first-order.

3.2 Special Methods for Fluctuations

Since perturbations of an acoustic medium such as the atmosphere or the ocean are extremely difficult to model in detail, a suitable analytical method for determining the statistics of signal fluctuations based on some parameter or parameters of the perturbations would be most useful. Much of the work that has been done in this area has been based on models of homogeneous and isotropic scatterers (and often of single scatterers) in an isotropic medium. The next section summarizes some of the more important work in this regard but, because physical perturbations are often far from homogeneous and isotropic, none of these results are directly useful here. Section 3.2.2 summarizes Flatte's (1979) method for calculating expected fluctuation statistics for an inhomogeneous medium and this method will be extended to regions near caustics. Finally, a somewhat more promising approach based on range-dependent normal-mode theory is developed.

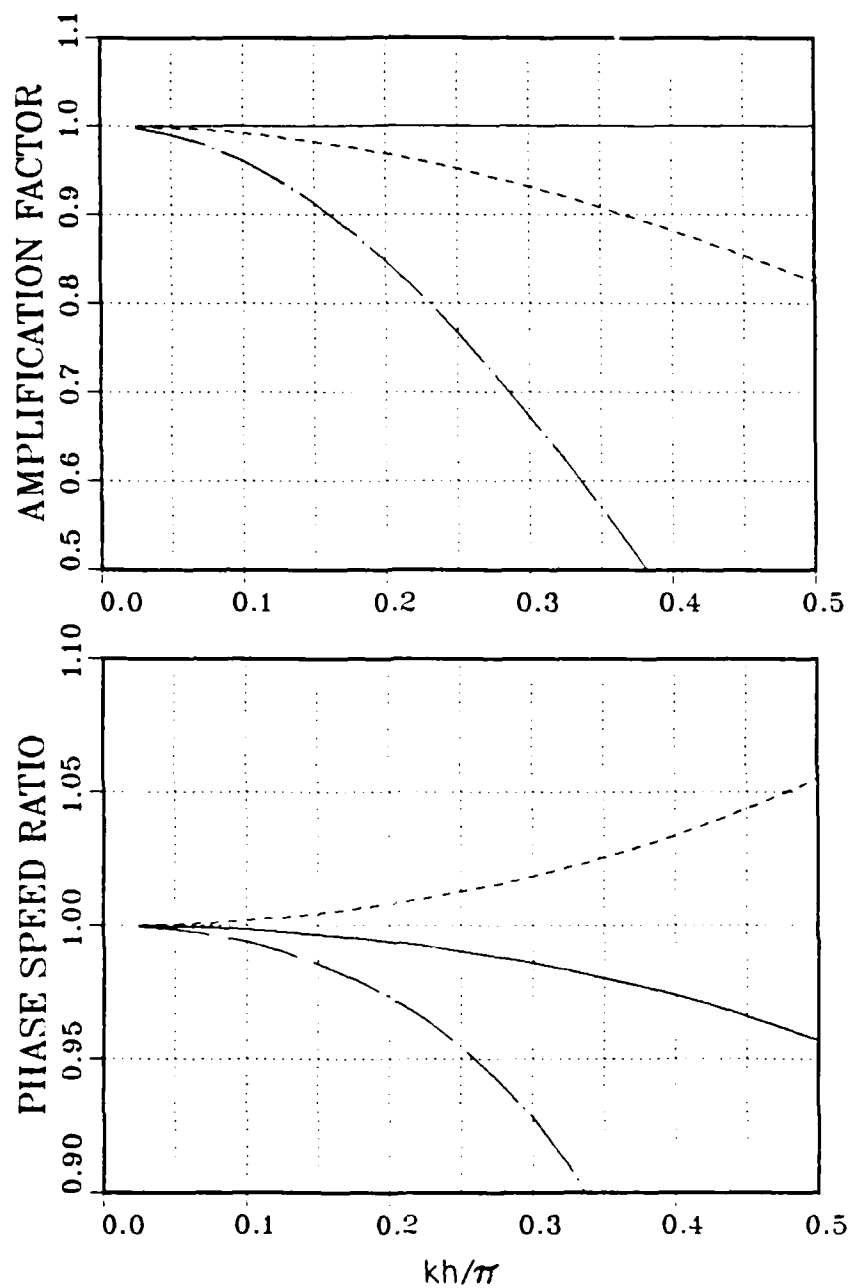


Figure 7. Comparison of the dissipation and dispersion characteristics of the finite-difference method (—), the weighted-characteristics method (---), and a predictor-corrector method (— · —).

3.2.1 Homogeneous isotropic turbulence models

Chernov (1960) and Tatarskii (1967) formulated the fluctuation theory for single spherical scatterers in an otherwise homogeneous and unbounded medium. The principal result was the identification of two different dependencies of fluctuation magnitude on range. The normalized fluctuation magnitude V , given by

$$V = \sqrt{(P - \bar{P})^2} / \bar{P} , \quad (3.12)$$

varies either as $r^{3/2}$ for $r \ll r_0$ or as $r^{1/2}$ for $r \gg r_0$ where P is the pressure amplitude of a particular single-frequency component

$$r_0 = ka^2/4 , \quad (3.13)$$

and a is the length scale of an individual scatterer.

By analogy to Flatte's (1979) analysis of ocean perturbations, we can identify five points at which real media depart substantially from the homogeneous single-scattering model:

1. multiple scattering may predominate in real turbulence;
2. the medium itself introduces refraction thus causing deterministic multipath;
3. the strength of perturbations varies vertically;
4. because of turbulence cascading, the dynamical range of perturbations is large;

5. the boundaries introduce multipath by reflection.

Clearly, the single-scattering model cannot predict the saturation that is observed at long ranges: V approaches a limiting value of 0.52 (Skudrzyk, 1957).

Minor improvements have been made to this theory: for example, work on absorption by scattering by Brown and Clifford (1976) and the work on the effects of turbulence on multipath interference by Ingard and Maling (1963). However, these models correct isolated deficiencies without treating the overall complexity of wave scattering by turbulence in a refracting medium. Roth (1983) demonstrates the inadequacy of these and other simple models when applied to acoustic fluctuations in an atmospheric boundary layer with convective instability.

3.2.2 Strength and diffraction parameters for fluctuations

One method for analyzing the ability of a realistic medium to produce signal fluctuations has been developed by Flatte (1979). He accounts for sound-speed perturbations through two parameters: a fluctuation strength parameter \mathcal{F} and a fluctuation diffraction parameter \mathcal{A} .

The strength parameter is the rms phase fluctuation produced by perturbations along the unperturbed ray path. The diffraction parameter, a modification of Tatarskii's (1971) wave parameter, describes how much the ray path must be changed in order to produce phase interference at the receiver point. Another point of view is that \mathcal{F} contains information on the magnitude of the perturbations in sound speed while \mathcal{A} indicates the significance of multipath: i.e., whether distinct paths can form or the single path is diffractively "blurred".

This formulation accounts for the inhomogeneity of the medium itself, for the distribution of perturbations, for multiple scattering, and for multiple paths. Its fundamental defect is that it is based on ray theory and cannot easily be extended into classical shadow zones or to low frequencies. As it was originally developed, it cannot be used near or on caustics, but this deficiency will be corrected below.

In order to define the strength parameter $\bar{\phi}$, we can write a phase integral over the ray path from source to receiver including only the phase contributions from the perturbation component of the sound speed. The mean square of this integral averaged over time is the fluctuation strength

$$\bar{\phi}^2 = \left\langle \left(k_0 \int^{\text{ray}} \mu dx \right)^2 \right\rangle, \quad (3.14)$$

where μ is the normalized perturbation term

$$\mu(x, z, t) = \left[c(x, z, t) - c_u(z) \right] / c_0, \quad (3.15)$$

and c_u is the unperturbed profile.

The diffraction parameter \mathcal{A} is considerably more difficult to compute in a refracting medium. The basic definition is

$$\mathcal{A} = (R/L)^2 / 2\pi, \quad (3.16)$$

where L is the vertical correlation distance of the perturbation patches. The quantity R is the vertical distance through which an intermediate point along the unperturbed ray path must be displaced vertically in order to produce a π phase difference at the receiver. In moving this intermediate point, the source angle must be adjusted so that the new ray hits the displaced point and then the angle must be changed at that point so that the ray continues on to the receiver. Notice that the strength of the perturbations does not affect the magnitude of R ; it is purely a measure of diffraction. The local Δ value is, however, weighted by the normalized local ϕ and integrated along the entire path to get the composite Δ . This prevents a very large Δ at a point at which there are very weak perturbations from biasing the overall Δ .

In practice, the path deviation required to produce a full π phase change is not calculated but, instead, the intermediate point is displaced a small amount and R is computed based on the rate of phase change with vertical displacement. The total travel time along a ray can be expanded as a series for small intermediate displacement ξ as follows,

$$T(\xi) \approx T(0) + \xi T' + \xi^2 T''/2 + \xi^3 T'''/6 \quad . \quad (3.17)$$

The eigenray is the minimum travel time ray so the second term on the right side is zero and the phase difference can be written as

$$\omega [T(\xi) - T(0)] \approx \omega \xi^2 (T'' + \xi T'''/3)/2 . \quad (3.18)$$

Normally T'' is much larger than T''' for small ξ but T'' vanishes at caustics, hence the third-order term will be retained. When the phase difference is π then ξ is equal to R ; therefore

$$fR^2(T'' + RT'''/3) = 1 , \quad (3.19)$$

gives the condition for R . If we neglect T''' , the expression reduces to Flatte's expression as long as the unperturbed sound speed is constant everywhere. (Flatte derives R in terms of path length and that quantity is only stationary on the eigenray if the eigenray is a straight line.)

At this point, the quantities T'' and T''' must be related to the quantities normally obtained by ray tracing. Since the ray vertex speed c_v is a more convenient independent variable than vertical displacement, we will use it initially. The derivative of travel time T with respect to c_v holding x constant is equal to the derivative of T holding z constant (the usual ray derivative) minus the travel time increment along the extra path segment of the latter ray

$$(\partial T / \partial c_v)_x = (\partial T / \partial c_v)_z - (dl/dx)(\partial x / \partial c_v)/c_p , \quad (3.20)$$

where c_p is the sound speed at the point of displacement. By Snell's law

$$c_p/c_v = dx/dl, \quad (3.21)$$

$$dz/dx = \sqrt{(c_v/c_p)^2 - 1},$$

so that

$$T' \approx \left[(\partial T / \partial c_v)_z / (\partial x / \partial c_v) - c_v/c_p^2 \right] / \sqrt{(c_v/c_p)^2 - 1}. \quad (3.22)$$

Now T is identically zero on the proper ray between the source and the receiver so a new pair of rays must be constructed one of which connects the source to a point offset slightly above the original ray and another that connects that offset point to the receiver. This is repeated until there are five rays: the original ray and four other rays that have vertical midpoint displacements of ξ , 2ξ , $-\xi$, and -2ξ . From these rays, the derivatives T'' and T''' are computed numerically. Finally, using Equations (3.19) and (3.16), R and A are calculated.

3.2.3 Range-dependent Normal-mode Theory

While the A - \mathcal{E} characterization does attempt to account for real distributions of sound-speed perturbations, it is based on ray theory and, as such, it cannot be expected to produce reliable results in a highly diffractive field. An approximate approach can, however, be developed from a wave point of view using range-dependent normal-mode theory.

By taking the Fourier transform in time of the wave Equation (2.7), the Helmholtz equation for a medium with range-dependent perturbations can be written

$$\partial^2 p / \partial x^2 + \partial^2 p / \partial z^2 + k_p^2 p = \delta(z-z_0) \delta(x) \quad (3.23)$$

Let

$$p(x, z) = \sum_m \varphi_m(x) u_m(z) \quad , \quad (3.24)$$

where u_m are the unperturbed (i.e., range-independent) eigenfunctions given by Equation (2.9). By assuming this form for the pressure, mode coupling is neglected. Substitute Equation (3.24) into Equation (3.23), multiply by u_n and integrate over z to yield

$$d^2 \varphi_n / dx^2 + (\bar{\gamma}_n^2 + D^2) \varphi_n = u_n(z_0) \delta(x) / \int u_n^2 dz \quad , \quad (3.25)$$

where

$$D^2 = \int (k_p^2 - k^2) u_n^2 dz / \int u_n^2 dz , \quad (3.26)$$

and $\bar{\gamma}_n$ is the range-averaged eigenvalue used to compute u_n . At this point, neglect the backscattered field by writing ϕ_n as

$$\phi_n(x) = a_n(x) \exp(i\bar{\gamma}_n x) . \quad (3.27)$$

If the problem were truly range-independent, the a_n would be constants. Substitute this form for ϕ_n into Equation (3.25) so that, after neglecting the second derivative of a_n , the a_n functions can be found and

$$\phi_n(x) = u_n(z_0) \exp \left[i(\bar{\gamma}_n + D^2/2\bar{\gamma}_n)x \right] / 2i\bar{\gamma}_n \int u_n^2 dz , \quad (3.28)$$

Thus, the principal effect of the perturbations is to produce a shift in the eigenvalue given by

$$\gamma_{np} - \bar{\gamma}_n = \int (k_p^2 - k^2) u_n^2 dz / 2\bar{\gamma}_n \int u_n^2 dz . \quad (3.29)$$

This provides at least an approximate method of computing signal fluctuations based on wave theory. Both the eigenvalue shift technique and

the extended \mathcal{A} method will be applied in Chapter VII to a specific focusing problem.

The integrals in Equation (3.29) can, of course, be performed numerically but the choice of Airy functions for the vertical field variations allows these integrals to be evaluated in closed form for either constant or linear variation in $k^z - k_p^z$. Bucker (1970) gives an exact differential for the integrand if $k^z - k_p^z$ is constant

$$u^2 dz = - d \left[(du/dZ)^2 - Zu^2 \right] / \eta . \quad (3.30)$$

If we use this expression and Stoke's equation for the Airy functions

$$d^2 u / dZ^2 - Zu = 0 , \quad (3.31)$$

where u is any linear combination of Ai and Bi , we can write an exact differential for

$$3Zu^2 dZ = d \left\{ u(du/dZ) - Z \left[(du/dZ)^2 - Zu^2 \right] \right\} . \quad (3.32)$$

This can then be transformed into the desired form

$$\eta^2 z u^2 dz = d \left\{ \left[u(du/dZ) - Z(du/dZ)^2 + Z^2 u^2 \right] / 3 - \left[(\omega^2/c_o^2 - \gamma^2)/\eta^2 + \eta z_o \right] \left[(du/dZ)^2 - Z u^2 \right] \right\} . \quad (3.33)$$

Using Equations (3.30) and (3.32), the eigenvalue shift can be computed from Equation (3.29) as long as the perturbations can be approximated by segments of constant and linear $k^2 - k_p^2$. For small perturbations, the relationship

$$k^2 - k_p^2 \simeq 2\omega^2 \delta c / c^3 , \quad (3.34)$$

holds.

In the next chapter, extensive tests of the finite-difference method will be outlined in order to establish the technique's validity. The techniques described above (the normal-mode and the finite-difference techniques, in particular) will be applied in Chapter VII to the study of fluctuations induced by turbulence in a region of strong focusing.

Chapter IV

VALIDATION OF FINITE-DIFFERENCE SOLUTION

Since direct finite-difference methods have not generally been applied to time-dependent acoustic fields, the technique should be tested for its accuracy in relation to other known solutions. While the dispersion/dissipation analysis of the previous chapter sets some specific limits on the distortion introduced by the finite-difference approximation, comparisons against known solutions are necessary to insure that diffraction, refraction, boundary effects, and the source term are properly represented.

4.1 Boundary Conditions and Source Diffusion

Transparent-boundary conditions (Appendix A) are used in the finite-difference model to avoid contamination of the focused field by simply reflected arrivals. Consequently, a very simple test can be performed by keeping the sound speed constant and by applying transparent-boundary conditions at the horizontal boundaries indicated in Figure 1. The finite-difference solution can then be compared to two-dimensional free-field spreading. This will test the model's representation of the transparent-boundary conditions and of the diffusive "tails" associated with two-dimensional geometries.

The governing equation throughout this study is the forced wave Equation (2.7). In this first test, the sound speed is constant everywhere

and there are no boundaries so by converting the equation to cylindrical coordinates with the source at the origin and taking the Fourier transform in time and the Hankel transform in space, we can write

$$P(\omega) = iF(\omega) H_0^{(1)}(kx) / 4, \quad (4.1)$$

where P is the Fourier transform of pressure and F is the Fourier transform of the source waveform

$$f(t) = A \exp(-b^2 t^2 / 4), \quad (4.2)$$

or

$$F(\omega) = 2A\sqrt{\pi} \exp(-\omega/b)^2 / b. \quad (4.3)$$

The factors A and b scale the amplitude and the extent of the spectrum respectively.

The relative gain (or loss) of the finite-difference model with respect to the free-field spreading Equation (4.1) is shown in Figure 8 for several observation points roughly midway between the two boundaries and at ranges of 2.5 to 3.5 times the boundary separation. The independent variable here is the normalized grid spacing kh . The steep departure below kh equal to 0.075 is caused by the breakdown of the transpar-

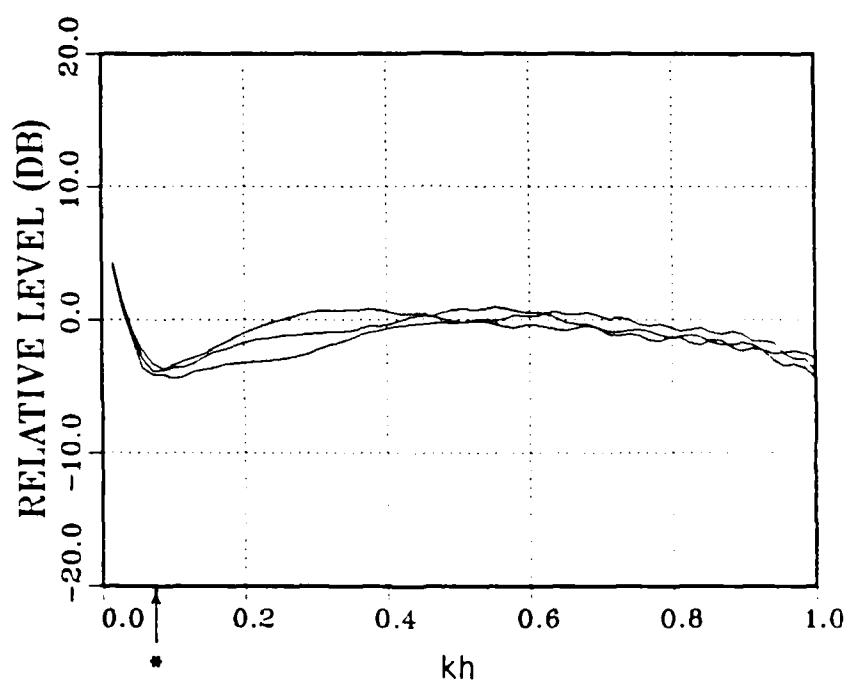


Figure 8. Level predicted by finite-difference calculation relative to free-field spreading for a constant sound-speed channel with transparent boundaries. The * marks the point at which the channel width is half the wavelength.

ent-boundary condition: below this point the boundaries are less than a half-wavelength apart and errors in the boundary conditions become large enough to affect the solution significantly. Between 0.075 and 0.95 there is a small departure from the desired response. These changes, as long as they are smooth, are of no concern for this study since enhancement near the caustic and loss in the shadow will cause far greater swings in magnitude than these errors.

4.2 Corner Diffraction

Although the physical model discussed in Chapter V does not have any wedge-shaped boundaries, the ability of the technique to predict the field in the shadow behind a wedge is an important indication of its overall representation of diffraction. This is, in fact, a good way of separating diffraction and refraction since this shadowing occurs even for constant sound speed.

4.2.1 Integral solution for diffraction by a wedge

An analytical solution for time-dependent two-dimensional wedge diffraction can be constructed by the method of normal coordinates (Biot and Tolstoy, 1957). For the polar coordinate system shown in Figure 9 with the origin at the apex of a pressure-release wedge, the solution to the forced wave equation is

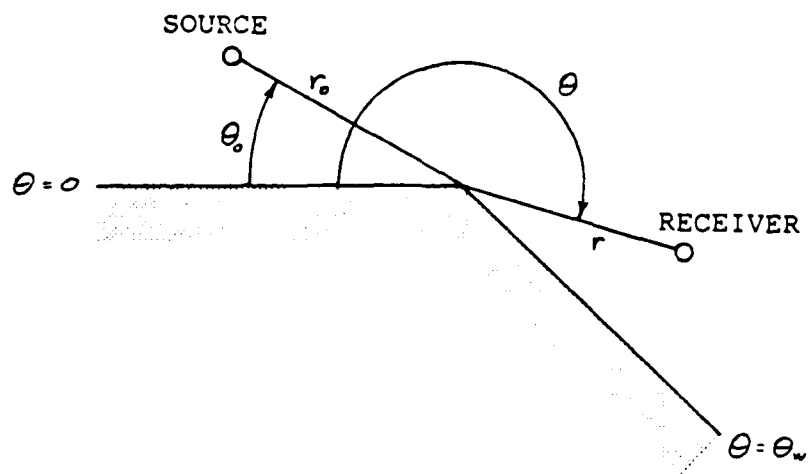


Figure 9. Geometry for the two-dimensional wedge problem.

$$p(r, \theta, t) = c/\theta_w \sqrt{rr_0} \cdot \sum_{n=1}^{\infty} P_{\nu_n - \frac{1}{2}}(A) \sin \nu_n \theta_0 \sin \nu_n \theta, \quad (4.4)$$

for ct greater than $(r - r_0)$ and less than $(r + r_0)$ and

$$p(r, \theta, t) = -2c/\pi\theta_w \sqrt{rr_0} \cdot \sum_{n=1}^{\infty} Q_{\nu_n - \frac{1}{2}}(-A) \cos \nu_n \pi \sin \nu_n \theta_0 \sin \nu_n \theta, \quad (4.5)$$

for ct greater than $(r + r_0)$ where a unit impulse driver has been used (i.e., $F = 1$). The pressure is zero before the range of Equation (4.4). Also

$$A = (r^2 + r_0^2 - c^2 t^2)/2rr_0, \quad (4.6)$$

and

$$\nu_n = n\pi/\theta_w. \quad (4.7)$$

This is the exact solution for a pressure-release wedge. However, computations of p are not practical because of the very poor convergence of the series coupled with the difficulty of computing the Legendre functions for non-integer degree.

This problem can be circumvented by transforming the expression as follows. First, the Legendre functions are replaced by contour integrals of simpler functions and then the summation and the integration are interchanged. This allows closed form evaluation of the sum. A simple integral results that is easily evaluated numerically.

Consider Equation (4.4): Gradshteyn and Ryzhik (1965) give an integral form for the Legendre function of the first kind

$$P_{n-\frac{1}{2}}(A) = \pi^{-1} \int_0^{\pi} (A + \sqrt{A^2 - 1} \cos \xi)^{n-\frac{1}{2}} d\xi, \quad (4.8)$$

which is valid for $\text{Re}(A)$ greater than zero. The limit on n in Equation (4.4) corresponds to A between 1 and -1 so Equation (4.8) is not completely suitable.

Equation (4.8) is limited because, for $\text{Re}(A)$ less than zero, the branch cut associated with the branch given by

$$A + \sqrt{A^2 - 1} \cos \xi = 0, \quad (4.9)$$

intersects the original integration path. By defining a new integration contour C_p that goes from 0 to $\pi/2$, then from $\pi/2$ to $\pi/2 + i\xi_c$ along one

side of the branch, around the branch point (a zero not a pole), down the other side, and finally along the real axis to π , we can write

$$P_{\nu_n - \frac{1}{2}}(A) = \pi^{-1} \int_{C_p} (A + \sqrt{A^2 - 1} \cos \xi)^{\nu_n - \frac{1}{2}} d\xi, \quad (4.10)$$

for the entire range required by Equation (4.4). The imaginary part of ξ at the branch point is given by

$$A + \sqrt{1 - A^2} \sinh \xi_i = 0. \quad (4.11)$$

For $\text{Re}(A)$ greater than zero, this diversion is, of course, unnecessary.

Next, substitute this integral form for the Legendre function into Equation (4.4) and interchange the integration and summation to write

$$p = c \int_{C_p} V^{-\frac{\theta_w}{2\pi}} \left[\sum_{n=1}^{\infty} V^n \sin \nu_n \theta_0 \sin \nu_n \theta \right] d\xi / \pi \theta_w \sqrt{r r_0}, \quad (4.12)$$

where

$$V = (A + i \sqrt{1 - A^2} \cos \xi)^{\pi/\theta_w}. \quad (4.13)$$

If we expand the sine functions as exponentials and replace V^n by $\exp(n \ln V)$, then the entire quantity within the summation can be written

as terms of the form $\exp(n\pi i)$ and the sum can be evaluated. The resulting expression for the pressure is

$$p = c \int_{C_p} V'^{-\frac{\theta_w}{2\pi}} (T_- - T_+) d\xi / 2\pi\theta_w \sqrt{r r_0} \quad , \quad (4.14)$$

where

$$T_{\pm} = (\cos \chi_{\pm} - V) / (1 - 2V \cos \chi_{\pm} + V) \quad , \quad (4.15)$$

$$\chi_{\pm} = \pi(\theta + \theta_0) / \theta_w \quad .$$

To transform Equation (4.5), an integral representation for the Legendre function of the second kind is used

$$Q_{\nu_n - \frac{1}{2}}(-A) = \int_0^{\infty} (-A + \sqrt{A^2 - 1} \cosh \xi)^{-\nu_n - \frac{1}{2}} d\xi \quad . \quad (4.16)$$

For the region of validity of Equation (4.5), there are no problems with branch cuts except for selecting the overall sign of the $-\nu_n - 1/2$ root. The easiest way to pick the proper sign is by analytic continuation, which, in this case, amounts to matching the two pressure expressions at $ct = r + r_0$. The negative root is the proper one.

Otherwise, the transformation is identical to the previous one and the result is

$$p = c/2\pi\theta_w\sqrt{\tau\tau_0} \cdot \int_0^\infty (V')' + \frac{\theta_w}{2\pi} (T_{--} + T_{-+} - T_{+-} - T_{++}) d\xi, \quad (4.17)$$

where

$$V' = (-A + \sqrt{A^2 - 1} \cosh \xi)^{-\pi/\theta_w}. \quad (4.18)$$

Here, T is identical in form to Equation (4.15) with

$$\chi_{\pm\pm} = \pi(\theta \pm \theta_0 \pm \pi)/\theta_w. \quad (4.19)$$

The solution is now formally complete; however, the computation of the infinite integral in Equation (4.17) is easier in two stages. First, the integration is performed numerically from 0 to some large ξ_L . Then, the remaining section is evaluated by approximating the integrand for large ξ

$$P_B = c(\cos \chi_{--} + \cos \chi_{-+} - \cos \chi_{+-} - \cos \chi_{++}) / 2\pi\theta_w \sqrt{r r_0} \cdot \int_{\xi_1}^{\infty} \left(2 \exp(-\xi) / \sqrt{A^2 - 1} \right)^{\frac{\pi}{\theta_w} + \frac{1}{2}} d\xi \quad (4.20)$$

This integration can be performed with the result that

$$P_B = \frac{2c \sin(\pi\theta/\theta_w) \sin(\pi\theta_0/\theta_w) \exp[-\xi_1(\frac{\pi}{\theta_w} + \frac{1}{2})] \cos(\pi^2/\theta_w)}{\pi \theta_w (\frac{\pi}{\theta_w} + \frac{1}{2}) \sqrt{r r_0} [(A^2 - 1)/4]^{\pi/2\theta_w + 1/4}} \quad (4.21)$$

A practical choice for ξ_1 is 10 and the step size for numerical integration from 0 to ξ_1 can be surprisingly large (0.5 was used with simple trapezoidal integration in the example below).

4.2.2 Comparison with finite-difference model

In Figure 10, the time-domain waveform calculated by the finite-difference method is compared to that calculated by the integral solution for a $3\pi/2$ pressure-release wedge. The receiver point is well within the shadow. Since Equations (4.14) and (4.17) assume an impulse source, the results from these calculations have been convolved with the source driver waveform, Equation (4.2), used in the finite-difference method.

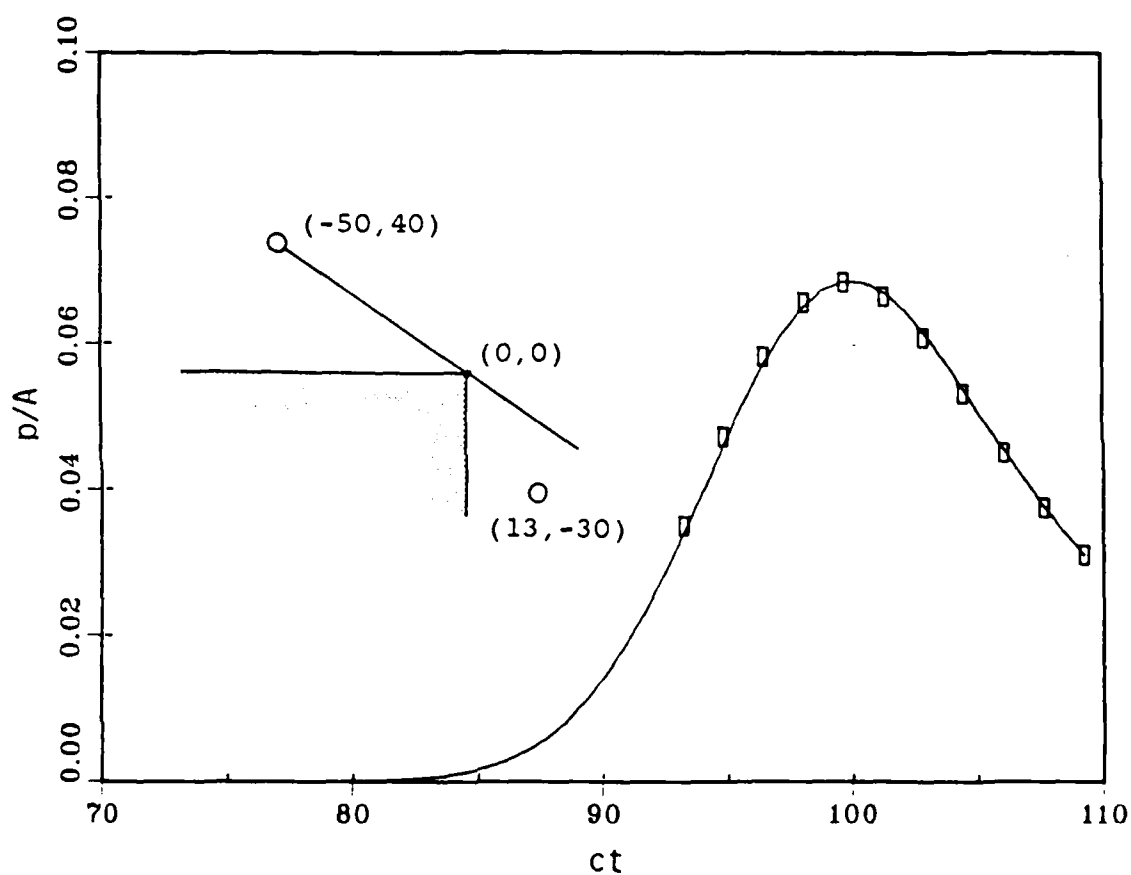


Figure 10. Diffraction into the shadow of a pressure-release wedge. Finite-difference calculation is shown as a solid line while the boxes give several points from the integral solution. Inset gives the x and y coordinates of the source and receiver.

Several other receiver locations were evaluated, all with equally good results. As noted before, both long wavelength diffraction into shadows and two-dimensional diffusion must be handled accurately for these results to agree so well.

4.3 Focusing at Simple and Cusped Caustics

Up to this point, the validation tests have centered on those wave effects not related directly to refraction. Since the region of interest in this study is one of strong refractive focusing, a test of the finite-difference method under these conditions is essential. An appropriate comparison solution for this task is a normal-mode solution. Some of the problems in using a superposition of single-frequency solutions to check a time-domain solution will become evident in this section. Nevertheless, reasonably successful comparisons are possible.

For these comparisons, the sound-speed profile shown in Figure 1 was used and perfect, pressure-release boundary conditions were applied at the upper and lower boundaries in both the finite-difference model and the normal-mode model. Since the boundaries are perfectly reflecting, the normal-mode solution predicts infinite-Q resonances; these would not, of course, be described by any time-limited solution. In order to avoid this mismatch, a very small amount of attenuation was added to the modes with ray-equivalent angles greater than 85 degrees from the horizontal. Also, because the driver is a transient and the range is relatively short, low-frequency evanescent modes were included in the solution.

Figure 11 shows the predictions of the mode model (dashed lines) and the finite-difference model (solid lines) at a cusp (upper plot) and on a simple caustic (lower plot). Overall, the agreement shown is excellent. Notice that, at the upper end of the spectrum, the curves are shifted slightly. This is evidence of the phase errors introduced by numerical dispersion in the finite-difference method. More than 4000 modes are included in the normal-mode solutions shown in these figures. If the evanescent modes are neglected, the spectra differ markedly. Also, without the attenuation applied to the higher order modes, very large peaks appear at several frequencies in the mode curve.

The efforts of this section underscore some of the problems associated with computing time-dependent solutions by Fourier superposition of single-frequency solutions. Two fundamental problems limit the accuracy of such calculation. The first is the reciprocal relation of frequency resolution and signal time duration. Many, closely spaced single-frequency solutions are required if a long time duration is expected in the signal.

The second problem has its roots in the type of equation being solved. The single-frequency solution is a solution to an elliptic differential equation (the Helmholtz equation) and, therefore, the entire space must be considered out to all boundaries including those at infinity. A change anywhere in the space changes the solution so some care must be exercised in selecting boundary conditions even if the real time-dependent signal would not reach those boundaries during the observation period. The time-dependent solution is the solution of a hyperbolic equation (the wave equation) and its progression follows the ad-

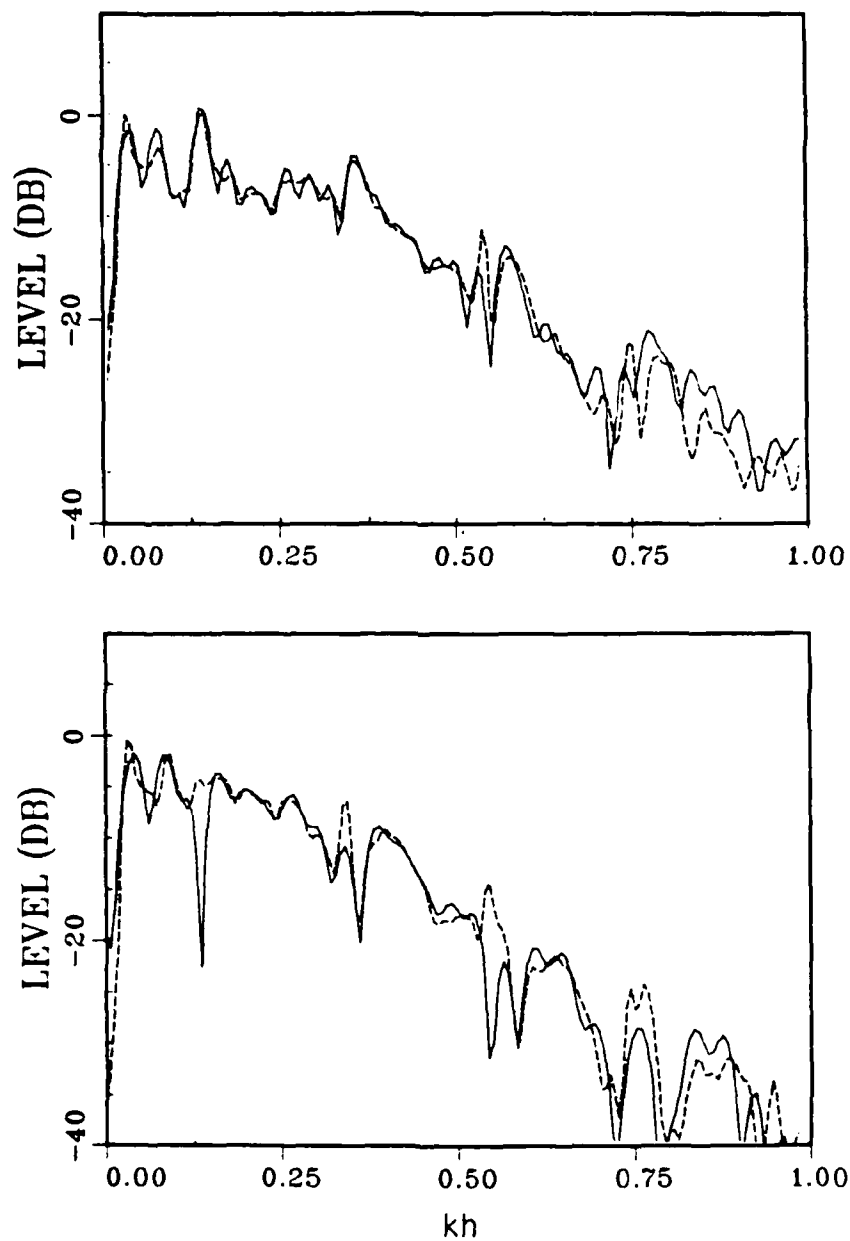


Figure 11. Comparison of finite-difference (solid lines) and normal-mode (dashed lines) solutions. Upper plot shows the field level (arbitrary reference) at a cusp while lower plot gives the level on a simple caustic.

vance of the physical wavefront: conditions outside this envelope do not affect the solution in any way. This conflict shows up in the apparently perfect resonances in the mode solution for ideal boundaries.

4.4 Limitations of the Finite-difference Solution

The most serious limitation of the finite-difference technique is the dispersion that forces a relationship between step size and maximum frequency. At about five points per wavelength (about 30Hz in the atmospheric problem considered later), the distortion becomes noticeable. This should be true in any application of the method so, given the maximum frequency and the minimum sound speed (to get the minimum wavelength) the grid size is fixed. In pushing the limiting frequency upwards, be aware that the running time increases as the linear density of grid points cubed since the time step must also be decreased as the grid spacing decreases.

The low-frequency limit is forced by imperfections in the transparent-boundary condition. As shown in Figure 8, this limit is kh roughly equal to 0.075 (about 2Hz for the atmosphere problem). If another type of boundary such as a rigid or pressure-release boundary is acceptable, this limit would be much lower. It could also be lowered by moving the boundary farther away at some increase in cost: doubling the distance to the boundary would only double the computation time.

Given these limitations (primarily economic), the finite-difference scheme is well suited for impulse studies in two-dimensions. Wave effects are accurately represented and large range variations as well as depth variations in sound speed and boundary geometry are easily accommodated.

Chapter V

SOLUTION CONTEXT

Focusing of waves occurs frequently in nature and, in a number of these cases, the relevant frequencies can be in the range of strong diffraction. For acoustic waves in the atmosphere, focusing can take place over distances ranging from less than a hundred meters to thousands of kilometers. Intense temperature inversions over snow coupled with wind shear can produce dramatic short range focusing (Thomson, 1984). In this case, the caustics would only be separated by a few meters and strong diffraction could extend to several hundred hertz. At the other extreme, acoustic waves from the SST (Weber and Donn, 1982) or meteors (Bedard and Greene, 1981) can be focused by strong temperature gradients in the thermosphere although here the focusing region may be on the order of 1000km from the source and strong diffraction would only be observed for extremely low frequencies (well below 1Hz). Of intermediate scale is focusing by wind shear in the atmospheric or planetary boundary layer (PBL).

Also, short and long range focusing in the ocean results from, for example, surface ducts or the SOFAR channel (Urick, 1979). Oceanic sound speed is four to five times higher than sound speed in the atmosphere so, for the same range scales, the upper limit in frequency for strong diffraction in the ocean is four to five times higher in the ocean than in the atmosphere.

At very low frequencies, ionospheric refraction of electromagnetic radiation (Brekhovskikh, 1980) can be strongly diffractive. At very high frequencies, refraction and focusing that create optical mirages (Fraser and Mach, 1976) would normally be well represented by simple asymptotic correction to ray theory.

5.1 Focusing in the Planetary Boundary Layer

While focusing in a stratified medium could be analyzed in a general way with normalized distances and frequencies, the introduction of realistic levels of perturbations depends on the specific environment being studied. In order to consider a useful perturbation problem and to be able to assign values to parameters, a specific problem is examined here: short-range focusing in the PBL. All of the general results are, however, still applicable to any strongly diffractive focusing environment.

5.1.1 Effects of wind on sound speed

Because bulk flow (wind) in the atmosphere is not generally negligible compared to the speed of sound, the wave equation must account for these flow effects. We could combine Equations (2.4) and (2.5) into a wave equation without dropping the bulk flow terms but it will be easier to include a simplifying assumption if we instead compute the implied dispersion relationship. By substituting time-harmonic expressions for p and \vec{v} (through a velocity potential), we can find the condition that allows non-trivial solution of the coupled Equations (2.4) and (2.5)

$$\omega/k = c + \vec{v}_0 \cdot \vec{k}/k, \quad (5.1)$$

where \vec{k} is the wave number vector and ω is the angular frequency. In other words, Equation (5.1) gives an effective sound speed.

In the atmosphere, the bulk flow is primarily horizontal and the rays are nearly horizontal particularly at the altitudes of the higher wind speeds. Thus, we can write an approximate relation for the effective sound speed

$$c_{eff} = c + U, \quad (5.2)$$

where U is the component of the wind in the direction of propagation. This effective sound speed is used directly in the usual time-dependent wave Equation (2.6).

Since air behaves very nearly as an ideal (albeit composite) gas, the expression for c is simply

$$c^2 = \gamma RT/M, \quad (5.3)$$

where, for air, $\gamma = 1.4$, $R = 8.31 \text{ J/mol} \cdot \text{K}$ and $M = 0.029 \text{ kg/mol}$ so that

$$c = 20.0 \sqrt{T} , \quad (5.4)$$

where T is the Kelvin temperature. At this point, we will cease to label c as effective and understand that the sound speed is given by

$$c = 20.0 \sqrt{T} + U , \quad (5.5)$$

where, as before, U is the downrange component of the wind speed.

5.1.2 The planetary boundary layer

Thermal and mechanical effects of the ground on atmospheric flow are confined to a region of flow transition known as the planetary boundary layer or PBL (Panofsky and Dutton, 1984). In this region, the wind makes the transition from a flow that is dominated by surface friction effects to one that is undisturbed at the altitude corresponding to the top of the PBL. Also, the structure and dynamics of the PBL depend strongly on the convection induced by ground heating. When the temperature decreases sufficiently fast with altitude so that a rising (and, hence, adiabatically cooling) parcel of air maintains buoyancy, ground-heated air will be vertically convected and disturb the horizontal flow to altitudes of up to one or two thousand meters. This is typical of a daytime neutral or slightly unstable PBL.

When the temperature profile is such that convection is suppressed as is normally the case at night as a result of radiative cooling of the surface, the transition layer effects are primarily surface friction and mechanically induced turbulence. In this case, the PBL is much thinner, perhaps only a few ten's or at most a few hundred's of meters. In this condition of stable flow, strong, infrequently turbulent winds aloft are common and the usual positive gradient in wind speed with altitude adds to that of the temperature gradient and causes strong downward refraction and focusing of sound.

In order to determine the dominant features of a particular PBL, the stability with regard to vertical convection must be determined. If a small parcel of air is displaced vertically, it may continue to move upward through its own buoyancy (in an unstable layer) or it may oscillate about its rest position at some frequency (in a stable layer). This frequency is known as the Brunt-Vaisala frequency (for example, see Beer, 1974). For a perfect gas, it is

$$\omega_B^2 = g(\alpha - \alpha^*)/T, \quad (5.6)$$

where α is the vertical temperature gradient, α^* is the adiabatic gradient (-0.0098 K/m), and g is the acceleration of gravity. If ω_B^2 is negative, the layer is unstable and thermal convection can cause mixing throughout the layer; if ω_B^2 is positive then the flow in the layer is stable and gravity waves can form.

In a convectively unstable PBL, the Richardson number describes turbulence maintenance (Schlichting, 1979). This number is the ratio of buoyant production of turbulence-related kinetic energy to shear-stress production of turbulent kinetic energy and, in terms of ω_B^2 is

$$R_i = \omega_B^2 / (\partial U / \partial z)^2, \quad (5.7)$$

where U is the horizontal wind speed. If R_i is greater than about 0.25, turbulence is suppressed. For R_i less than zero, convective turbulence dominates and, in between, shear-produced turbulence dominates.

Figure 12 shows the meteorological parameters that characterize the PBL at a time of strong focusing (Brown, 1980 and Thomson, 1983). These parameters were measured using tethered, instrumented balloons by the University of Virginia to support noise interference studies for the DOE/NASA Mod-1 wind turbine generator near Boone, North Carolina. The figure shows a typical nighttime stable flow. Except for a small, elevated layer (from 75m to 85m altitude), the flow is stable. In fact, it is strongly stable ($R_i \gg 0.25$) in the first 50m so that any thermal convection from the ground would be strongly suppressed. Also, a strong vertical wind-speed gradient exists above the surface layer.

For this particular PBL, the maximum Brunt-Vaisala frequency corresponds to a period of 200 seconds. Consequently, there will be no measurable coupling between gravity waves and acoustic waves and the gravity terms can be safely omitted (as we have already done) from the governing equations.

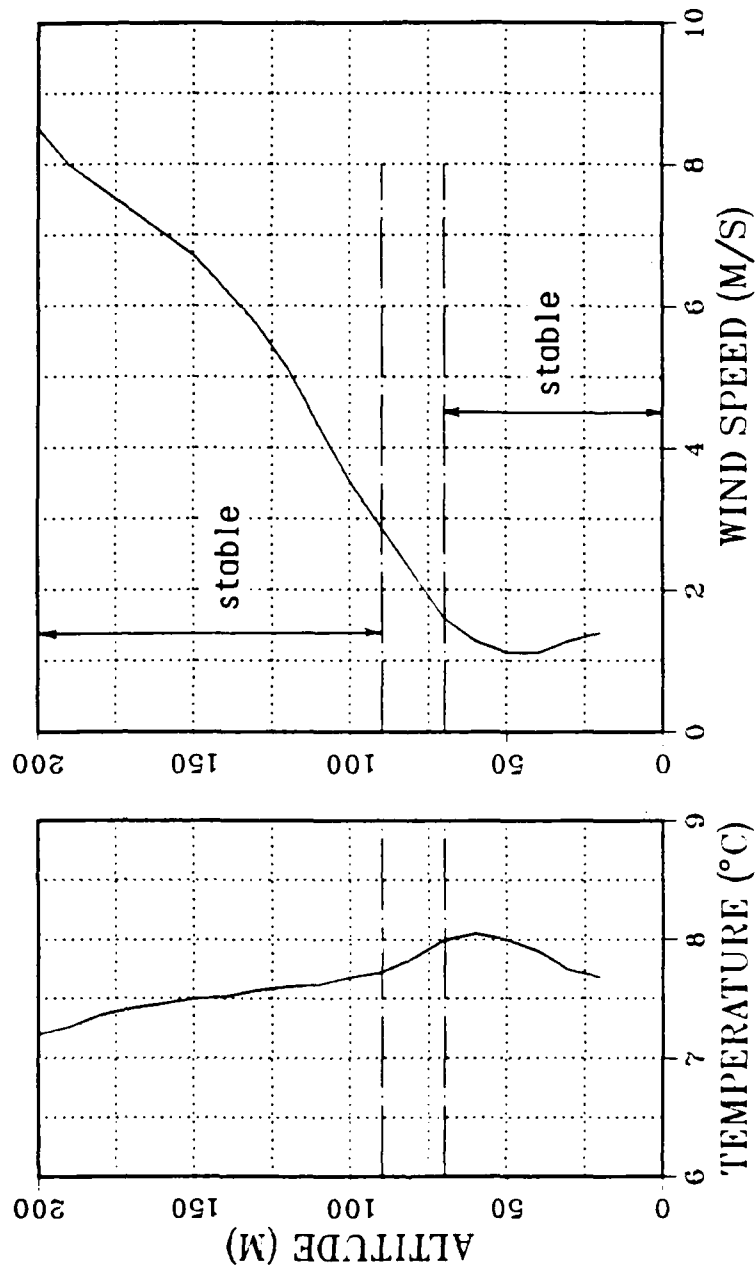


Figure 12. Measured temperature and wind speed profiles for a period of strong focusing in the planetary boundary layer.

Figure 13 shows the sound-speed profile for the meteorological conditions of Figure 12 including the envelope of perturbations. (This envelope is described in section 5.2.) Although the finite-difference model can accept an arbitrary profile, in order to facilitate comparison to normal-mode and ray models, two layers are used to fit the environmental data. Each layer has a linear variation in the square of the reciprocal of the sound speed. This turns out to be an excellent fit for the upper, steep-gradient layer.

Although the frequency range of the investigation to follow is so low as to render analysis by ray theory questionable at best, some insight into the focusing produced by this profile can be gained from the ray diagram in Figure 14. The three limbs of the caustic (and the two cusps) are shown in Figure 15 along with the observation points used in Chapters VI and VII. Three general areas are examined with these points: the transition from the illuminated side of a simple caustic to the shadow side; the field between two closely spaced caustics; and the near-ground field before and near one of the cusps.

5.2 Perturbation Model

There are many possible processes that can produce large scale horizontal inhomogeneities in the atmospheric boundary layer. One common phenomenon under stable conditions is gravity wave formation. In complex terrain such as the region surrounding the wind turbine generator at Boone, North Carolina, mechanically induced turbulence is often formed in the lee of the ridge. For this investigation, we will choose the turbulence mechanism.

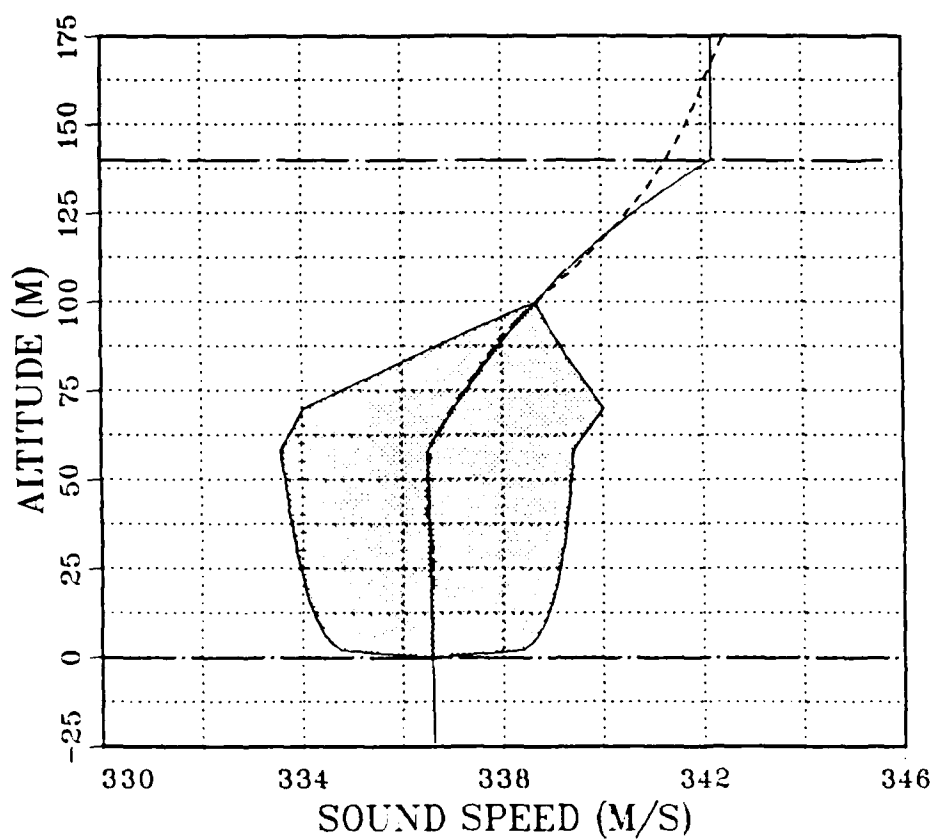


Figure 13. Sound-speed profile (dashed line) corresponding to temperature and wind speed profiles in Figure 12. Solid line shows profile used in finite-difference model and shaded region gives envelope of sound-speed perturbations.

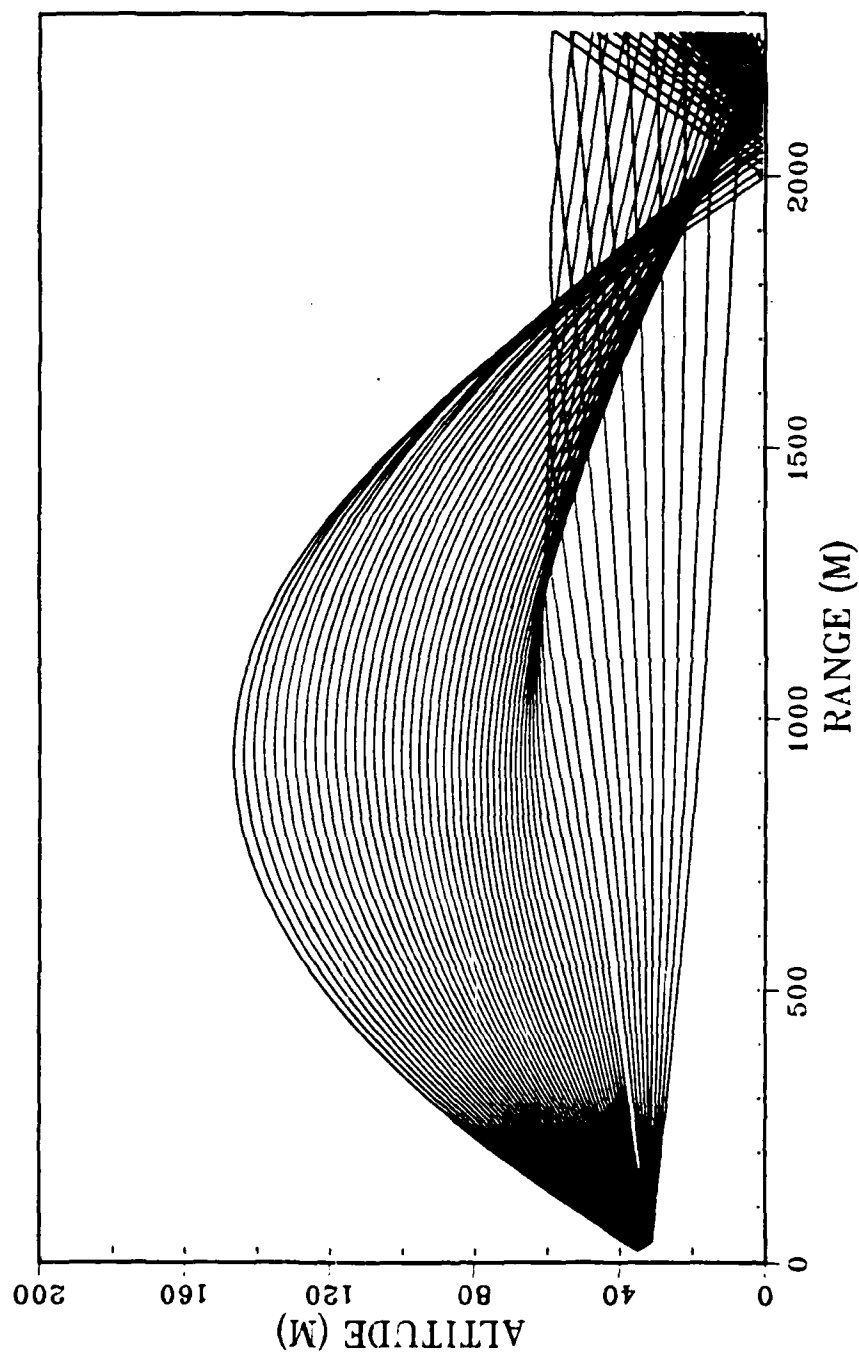


Figure 14. Ray diagram for sound-speed profile in Figure 13 (solid line). Altitude of source is 31m.

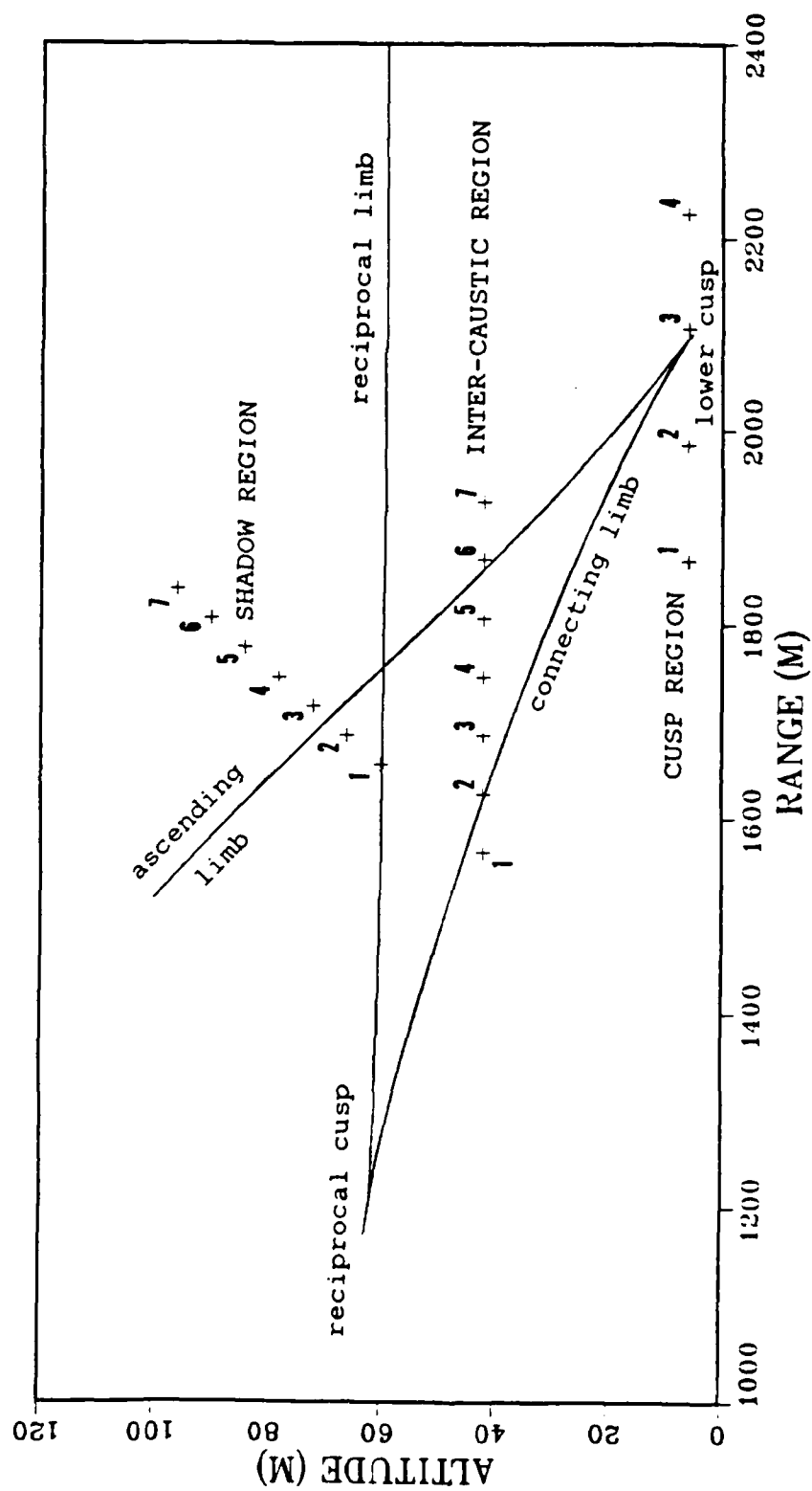


Figure 15. Location of ray-theory caustics (solid lines) and groups of observation points (crosses).

A detailed model describing such turbulence in detail would be prohibitively complex if indeed at all possible; however, since we are not seeking to duplicate one particular flow condition but rather to describe the general nature of signal fluctuations, a simple but not unrealistic model will suffice. An artificially introduced perturbation component of the observed wind is shown in Figure 16. The lower part is the normal power-law profile (Tennekes and Lumley, 1972) typical of turbulent boundary flows. This is, in fact, the same power-law that is used to extend the measured profile of the unperturbed wind to the ground. (In other words, the power-law applies to the sum of the perturbation component and the unperturbed wind.) This power-law section extends to the top of the temperature inversion (70m) shown in Figure 12. Above this region, there is no particular theoretical basis for the profile but observations (Thomson, 1984) suggest that a 30m layer of linearly decreasing perturbation speed is not unreasonable. This perturbation profile is modulated sinusoidally in range with a period of 140m or twice the characteristic height and then added to the steady-state wind profile of Figure 12. In addition, the perturbation pattern is advected downwind at the minimum wind speed in the upper part of the surface layer (1.5m/s). Since temperature variations have a negligible effect on the sound-speed profile (in this case), the steady-state temperature profile is used without perturbation.

The perturbed wind speed is then given by

$$U(x,z) = U_0(z) + u(z) \cos [\pi(x + v_a t)/\hat{z}] \quad , \quad (5.8)$$

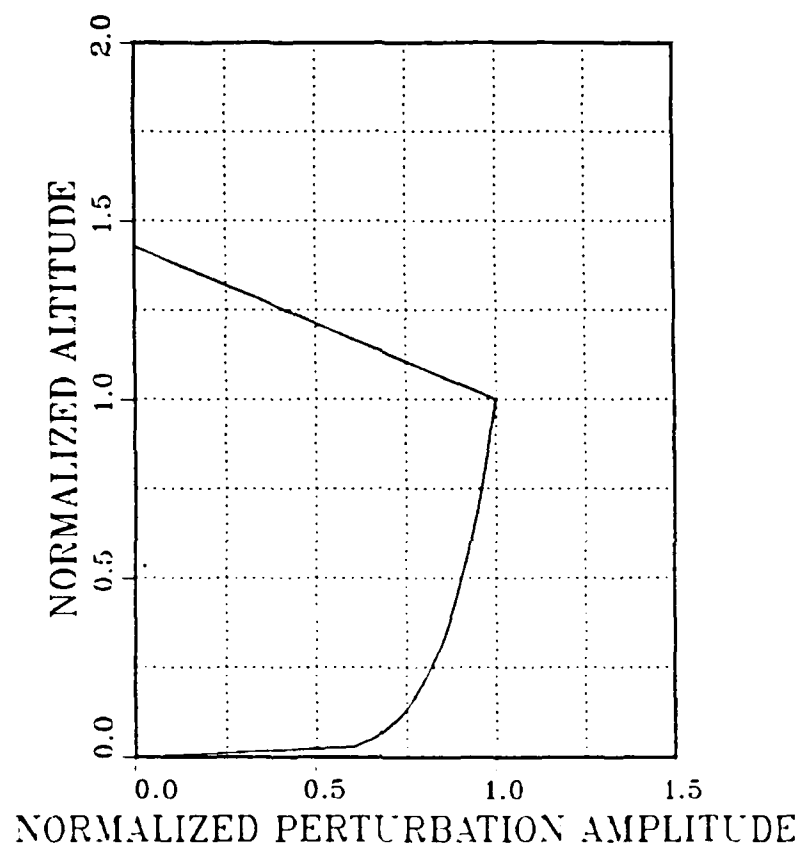


Figure 16. Vertical distribution of normalized perturbation component u/\hat{u} . Vertical scale is z/\hat{z} .

where $U_0(z)$ is the steady-state wind profile, $u(z)$ is the perturbation amplitude profile, \hat{z} is the characteristic height (70m), and v_a is the advection speed (1.5m/s). Also

$$u(z) = \begin{cases} \hat{u}(z/\hat{z})^{1/7} & ; \quad (0 < z < \hat{z}) , \\ \hat{u}(\hat{z} - z + 30)/30 & ; \quad (\hat{z} < z < \hat{z} + 30) , \\ 0 & ; \quad (\hat{z} + 30 < z) , \end{cases} \quad (5.9)$$

where \hat{u} is the perturbation level at \hat{z} . For this particular profile, the wind direction did not vary significantly so any directional corrections are ignored and directly downwind propagation is assumed.

5.3 Source Characteristics

The source used in this study simulates a line array of WTG's (as might be the case at a wind farm rather than an isolated turbine) by using a line source. This is a crude representation since the turbines would not normally be rotating in phase; however, this will serve to simulate a worst-case, on-axis beam. In the finite-difference model, the line source is introduced by using a point source in a two-dimensional Cartesian coordinate system.

At the Boone installation, an annoying sound was produced by passage of the blade through the turbulent wake of the supporting tower (Kelley, 1981)). To simulate this, a narrow impulsive source waveform is used that has a broad spectrum (see Equations (4.2) and (4.3)). The Mod-1

wind turbine generator (WTG) blade rotated at 35rpm so approximately one pulse per second was produced. Consequently, there will be a rapid drop in source level below 1Hz.

According to measurements by Kelley et al. (1982), the part of the received WTG signal that was above the noise at the affected dwellings was bandlimited below 25Hz. Since this range is entirely subaudible, the annoyance was apparently a result of excitation of the natural vibrational modes (at approximately 5, 12 and 20Hz) of the human body (Tempest, 1976). The incoming acoustic energy did not directly couple the modes (the "noise" was not generally objectionable outside the houses) but, instead, it excited diaphragm modes in the floors and walls and these, in turn, produced annoyances to the residents.

5.4 Configuration for the PBL Model

Since the mechanics of the finite-difference method have been developed in Chapter III, a particular model can now be configured for the PBL problem. In order to maximize computational efficiency, the range coordinate is transformed by gradient scaling (see Appendix B). In the atmosphere, as in the ocean, range scales are generally larger than height scales but an approximately square grid is more efficient for calculation. In this case, a 5-to-1 range compression is used so that the resulting grid of 70 by 225 (2m spacing) represents 140m in altitude and 2250m in true range.

Because of this gradient scaling, the highest sound speed in the field rises to 480m/s. In order to limit q to no more than 0.8 anywhere in the field, the maximum time step is 0.00333s. Notice that, in the

unscaled case, this maximum would be 0.00435s. This loss in time advance per step is far outweighed by having to cover only one-fifth the distance downrange.

The source is located at 31m above the ground. This position was selected only to provide a clean caustic region; it is otherwise arbitrary. Since the purpose of this study is to examine only aspects of the propagation rather than simulating the Boone situation per se, no attempt was made to include features such as actual topography or surface impedances.

Source points traditionally cause problems in finite-difference schemes (e.g., Alterman and Karal, 1968). This is avoided here by defining a fairly large source region (40m in radius from the source) and computing the source field analytically at two consecutive time steps. These starter fields are then used as initial conditions. A very accurate representation of the source is possible if the peak of the source pulse is put about halfway out into this source region (i.e., $ct_0 = 20$ in this case). Hence, a start time of 0.059s is used here.

Dispersion is controlled by proper selection of source bandwidth and grid spacing. These two parameters determine kh and this can be set according to the dispersion curve in Figure 6. The choice of 2m for h was made in order to keep kh below $\pi/3$ up to 25Hz. Source bandwidth is controlled by b in Equation (4.3). A value of 82.82 for b reduces the source amplitude by a factor of ten at 20Hz and by a factor of 400 at 30Hz.

The final element in the PBL configuration is the transparent-boundary condition. Since this investigation is concerned primarily with re-

fractive focusing, interfering multipath from simple reflection is avoided by using Reynolds' (1978) method for transparent boundaries. A summary of this condition is contained in Appendix A. The lower limit on kh imposed by defects in the transparent-boundary condition is, according to Chapter IV, 0.075, which is about 2Hz in this case. Rigid and pressure-release boundaries are, of course, much easier to insert.

If a different problem is to be modeled, the design process would proceed as follows:

1. determine the maximum frequency of interest and select b so that the source spectrum drops below one percent somewhat higher than this frequency;
2. based on the minimum sound speed, compute the required grid spacing h for kh less than $\pi/3$ at the maximum frequency;
3. select a time step so that q is no greater than 0.8 at the maximum sound speed;
4. define a source region with a radius of about $20h$ and pre-calculate the starter fields within this region at a time equal to half this radius divided by the local sound speed;
5. select appropriate boundary conditions.

The fastest computations are possible if the entire solution grid at three consecutive time steps can be kept in memory, but, since the technique is explicit, this is not a requirement. Pieces of the grid can be swapped in and out of active memory if the overall grid size is very large.

The model of atmospheric structure used here takes about half a megabyte of storage on an IBM 3033 so no memory swapping is required. One

of the outstanding features of the finite-difference method for studies of large regions of the field is that the solution is obtained at every grid point, not just a few selected receiver points. A normal-mode solution for a simple two-layer model is only cheaper than the finite-difference model for less than 20 receiver points.

Chapter VI

STRUCTURE OF THE UNPERTURBED FIELD

Before the influence of sound-speed perturbations can be assessed, the structure of the unperturbed field must be understood. This underlying structure not only determines the nature of diffraction near a wave convergence but also affects the response of the field to perturbations. Consequently, some effort is spent in this chapter to examine the field structure in the context of diffractive wave phenomena.

6.1 Overall Field Structure

In order to reinforce the distinction between a strongly diffractive field and its asymptotic (high-frequency) limit given by ray theory, let us first examine the overall field in the multiple caustic region.

Consider the ray picture shown in Figure 14. According to the ray diagram, the region of focusing consists of three distinct limbs of a caustic joined by two cusps. This structure is delineated in Figure 15. The strongest limb is the ascending limb while the weakest (by far) is the almost-horizontal reciprocal limb. (The strengths are apparent from the line density in the plot but these qualitative statements were verified by ray theory calculations with first-order caustic corrections.) The almost horizontal limb and the associated cusp are called "reciprocal" because they occur at about the reciprocal altitude or the altitude in the upper layer that has the same sound speed as the source does in

the lower layer. A shadow is formed in the area to the right of the ascending limb and above the reciprocal limb. There is another shadow to the left and below the connecting limb but this is not pure shadow because direct rays weakly ensonify the region. Also, the lower cusp appears to be particularly intense.

Because the wavelengths considered here are of the order of the caustic spacing, conclusions based on this ray picture (or on a ray trace calculation) can be quite misleading. To demonstrate this, Figures 17, 18, and 19 were constructed from the results of the two-layer normal-mode model described in the previous chapter. (The finite-difference results could also have been used.) The caustic limbs are superimposed on these contour plots as dashed lines. The contour lines represent lines of equal field level relative to free-field spreading and the contour increment is 3dB. In all cases, the actual wave field bears only a casual resemblance to the ray structure.

The results at 5Hz are particularly striking: the contoured field in Figure 17 shows a smooth, broad ridge roughly centered over the multiple caustic and approximately parallel to the ascending limb. The only hint of the multiple caustic structure is the slight upturn in the contour lines at the far right near the reciprocal limb. There is no indication at all of the lower cusp while the presence of the upper (reciprocal) cusp merely fills in the upper end of the valley to the left of and paralleling the focal ridge. The two major depressions correspond to the shadow regions of the ascending and connecting limbs. Obviously, if the caustic structure were not already known from ray tracing, it could not be inferred in any detail from the field contour plot.

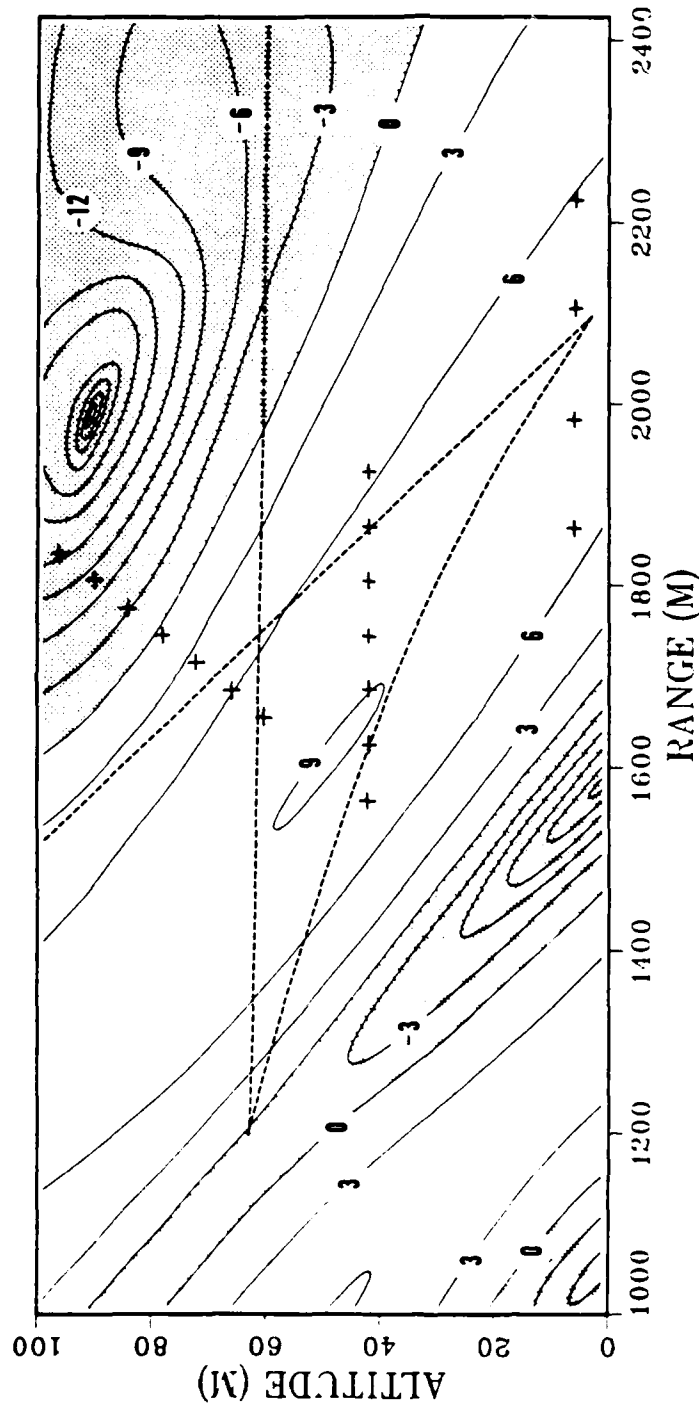


Figure 17. Field in the vicinity of the multiple caustic (5Hz).
 Contours show gain in dB with respect to free-field spreading.
 Dashed line shows caustic and crosses indicate observation points as
 in Figure 15.

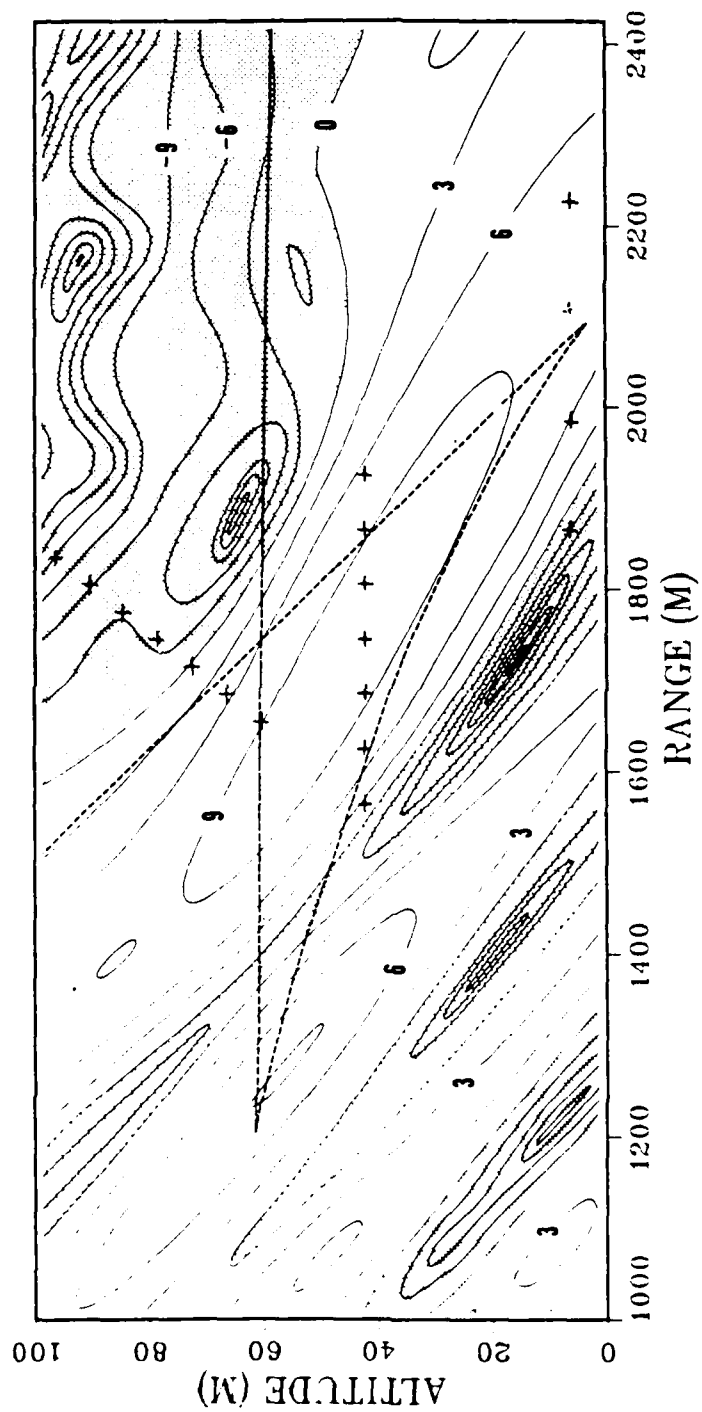


Figure 18. Field in the vicinity of the multiple caustic (10Hz).

AD-A171 220

EFFECTS OF STRONG DIFFRACTION ON THE FOCUSING AND
SCATTERING OF ACOUSTIC WAVES (U) PENNSYLVANIA STATE UNIV
STATE COLLEGE APPLIED RESEARCH LAB
I B GABRIELSON ET AL. JUN 86 IR-86-004

2/2

UNCLASSIFIED

F/G 20/1

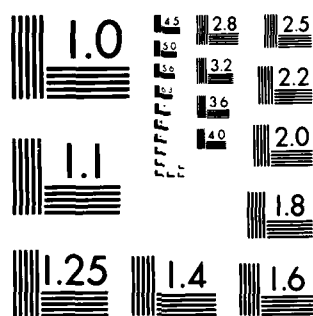
NL

END

DATE

FILED

10-86



MICROCOPY RESOLUTION TEST CHART
NATIONAL BUREAU OF STANDARDS-1963-A

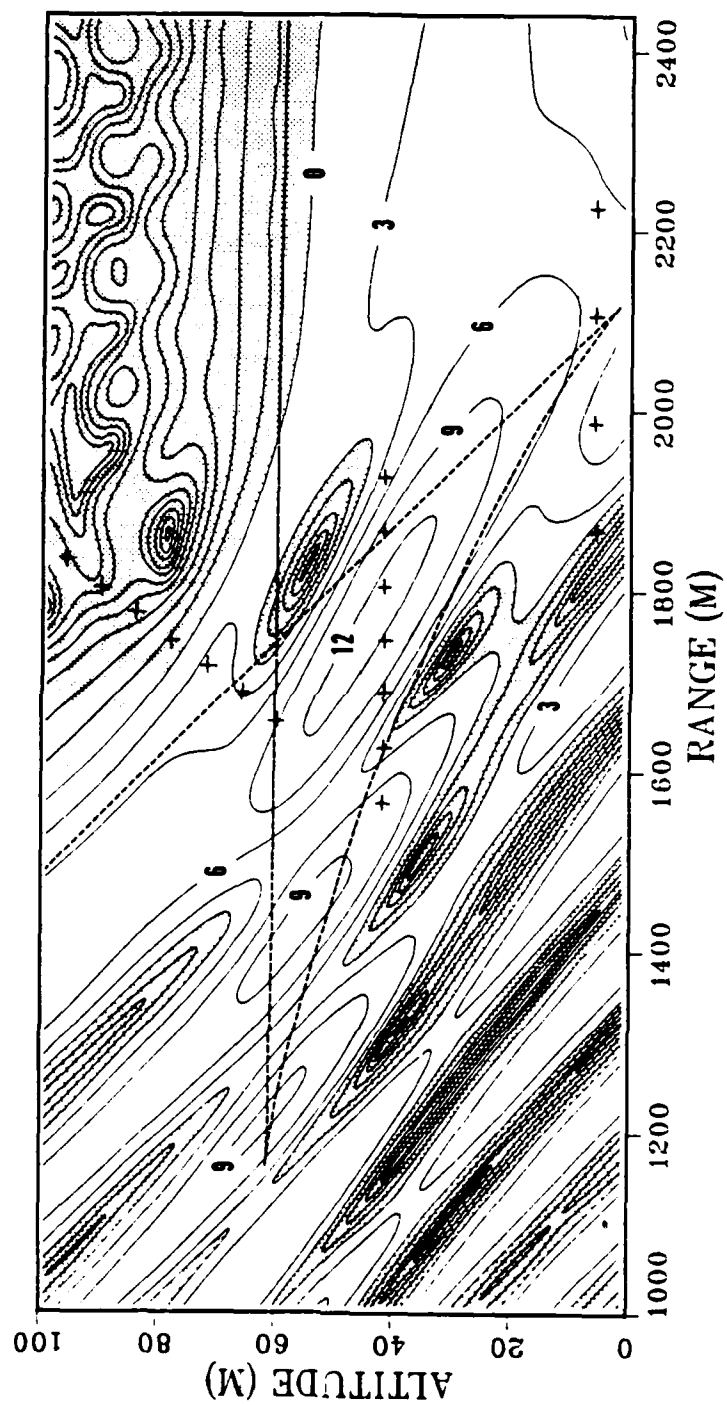


Figure 19. Field in the vicinity of the multiple caustic (20kHz).

The field plot at 10Hz, shown in Figure 18, delineates the weak reciprocal limb more clearly than at 5Hz, but there is, again, no indication that there are two other strong caustics. In fact, at both 5 and 10Hz, the field contour lines cut across the connecting limb at a high angle near the upper cusp. Simple asymptotic corrections to ray theory would trace the contours parallel to the caustic. As at 5Hz, the "strong" lower cusp does not show on the contour plot. Notice that in the upper right shadow region, the wave field is actually highly structured as if there were several interfering paths. In fact, there is more structure in this deep shadow than in the illuminated zone. Note that first-order asymptotic ray theory predicts a smooth, featureless decay into the shadow.

At 20Hz (Figure 19), the upper cusp and the wedge formed by that cusp and the connecting and reciprocal limbs are indicated by the two elliptical peaks. Again, the multiple caustic is represented predominantly by a long, single ridge paralleling the ascending limb. The dropoff into either shadow is faster but the upper right shadow still shows much more structure than the illuminated region between the limbs. Curiously enough, the lower cusp is still not a distinguishable feature of the wave field.

By quickly scanning Figures 17, 18, and 19 in order, the trend is clear. The wave field is slowly approaching the general shape of the convergence suggested by the ray trace. This would continue until, at very high frequency, the multiple caustic structure would be clearly defined and the interference pattern in the shadow would be generally destructive. Throughout the frequency range shown here, however, the ray representation is a very poor indication of the actual field.

In particular, the wave field structure is a generally featureless enhancement in the high intensity region while, in the shadow, there is a distinct interference structure. In the following analyses, the caustics will be used as reference lines to locate observation points in the field, but, as we have seen, they have little intrinsic significance at these frequencies.

6.2 Structure in the Shadow Zone

Since ray theory does not provide much information about the field structure at low frequency, we will use the wave results given by both the finite-difference method and normal-mode analysis. The shadow zone is, perhaps, the most interesting region since the greatest changes in signal characteristics occur there.

6.2.1 Finite-difference results

The finite-difference model produces the received time waveform directly for a pulsed source. Figure 20 shows the variation in the received waveform for the points in the set labelled "shadow zone" in Figure 15. The trace at the top is from a receiver well inside the illuminated zone and the shape is similar to the source pulse with an extended tail. This tail is a characteristic of two-dimensional spreading and appears in all of the pulse waveforms. As we penetrate the shadow zone (moving downward in Figure 20), the pulse flattens considerably and broadens slightly as if the initial single pulse were being split into two very closely spaced pulses of reduced amplitude. Another way of viewing the pulse change is that the high-frequency components

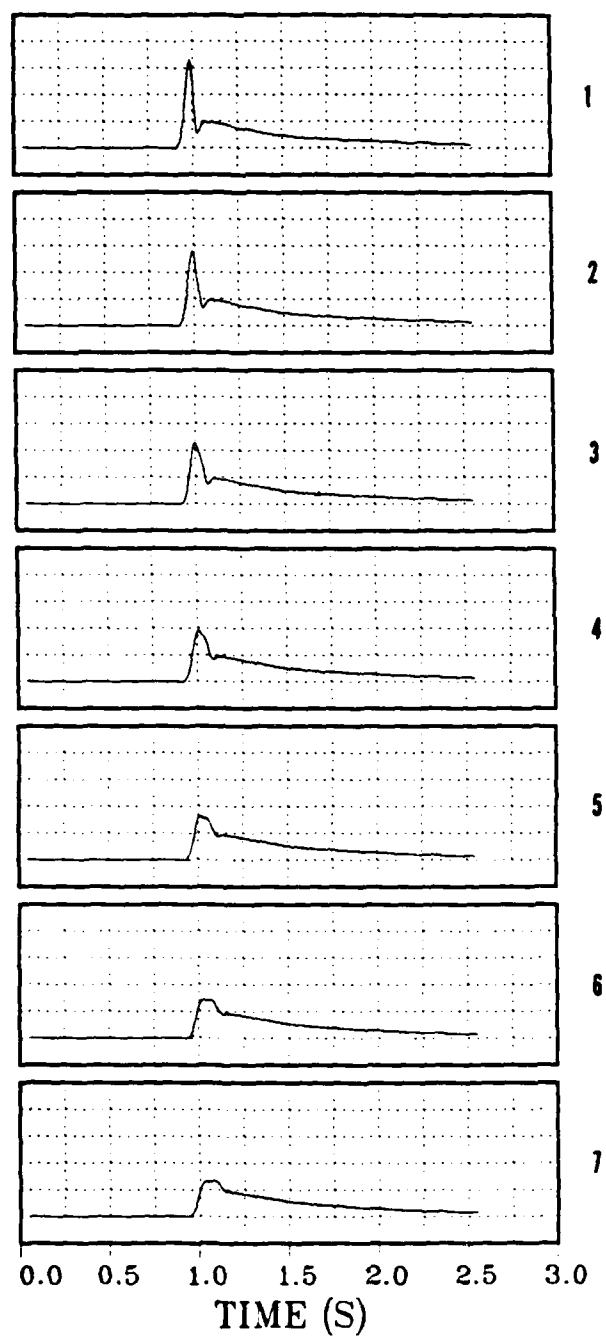


Figure 20. Finite-difference model predictions of pulse shape at receiver points 1 through 7 in shadow region. Point 7 is furthest into the classical shadow. Amplitude scale is linear but otherwise arbitrary.

are being lost more quickly deep in the shadow. As we will see, both of these interpretations are correct: there is some high-frequency rejection in the shadow and there is a significant multiple arrival structure in the shadow (in spite of the ray theory prediction that there are no arrivals here at all).

In Figure 21, the magnitude spectra for several of the shadow zone points are shown. The two principal features are the increasing amount of high frequency rejection with deeper penetration into the shadow and the changing interference pattern. As we progress into the shadow, the spectrum interference nulls become more closely spaced. The interference pattern is quite simple indicating only two or three major interfering components and the null shift indicates that the arrival time difference between the components is increasing with penetration into the shadow. In order to locate the cause of this interference, we must use another wave theory model: the normal-mode model.

6.2.2 Cumulative mode-sum analysis

A ray theory calculation considers the field to be the sum of all possible rays connecting the receiver to the source. The normal-mode method, on the other hand, develops the field as the sum of the permissible elementary waves determined by the boundary conditions. For a point source in a horizontally stratified medium, the elementary waves are cylindrical waves while, in this analysis for a line source, the elementary waves are plane waves. In either case, if we cut the field with a vertical plane parallel to the direction of propagation, we would see that each mode (elementary wave) would have its own wavefront and

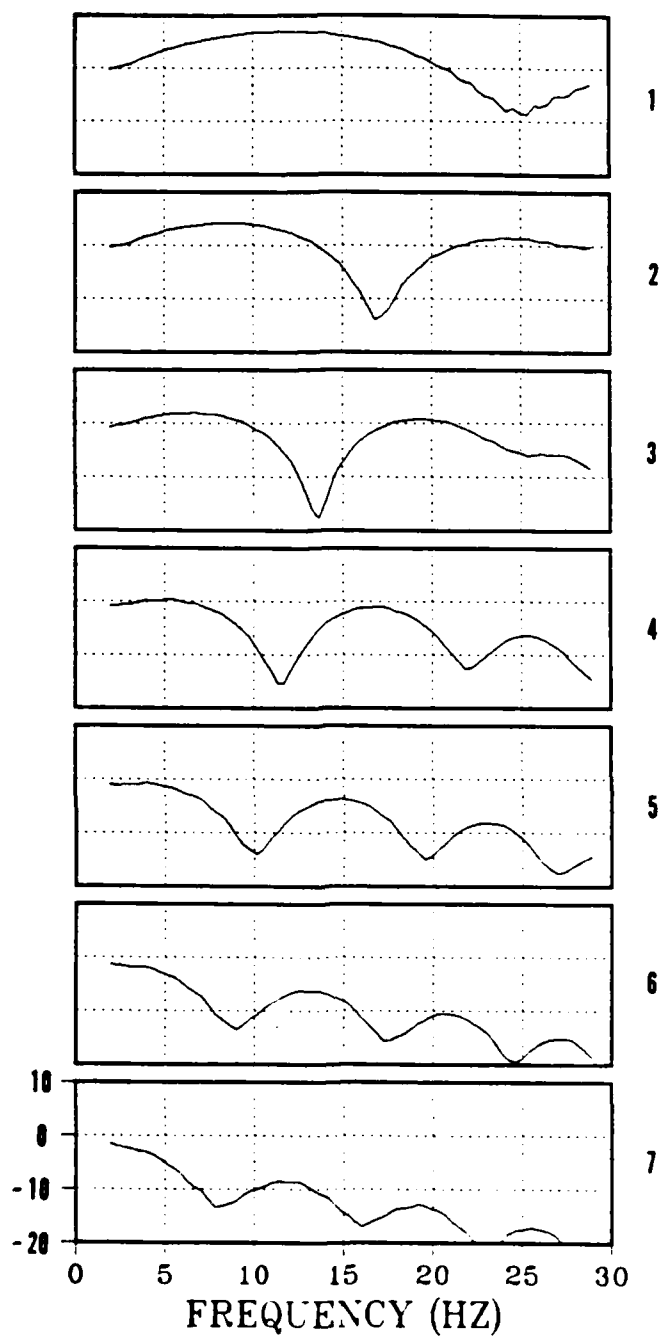


Figure 21. Spectra corresponding to the waveforms shown in Figure 20
Vertical scale is level (dB) relative to free-field spreading.

that these wavefronts would be curved by the sound-speed gradients. Equivalent rays could be drawn for each mode and they would be perpendicular to the wavefronts. In fact, at a high enough frequency, sets of modes can be isolated and summed to produce a field pattern that looks like a "fuzzy" ray path connecting the source and the receiver.

While the ray plot is useful for understanding the structure of weakly diffracted (high frequency) fields, the mode-sum plot is useful for interpreting the structure of both strong and weak diffraction. In this plot, the complex numbers representing each term in the mode sum (Equation (2.8)) are added and, after each term is added, the new partial sum is plotted on a grid with the real and imaginary parts as the two axes. In this way, the development or progression of the mode sum can be seen from the lowest order mode through the highest order mode.

Along some sections of this curve, the modes will appear to be combining haphazardly without contributing to the overall movement of the endpoint in the complex plane. Along other sections, the modes will be working together to produce generally straight progress (although often with superimposed wiggles) in some direction. In the first case, these modes are unimportant since they do not affect the final result much. In the second case, the groups contribute directly to the field strength, each group representing a specific component of the field. At high frequency, the groups are very well defined and, as we will see, these same structural features can be identified at low frequency as well.

Mode-sum plots for four of the shadow zone points at 20Hz are shown in Figure 22. Here, the highest-order modes near the end of each curve

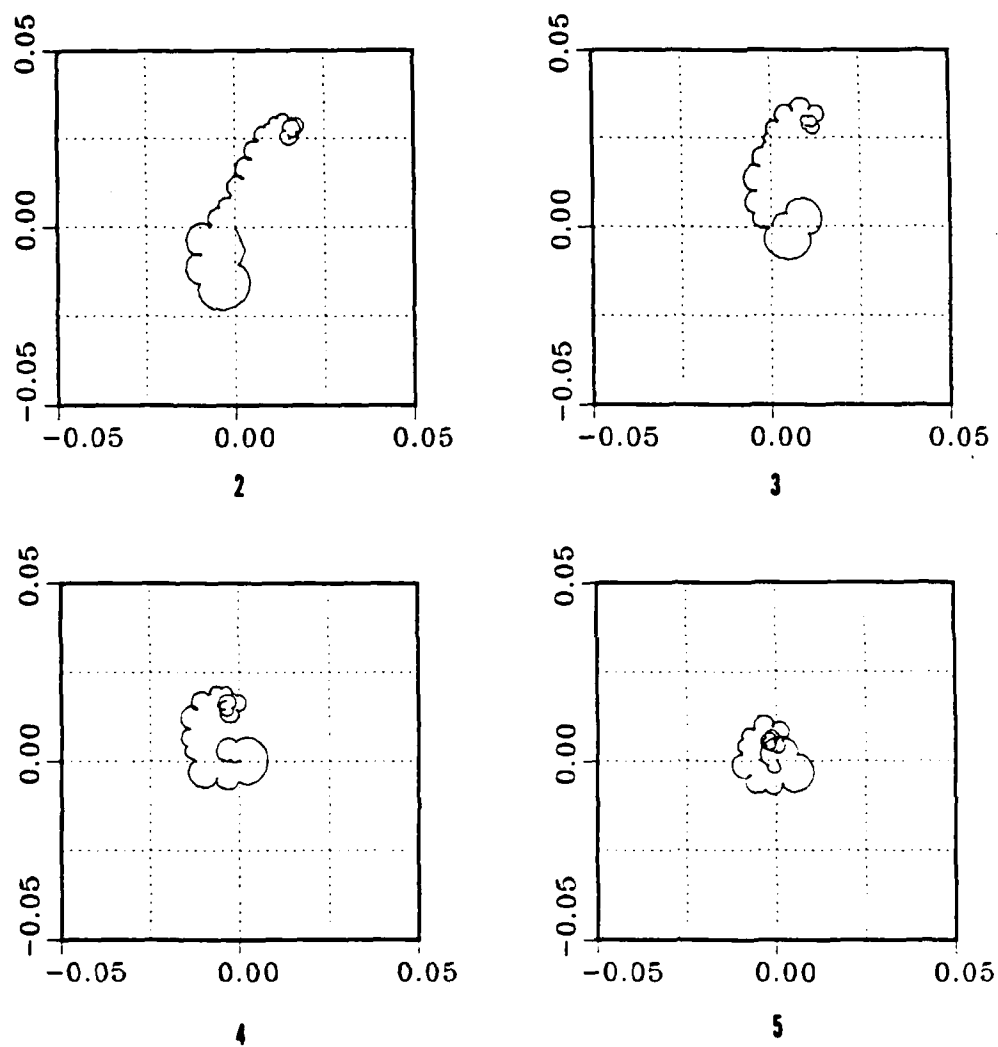


Figure 22. Mode-sum plots (20Hz) for points 2, 3, 4 and 5 in the shadow region.

(the end away from the origin) circle around tightly and do not contribute significantly to the final field value. This is a good indication that enough modes have been taken to get a good solution. Most of the other modes are adding in a reasonably orderly manner. Scanning from the upper left to the lower right (from the caustic into the shadow), we can see that the sum seems to be grouped into three or four segments and that the overall curve is folding up rather than either curling up or degenerating randomly. Thus, there are, in the shadow, several interfering components made up of partial sums of modes.

If we compute a ray equivalent angle based on the eigenvalue of the central mode in each group according to the equation

$$\cos \phi_n = \gamma_n/k, \quad (6.1)$$

where ϕ is the angle from the horizontal, we can determine something of the nature of these groups. In the upper left plot, there are three distinct groups: one that goes straight down from the origin, a second that goes up and slightly to the left, and a third that goes further up and to the right. The second and third groups meet at the real axis. The first of these groups has an imaginary equivalent angle. This indicates an evanescent component in the form of an inhomogeneous wave resulting from diffractive leakage out of the refractive turning point somewhat below the receiver altitude. Of course, no real ray equivalent exists for this component.

The second and third groups do have real equivalent ray angles and, thus, represent real propagating waves that result from the diffractive broadening of the ray paths forming the caustics below. A crude representation of a low-frequency ray would be a very broad, curved swath and, in this case, the paths have become wide enough to extend well into the classical shadow. In fact, at 20Hz, a typical value for the ray width parameter given by Equation (2.21) is 100m.

Consequently, the interference-like structure shown in the shadow spectra is, in fact, interference of several distinct field components both propagating and evanescent. The reduction in field level into the shadow is the result of a very orderly folding of the mode sum until, deep in the shadow, it has been broken into so many segments that it appears to be completely disordered.

6.2.3 Asymptotic analysis

Obviously, simple ray acoustics fails at a caustic; however, the single-term asymptotic correction given by Equation (2.27) allows calculation of a value for the field at and near the caustic. Unfortunately, at the frequency range of interest here, this ray theory correction gives very poor results.

Figure 23 shows the spectra of the field computed by the finite-difference method (solid line) at points 4 and 7 of the shadow zone series. The field predicted by the asymptotic correction to ray theory is also shown as a dashed line. The interference structure of the shadow zone field is, of course, absent in the asymptotic theory.

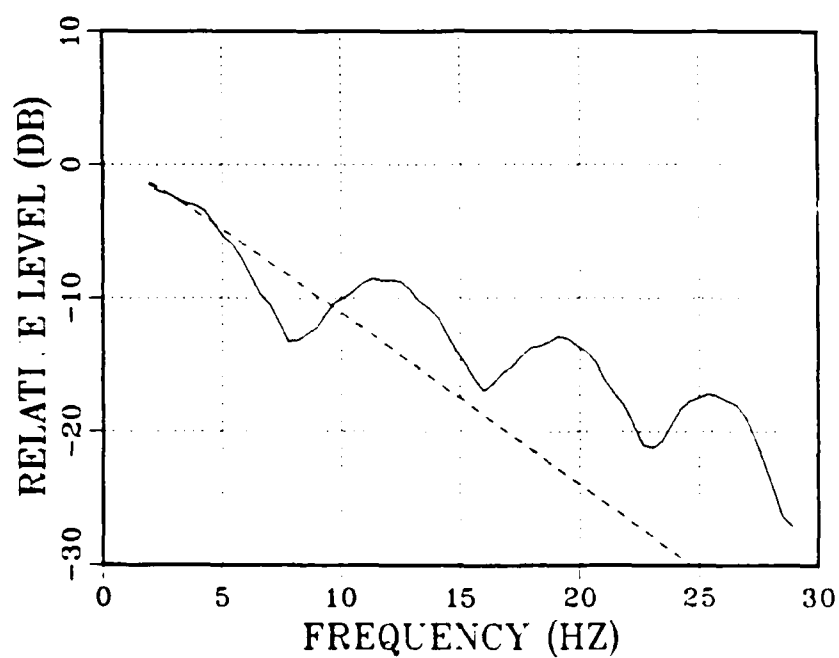
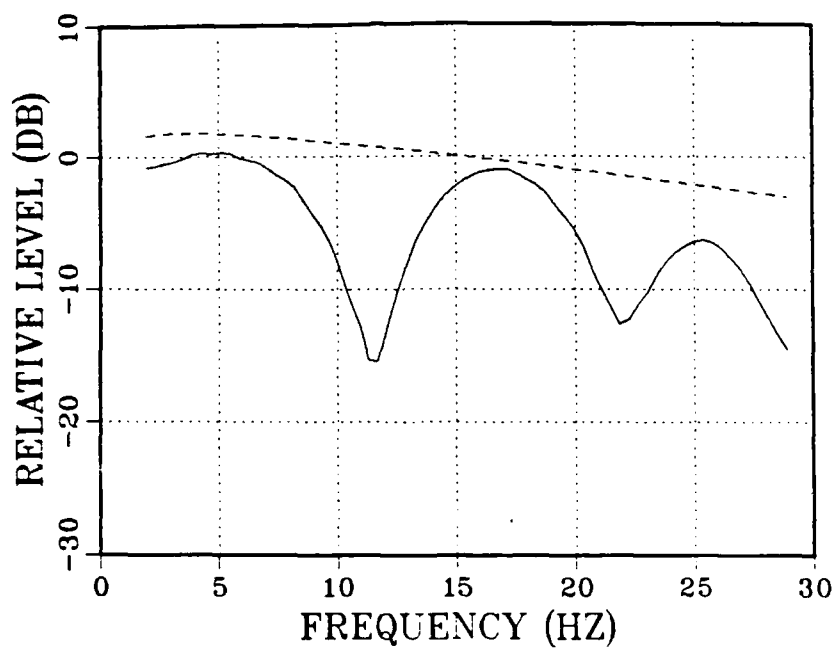


Figure 23. First-order asymptotic correction (----) compared to spectra from finite-difference model (—) at points 4 and 7 in the shadow region.

This first-order asymptotic correction was also computed for the points in the inter-caustic zone but the agreement was even poorer there so that the results are not shown. Typical values for the characteristic caustic width C_D of Equation (2.29) range from 50m to 150m at 20Hz (and 250m to 400m at 5Hz) so, clearly, the caustics are much too close together to be treated as distinct. Consequently, the first-order asymptotic correction is of little value. We will consider the second-order correction in the following section.

6.3 Structure of the Multiple Caustic

6.3.1 Mode-sum analysis

As in the shadow zone, we will again resort to the mode-sum plots to interpret the field structure. Since there is very little change in the spectrum or waveshape of the received pulses over the inter-caustic zone (and the cusp zone), the spectra and time series plots will not be shown. Figure 24 shows the mode-sum plots for four of the points in the inter-caustic region of Figure 15. The lower left plot is at the point of maximum field level in this zone.

One feature, identical (except for angular orientation) in all four of the plots, is that of the first two straight line segments from the origin. These two modes give the direct, low-angle path into this zone that is also shown on the ray plot. The other modes are associated predominantly with the higher angle converging rays.

The lower left plot at the field maximum shows that all of the modes form one group (beyond the direct path segment that happens to be in the same direction) working together to build up the field level. Instead

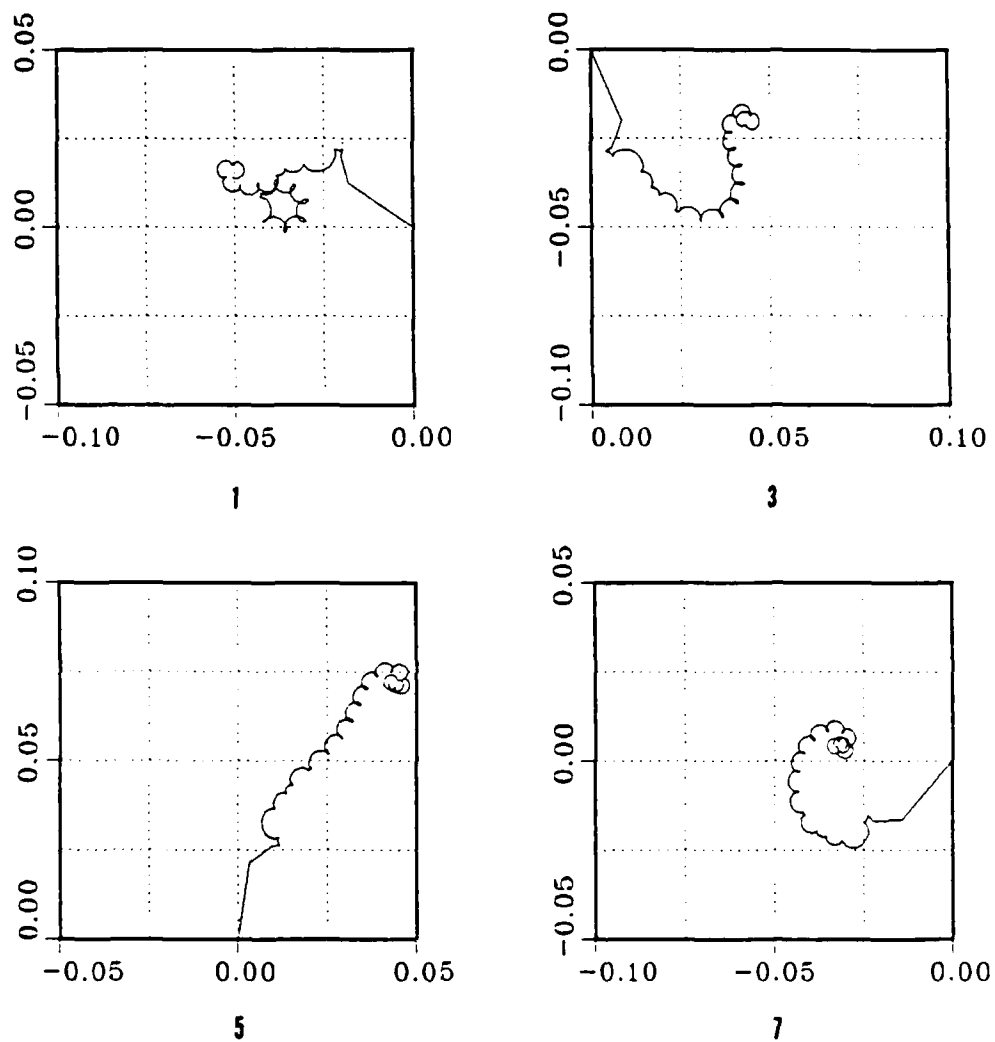


Figure 24. Mode-sum plots (20Hz) for points 1, 3, 5 and 7 in the inter-caustic zone.

of breaking up into a few discrete groups as the shadow zone modes did, this single mode group smoothly curls up on either side of the field maximum. There is no separable two-caustic structure at this frequency (20Hz). This is in accord with the overall field levels shown in Figure 19. Notice at point 1 (upper left plot of Figure 24) the mode sum has curled up to form a complete circle without showing any other distinct grouping.

Hence, the field in the inter-caustic zone actually only has one structural feature (aside from the trivial direct path) and this is representative of the general convergence and constructive interference in this area. There is no indication, even in the mode sum, that there are two caustics. Consequently, use of the extended \mathcal{A} theory to predict fluctuations in the inter-caustic zone probably has little meaning at these frequencies since it takes both caustics into account.

6.3.2 Asymptotic analysis

As we have seen, the two caustics bordering the inter-caustic zone cannot be treated as distinct elements. Instead, we can compute the field based on the second-order asymptotic correction to ray theory given in Equation (2.31). Figure 25 gives a contour plot of the field level (relative to free-field spreading) predicted by this second-order correction. To construct this figure, the weak reciprocal limb was ignored and the range Equation (2.30) was fit to the ascending and connecting limbs. These two limbs did, however, have quite different second derivatives at the caustics so a symmetric cubic curve is not a good representation. This asymmetry was reduced greatly by bisecting the

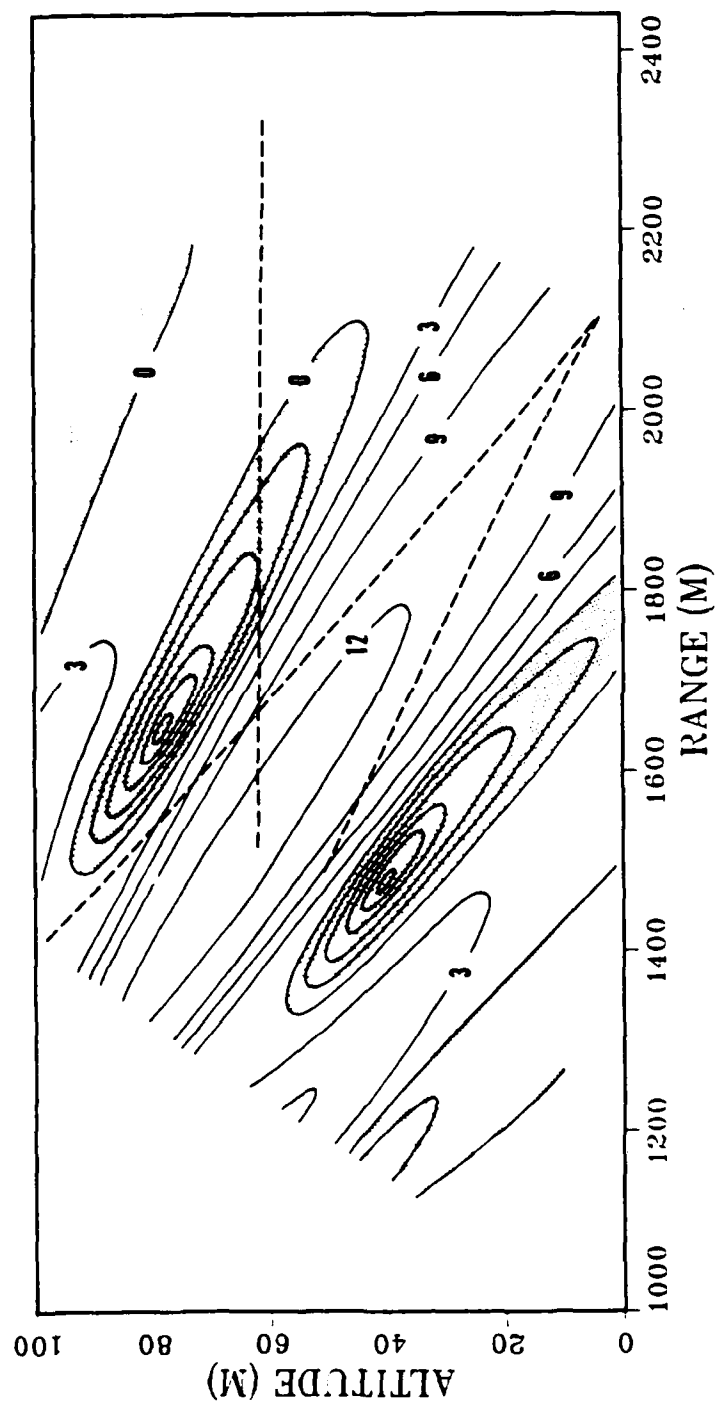


Figure 25. Prediction of field level at 20Hz by second-order asymptotic correction to ray theory. Compare to Figure 19.

wedge formed by these two caustics and the lower cusp, and taking a new "range" coordinate perpendicular to this bisector. In this way, the transformed range coordinate cuts both caustics at an angle approaching 90 degrees. The second derivatives of this transformed range became much more nearly equal. Once the coordinate transformation was done, X and Y could be computed by Equations (2.33) for a grid superimposed on the caustic system. Then the field was calculated from Equation (2.31) as discussed in Chapter II.

Although the frequency is still too low to allow detailed prediction of absolute field levels, the desired structure is clearly shown. There is a smooth ridge centered on the two caustics with depressions on either side. In addition, beyond these depressions, the field temporarily increases again thus showing the structure that is observed in the shadow by the mode and finite-difference methods. This structure is completely absent from the first-order asymptotic calculations.

As the frequency is increased, the major depressions would slide in toward the caustics and down toward the lower cusp. By scanning Figures 17, 18, and 19, we can see that this trend is correct but, again, the frequency is not high enough for the correspondence to be good in detail.

6.4 Structure near the Cusp

Because this cusp does not appear as a distinct feature on the overall field plot in Figure 19, we would not expect the structure to be very different from that in the inter-caustic zone.

The mode-sum plots for four points of the cusp series (see Figure 15) are shown in Figure 26. As in the inter-caustic zone, there are two distinct features: one mode representing the low-angle direct path and a large group of modes that represents the convergence. The direct path mode here generally opposes the other group but, otherwise, these plots are very similar to those in Figure 24.

We would expect that a frequency high enough to display the multiple caustic structure in the inter-caustic region would also resolve the cusp. By means of the X parameter of the second-order correction, we can determine what the lower frequency limit for resolution of the two caustics is. A value of -4 for X is required in order for the integral of Equation (2.31) to show two distinct ridges, one at each caustic. At 20Hz, X is about -2 at 50m altitude. Since the horizontal wave number is proportional to frequency, each derivative of range with respect to wave number gives an inverse proportionality to frequency. Thus, from the first of Equations (2.33), we can see that X is proportional to the square root of frequency. Consequently, the two caustics and the cusp should appear as distinct features at 80Hz (four times 20Hz) or greater.

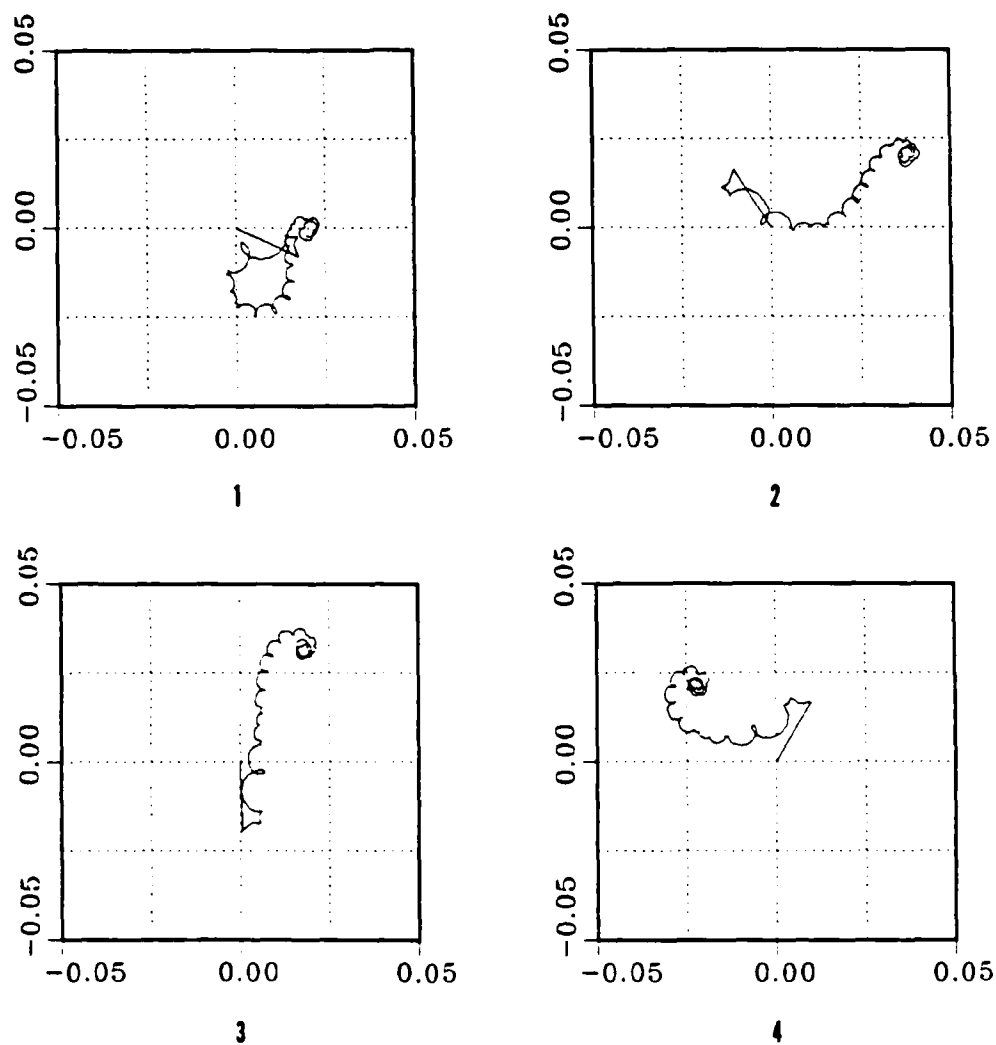


Figure 26. Mode-sum plots (20Hz) for points 1, 2, 3 and 4 in the cusp region.

Chapter VII

SIGNAL FLUCTUATIONS

Once time-varying perturbations in sound speed are introduced, the signal levels throughout the field fluctuate. These fluctuations are easy to simulate with the range-dependent finite-difference model, but this simulation, by itself, does not shed much light on the underlying causes of the fluctuations.

In Chapter III, we considered a ray interpretation of the fluctuation mechanism through the Δ and ϕ parameters. By following rays through a perturbed medium, three effects can be isolated: First, the ray path itself changes from the unperturbed path and there is a concomittant change in spreading loss. Second, an additional path may be possible, thereby introducing the potential for multipath interference. These two effects are considered simultaneously by the diffraction parameter Δ and, in cases where, under the influence of perturbations, the original path splits into two paths, neither of which resembles the original path, the Δ parameter can miss important contributions to the fluctuation. The third effect that is described by ray theory is the phase change resulting from differences in sound speed along the path. This effect is given by the strength parameter ϕ .

When the unperturbed field intensity can be adequately modeled by ray theory, these ray-based concepts of fluctuation have some utility. However, by probing a strongly diffractive region of focusing by wave meth-

ods in Chapter VI, we have seen that ray theory predictions can recreate the general features of the field only after a rather elaborate asymptotic correction. Since the fluctuation parameters Δ and ϕ are based on simple ray theory, there is no reason to expect that these parameters will be useful for estimating the type and magnitude of signal fluctuations in the present example.

In order to characterize fluctuations in wave terms then, we will consider the normal-mode decomposition of the field. This approach is still deficient in that, in the case we are considering, mode coupling is undoubtedly significant and we will ignore this coupling completely. In spite of this omission, some useful results can be developed. In this chapter, the fluctuation predictions of the finite-difference model will be briefly summarized and then a substantial effort will be devoted to the mode interpretation of these fluctuations.

7.1 Calculated Fluctuations

As described in Chapter V, the perturbations are introduced as a horizontally cyclic pattern of sound-speed variation that drifts through the field at 1.5m/s as a crude representation of the advection of large-scale turbulence. The pattern's period is 140m so the fluctuations should completely cycle about every 95s. As a compromise between the expense of running the finite-difference model and the desirability of frequent sampling, sixteen runs were made covering one complete cycle of fluctuation.

7.1.1 Time history of received levels

Figures 27 and 28 show the calculated level fluctuations at 2, 5, 10 and 20Hz for two of the points in the inter-caustic zone (points 1 and 5). Here, as before, the relative level scale indicates the gain over free-field spreading in a homogeneous medium. As we would expect, the higher frequencies show greater fluctuation and also greater departure from free-field spreading. Notice also that the 20Hz curve shows more variability at point 1 than at point 5, point 5 being at a point of greater field enhancement. This is a consistent feature of these simulations: in regions of strong focusing, the signal variability (at the higher frequencies) is generally lower than in other regions. This behavior is modeled in section 7.3.

The behavior of the signal level near the cusp as a function of time is not significantly different from the behavior in the inter-caustic zone but there are some notable differences in the shadow zone. The signal-level time histories for points 2 and 5 in the shadow region are shown in Figures 29 and 30, respectively. The progression in relative gain with frequency is not as smooth as in the inter-caustic zone but this can also be seen in the unperturbed spectra. As before, the higher frequencies have greater level changes and the greatest changes seen in the 20Hz curve in Figure 30 are accompanied by a marked asymmetry. This will be considered in more detail later but, for now, it is enough to say that this is an indication of alternately constructive and destructive interference between two nearly equal components.

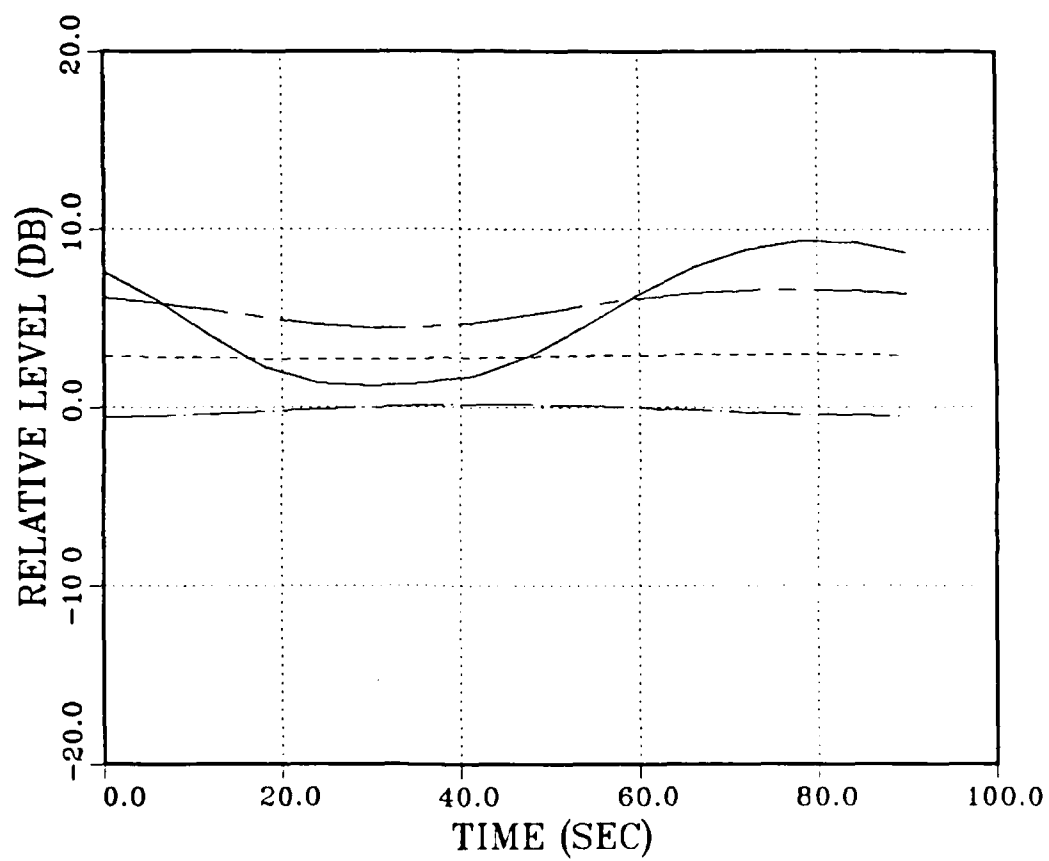


Figure 27. Signal level fluctuations at point 1 in the inter-caustic zone. Frequencies shown are 2 (— · —), 5 (-----), 10 (— — —), and 20Hz (————).

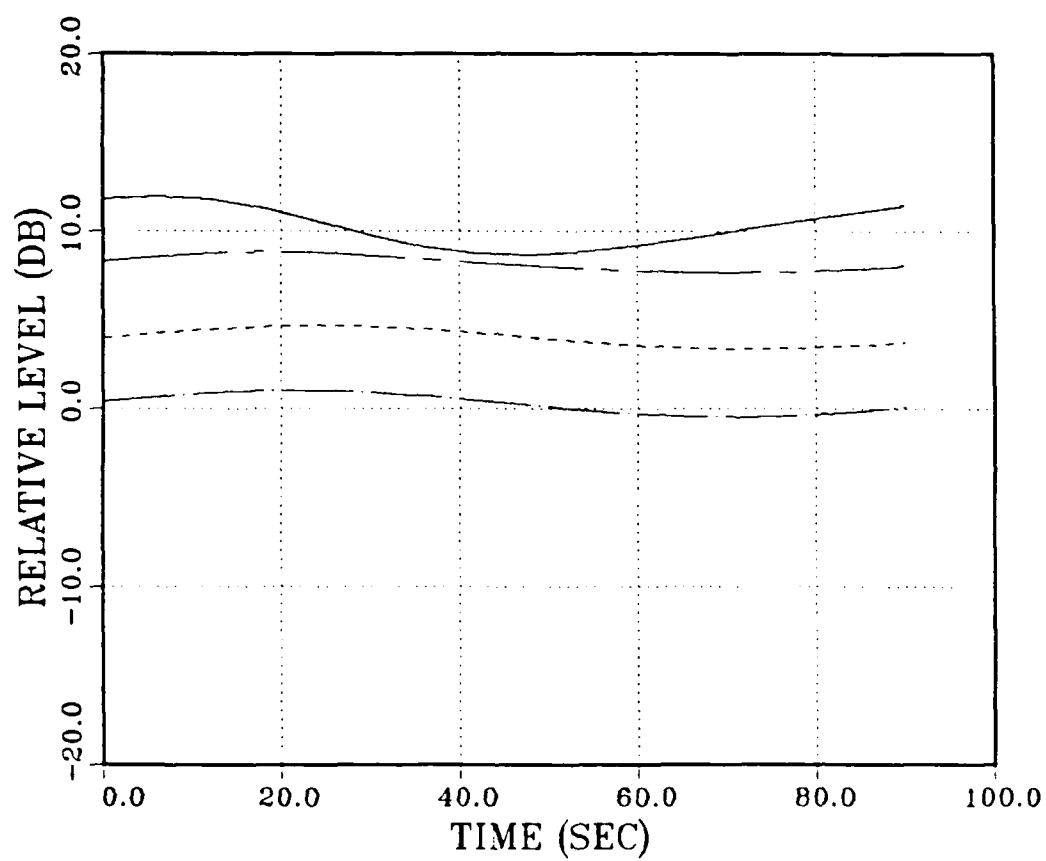


Figure 28. Signal level fluctuations at point 5 in the inter-caustic zone. Frequencies shown are 2 (— · —), 5 (----), 10 (— — —), and 20Hz (——).

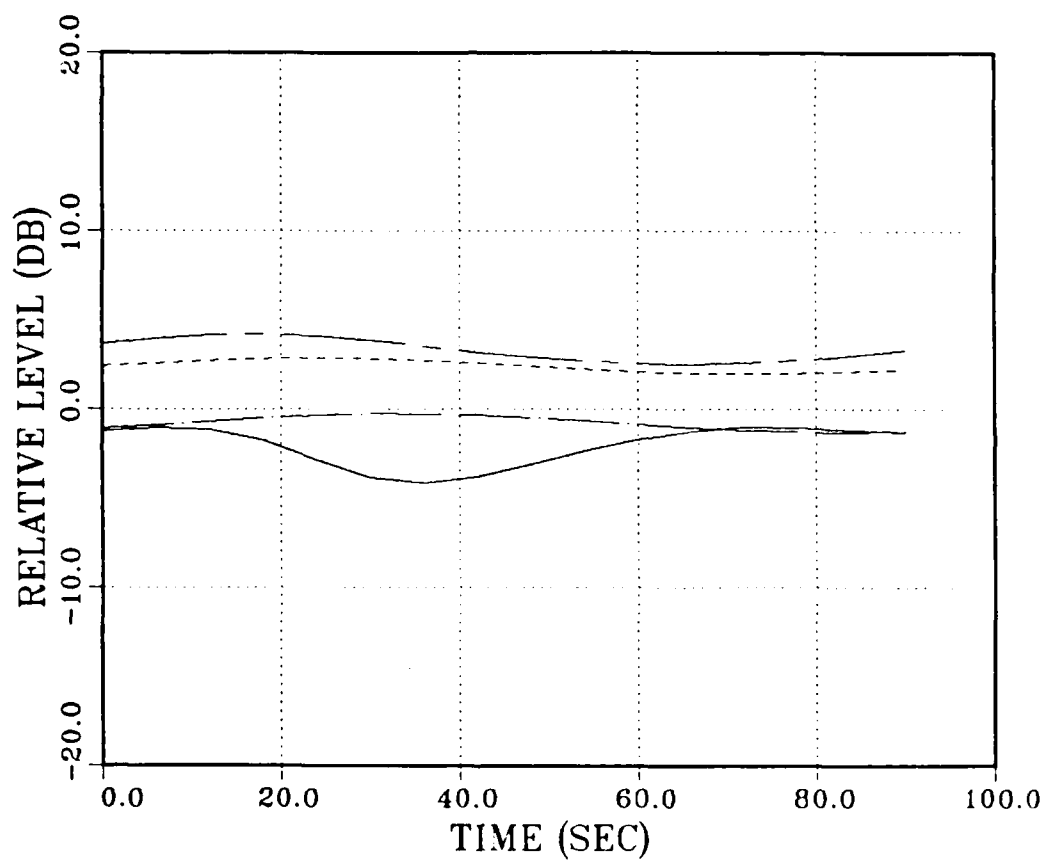


Figure 29. Signal level fluctuations at point 2 in the shadow region. Frequencies shown are 2 (— · —), 5 (---), 10 (— — —), and 20Hz (—).

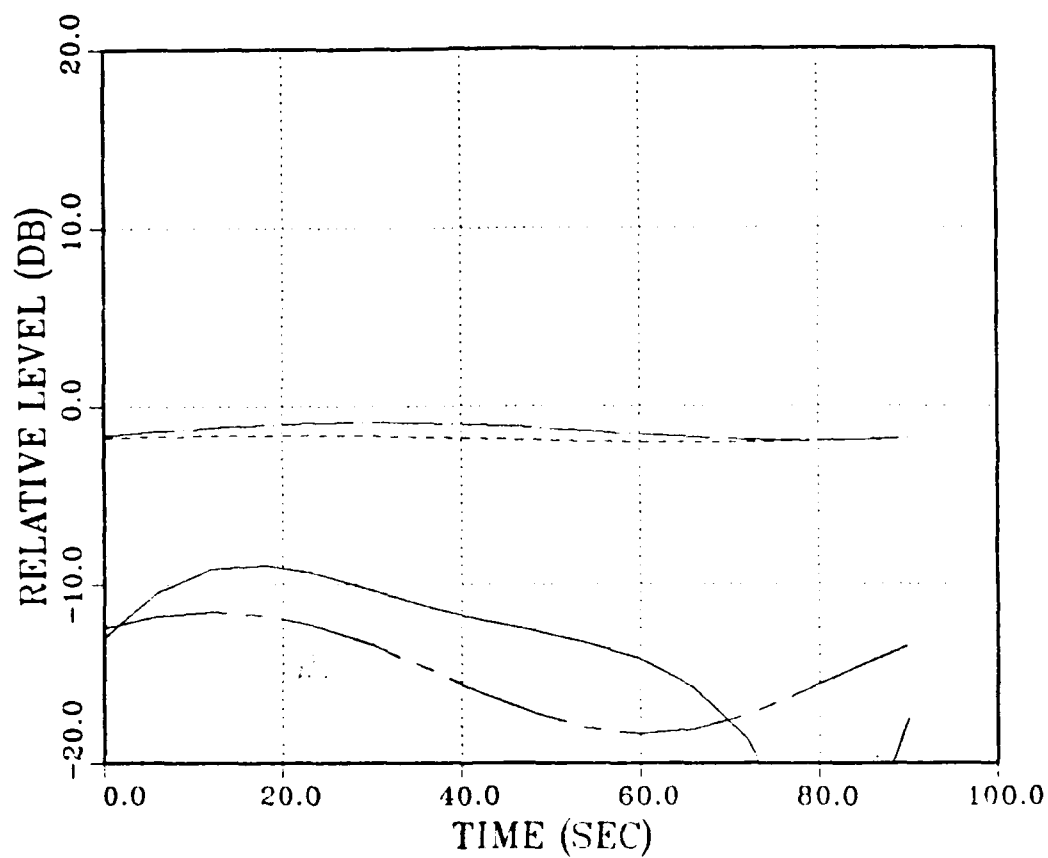


Figure 30. Signal level fluctuations at point 5 in the shadow region. Frequencies shown are 2 (— · —), 5 (---), 10 (— — —), and 20Hz (—).

7.1.2 Normalized fluctuation magnitude

In order to compare the fluctuations at different receiver locations and frequencies, the normalized fluctuation magnitude V given by Equation (3.12) will be used. This quantity is actually the standard deviation of the received amplitude divided by the average received amplitude. The fluctuation magnitude is a convenient quantity because it is a measure of signal variability that is independent of the mean signal level. Also, if the signal is determined by the interference of many components of random amplitude and phase, V approaches an upper limit of 0.52 (Skudrzyk, 1957). This is the saturation limit. (If, however, the signal results from interference of only two components, the limiting value of V can be somewhat less. This will be demonstrated in section 7.3.)

The values for fluctuation magnitude for receivers in all three of the observation areas and at 2, 5, 10 and 20Hz are shown in Figure 31. While the 20Hz values are consistently higher than all other values, there is no other definite trend with respect to frequency. None of the values exceed the saturation limit of 0.52 although the 20Hz curves approach this value. As we will see in the next section, the 20Hz component of the signal is just beyond saturation at the ranges considered here.

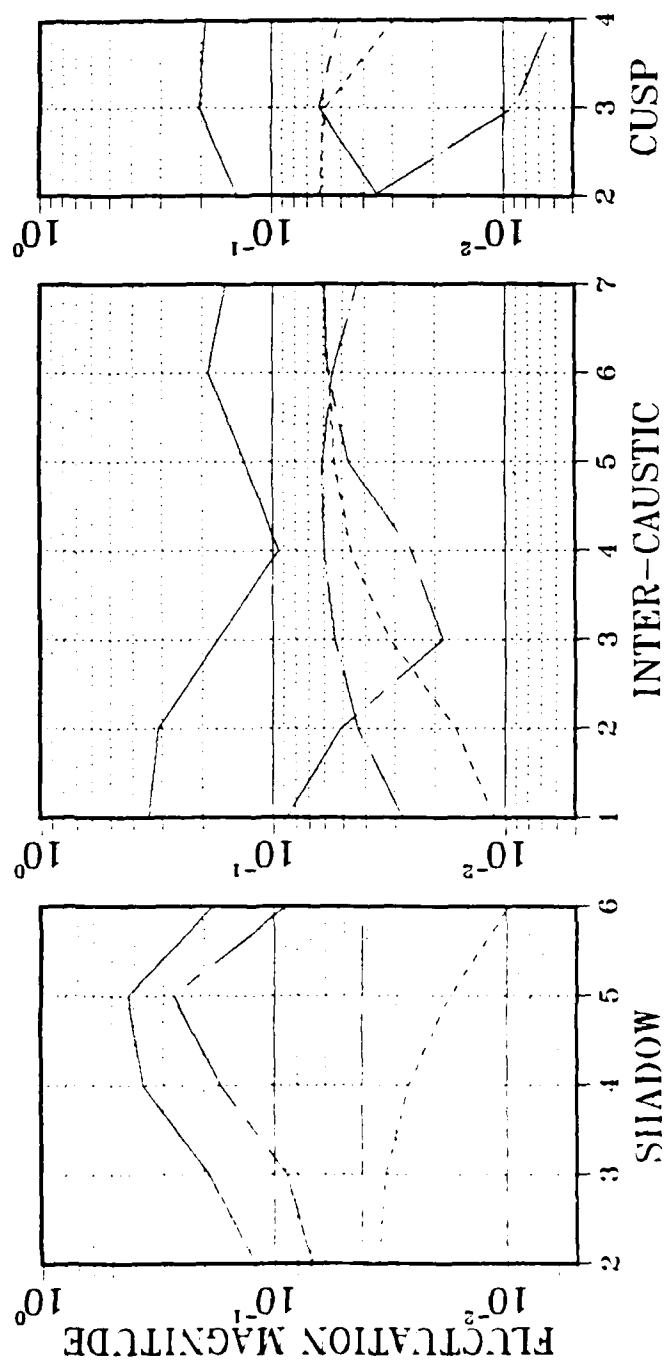


Figure 31. Fluctuation magnitude computed by the finite-difference method at 2 (—), 5 (---), 10 (- - - -), and 20 Hz (—).

7.2 Mode Analysis of Fluctuations

From Figure 31 it is clear that the normalized fluctuation magnitude does not follow a simple power law in range as is predicted by the homogeneous, isotropic scattering model. The field in this region is a complicated combination of coherent components and any attempt to analyze the nature of fluctuations must account for this structure. The analysis to follow is based on normal-mode theory and, in this context, the following points are important:

1. the degree of influence of the perturbations on a given mode;
2. the relative contribution of that mode to the received field (or, in other words, the degree to which that mode is excited);
3. the structure of the field at a particular receiver; and,
4. the influence of the range distribution of the perturbations.

The first three points can easily be described by mode theory but the fourth is more difficult unless the modes are allowed to couple, in which case the analysis becomes more time-consuming than the complete finite-difference simulation. This defeats the purpose of the modal analysis, which is to provide a simple model for the fluctuations without solving the complete field problem. Consequently, mode coupling will be neglected. In spite of this omission, a fairly good estimate of the fluctuation magnitude can be made and some of the important fluctuation mechanisms can be identified.

7.2.1 Equivalent fluctuation magnitude

By using the theory developed in section 3.2.3, we can estimate the eigenvalue shift introduced by some perturbation in sound speed. To do this, we must first fit the perturbation function given, in this case, by Equation (5.9) with functions that allow evaluation of the eigenvalue shift expression, Equation (3.29).

There is, of course, no point in resolving the perturbation profile in much finer detail than a wavelength at the highest frequency of interest. Surprisingly good results are obtained by fitting Equation (5.9) with only two segments: one segment linear in altitude above another constant segment. By means of Equation (3.34), these segments can be written as

$$\delta c/c^3 = 15 [1 - (z - 58)/42] / 338^3, \quad (7.1)$$

for z between 58m and 100m, and

$$\delta c/c^3 = 15/338^3, \quad (7.2)$$

for z between 0m and 58m. Otherwise, the sound-speed perturbation is zero.

By using these expressions in Equation (3.29), we can calculate the maximum positive and negative eigenvalue shifts. These shifted eigenvalues are then used in the exponent of the mode-sum Equation (2.8) to

compute the upper and lower limits for the fluctuation pressure amplitude. These two values and the unperturbed pressure amplitude are used to compute V by means of Equation (3.12). Since the amplitude fluctuations are usually roughly sinusoidal, this over-estimates V so the values are corrected by assuming that the extreme values of pressure amplitude are the upper and lower peaks of a sinusoidal curve.

The results of these calculations for 5 and 20Hz are shown in Figure 32. The solid lines reproduce the finite-difference calculations, while the dashed lines give the calculations by eigenvalue shift. The results at 2 and 10Hz are generally better in the shadow region and worse in the inter-caustic zone.

There are three obvious flaws in the eigenvalue shift calculation: First, there is no attempt to consider the actual range distribution of the perturbations. This does not seem to be a very serious problem since the correspondence between the eigenvalue shift calculation and the finite-difference calculation is quite good over the entire inter-caustic zone.

Second, because the shadow region has significant interference structure, the actual location of peaks and nulls can be sensitive to small changes in the profile or boundary conditions. Recall that the normal-mode model uses an extended sound-speed profile instead of explicit boundary conditions; hence, the structure in the shadow zone is reproduced accurately in form but not necessarily in precise position. As a result, a point for which the finite-difference model predicts an interference peak may, according to the normal-mode model, be near a null. This displacement in structural details can be seen by comparing the

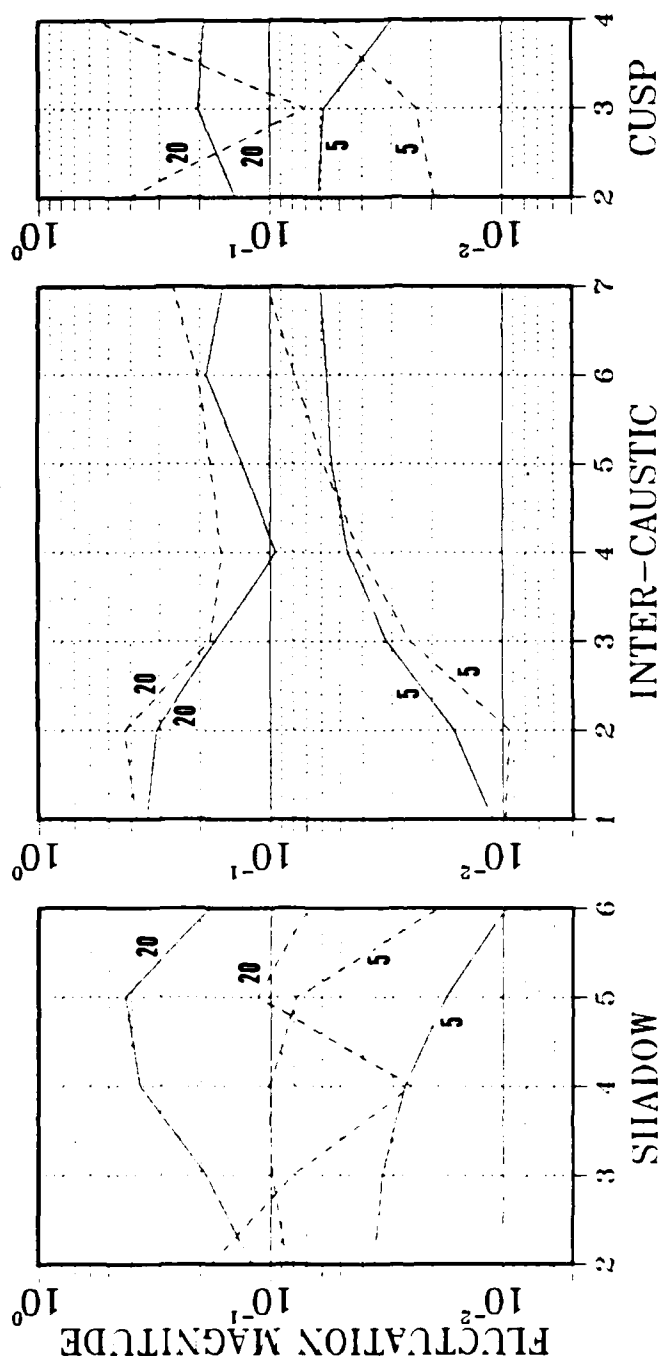


Figure 32. Comparison between fluctuation magnitudes at 5 and 20Hz as computed by the finite-difference model (—) and by eigenvalue shift (-----).

20Hz values of the finite-difference spectra in Figure 21 with the normal-mode field plot in Figure 19. This is far more likely to be a problem at the higher frequencies and we do see considerable disagreement in curve shape at 20Hz in Figure 32 for the shadow region points. The curve shape at 5Hz in the shadow region is reproduced accurately but with a shift in level. The cause for this is not clear but it probably is not related to the structure problem at 20Hz. The 2 and 10Hz curves (not shown) in the inter-caustic zone also reproduce the required shape accurately but with a significant level shift.

The final problem with the eigenvalue shift calculation results from the assumption that the maximum eigenvalue shift will produce the maximum level fluctuation. This is reasonable only below saturation. Above some frequency (or beyond some range), the mode-sum pattern will be disturbed so much that the magnitude of the sum will appear to vary randomly rather than continue to increase or decrease. As we will see shortly, the points considered here do show saturation at 20Hz and the eigenvalue shift calculations could be affected by being too low. The disagreement in the vicinity of the cusp is more likely a result of the proximity of the boundary since the boundary is modeled differently by each technique.

7.2.2 Modal analysis

We now have two methods for calculating the fluctuation magnitude but neither one gives much physical insight into the fluctuation process. For this, we must examine the components of the mode sum in the context of the first three points listed at the beginning of section 7.2, name-

ly: the perturbation-induced change in a given mode; that mode's relative contribution to the sum; and the overall field structure.

By computing the eigenvalue shift, we have already found the change in the individual modes. Before examining this more closely, consider another approach to finding the degree of influence of the perturbations on the modes: expand the perturbation function $\delta c/c^2$ as a sum of the unperturbed eigenfunctions. The series coefficient of any eigenfunction is then the relative excitation of that eigenfunction by the perturbation function. Since the eigenfunctions are orthogonal, the coefficients for the series expansion are easily computed and the result, to a constant factor, is identical to Equation (3.29), the equation for the eigenvalue shift. (We have also used Equation (3.34), valid for small perturbations.) Therefore, the series coefficients are simply the eigenvalue shifts.

Now, the difference between the eigenvalues before and after perturbation does not directly indicate the change in the appropriate term of the mode sum. Since we are considering only the phase changes in the mode sum to be important, we would like to know the difference between the old phase and the perturbed phase. This depends not only on the eigenvalue shift but also on the horizontal range. Furthermore, this phase difference can be greater than a full cycle but we are only interested in the net change in the complex term in the mode sum. Consequently, let us define a perturbation weight H such that

$$H = \left| \sin [(\gamma_{np} - \gamma_n)x/2] \right| . \quad (7.3)$$

When H is zero, the eigenvalue shift is such that there is no net change in the mode phase; when H is unity, the phase has shifted by 180 degrees. In other words, the larger H is for a given mode, the more that mode is changed by the perturbations.

A sample calculation of this perturbation weight is shown in Figure 33 for points 1 and 5 in the inter-caustic zone at 5Hz. The results for a similar calculation at 20Hz are shown in Figure 34. For the particular shape of perturbation function used in this study, the lowest mode is always the most affected mode, although the phase change may be greater than 180 degrees, in which case the perturbation weight drops below unity. This is the case for the solid curve in Figure 34. If the frequency is high enough (or the range large enough), the behavior of H for the lower modes can appear to be quite erratic since the total phase difference can be several complete cycles. This is illustrated by Figure 35 in which the calculation of the previous figures is repeated at 50Hz. Here, the first six modes show large phase changes over the range interval from point 1 to point 5.

By scanning Figures 33 through 35, we can see two distinct kinds of perturbation weight changes with range. The first kind of change is seen in the low-order modes, which show the most change with perturbation at any given range and also show the most change as a function of range. (This range dependence is only clear at the higher frequencies.) The second kind of change is the relatively small but consistent change between points 1 and 5 (i.e., between the solid and the dashed curves) for the modes beyond the low-order group. This change increases with frequency and slowly decreases with mode number. Since the phase change

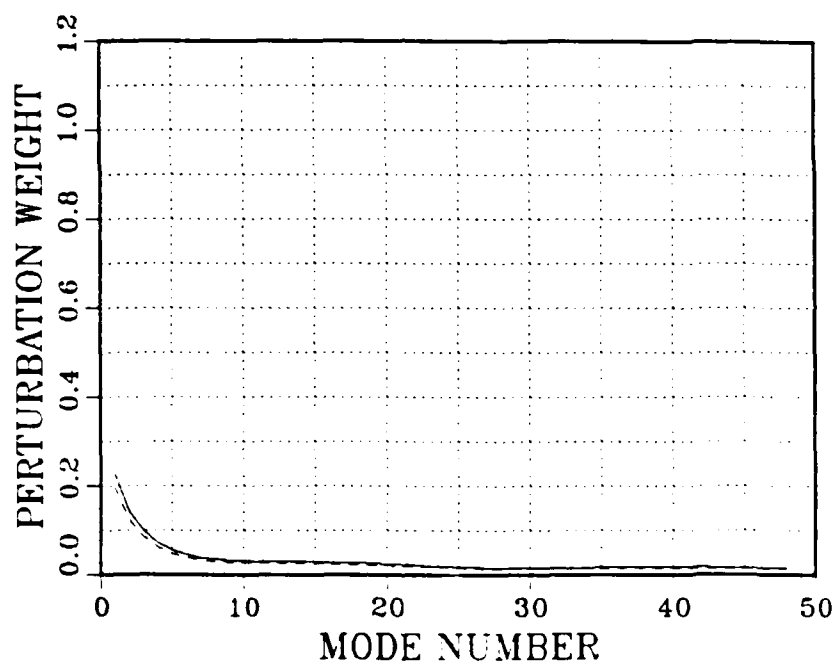


Figure 33. Perturbation weight function for the normal-mode solutions at points 1 (---) and 5 (—) in the inter-caustic zone (5Hz).

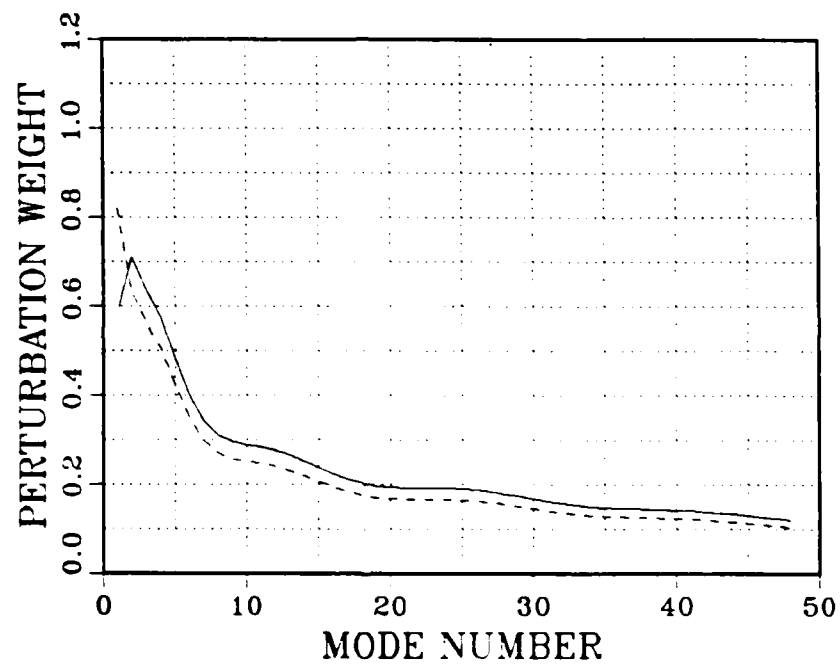


Figure 34. Perturbation weight function for the normal-mode solutions at points 1 (----) and 5 (—) in the inter-caustic zone (20Hz).

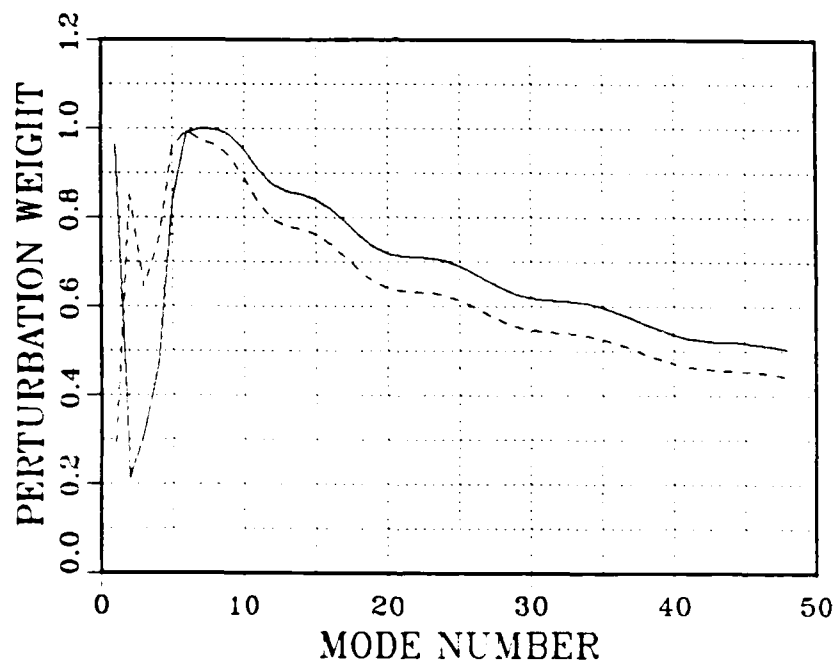


Figure 35. Perturbation weight function for the normal-mode solutions at points 1 (---) and 5 (—) in the inter-caustic zone (50Hz).

is relatively constant with mode number, the part of the mode sum corresponding to higher order modes retains its shape and rotates as a whole by that small phase change.

At the lower frequencies, the perturbations affect only the low-order modes to any significant degree. If these modes are important to the sum (we will see later how to determine this), then the fluctuations may be large. At the higher frequencies, the perturbation effects on the low-order modes increase until saturation is reached. The onset of saturation is indicated when the phase shift of the most-affected mode goes beyond 180 degrees. From Figure 34 and 35, we can see that the fluctuations are just saturated at 20Hz and well into the saturation region at 50Hz.

Now that we have seen how the perturbations affect individual modes, we will consider how the individual mode changes influence the total field through the mode sum. Not all modes contribute equally to the field; their contribution depends on how strongly they are excited and this, in turn, depends on the location of the source and receiver with respect to the nodes or antinodes of the mode eigenfunctions. If we call the amplitude of any one mode in the mode sum given by Equation (2.8) its excitation and plot this excitation as a function of mode number, we obtain a curve like that in Figure 36. Since, for uncoupled modes, the excitation is not a function of range, only of source and receiver altitude, this one curve applies to all of the inter-caustic zone points at 5Hz. The same calculation at 20Hz is shown in Figure 37. We can see that, at both frequencies, the perturbation changes of the low-order modes will be important since the low-order modes are the most strongly excited.

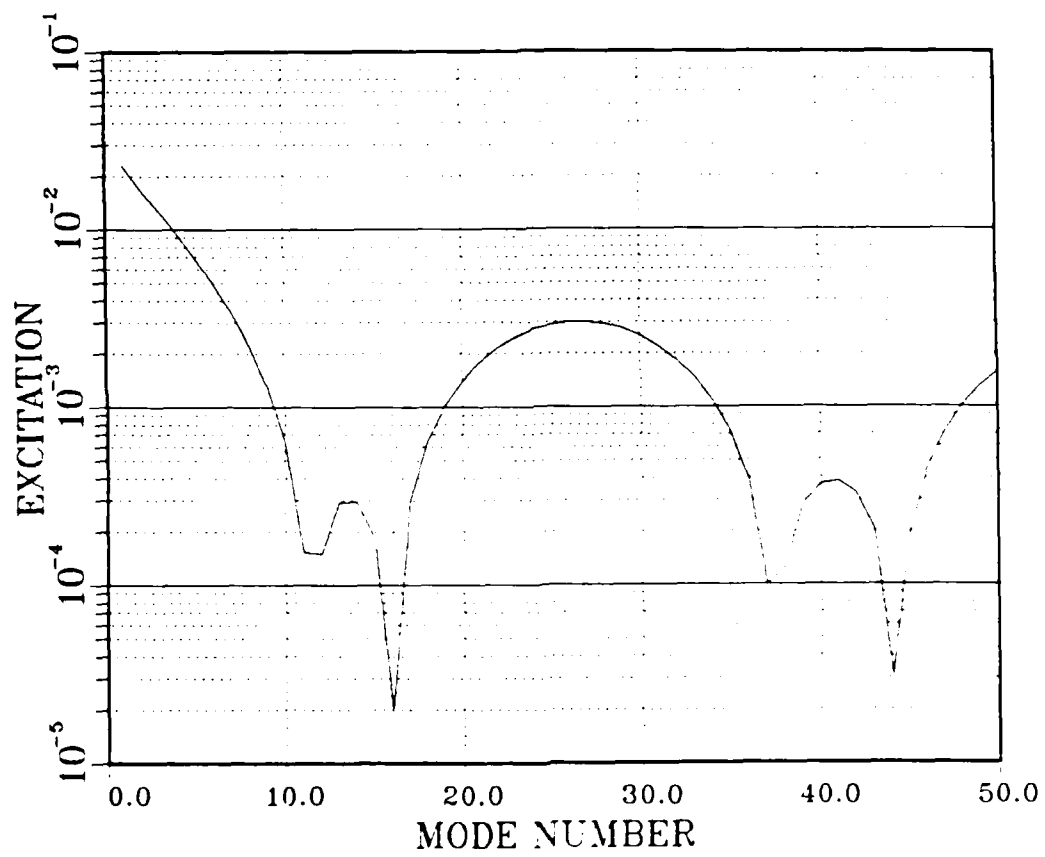


Figure 36. Relative excitation of 5Hz modes for receiver at the altitude of the inter-caustic region points.

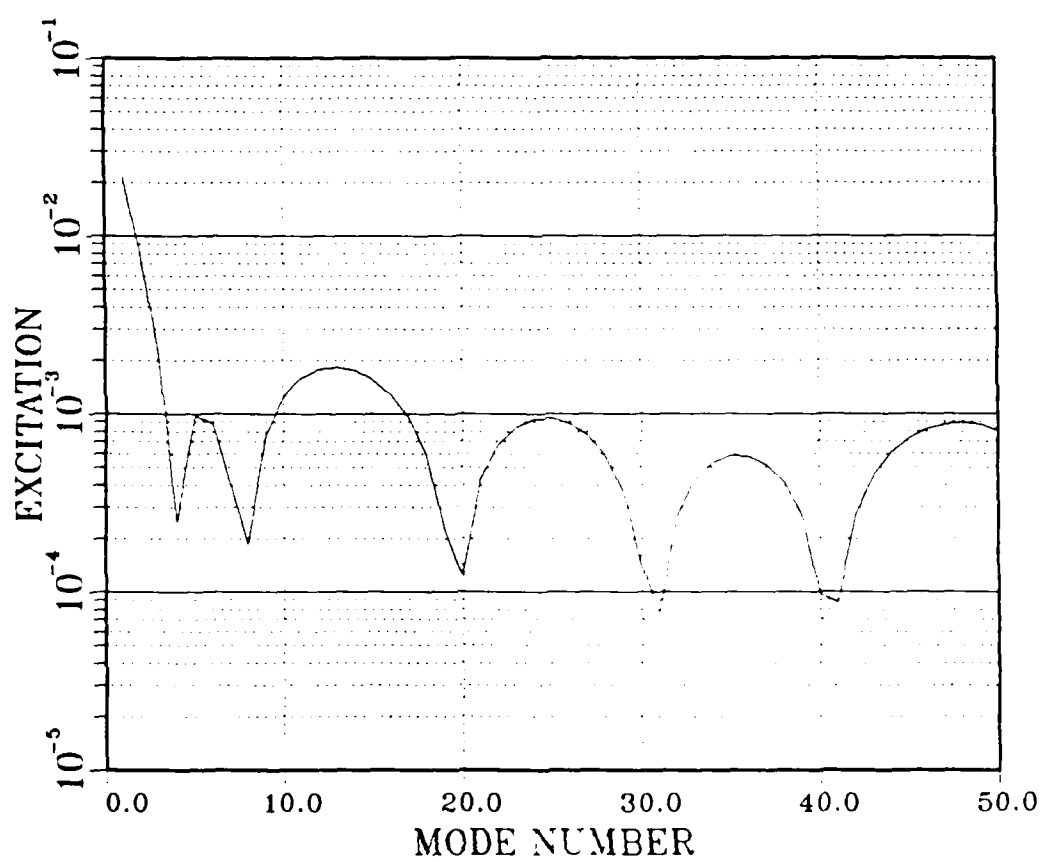


Figure 37. Relative excitation of 20Hz modes for receiver at the altitude of the inter-caustic region points.

The results in the shadow region are somewhat different. Figure 38 shows that the first few modes for a point near the focus (point 2) are strongly excited while deeper in the shadow (at point 5), the higher modes are stronger. This feature is consistent at all frequencies and, therefore, allows us to determine how much of an influence changes in the low-order modes have on the fluctuation magnitude. Referring back to Figure 32, we can see that, at 5Hz in the shadow region (and, also, for the 10Hz curve not shown), the trend is toward lower fluctuation magnitude deeper in the shadow. Hence, here, the varying excitation of the low-order modes is controlling the fluctuation magnitude. At 20Hz, there is no similar trend.

Finally, the degree of signal fluctuation also depends on the structure of the field. As demonstrated by the mode-sum curves in Chapter VI, the structure in the shadow region is substantially different from that in the inter-caustic zone. In between the caustics, where the field is strong, the modes add in a very orderly manner (for example, see Figure 24, the lower left plot). Here, we would expect the fluctuations to be more predictable and, in fact, the agreement between the finite-difference calculation of V and the eigenvalue shift calculation is quite good in this region.

7.3 Two-component Model

Particularly in the region of strong enhancement between the caustics, we have been able to successfully predict the fluctuation magnitude by computing the eigenvalue shift introduced by sound-speed perturbations and then summing the phase-shifted modes. While this method

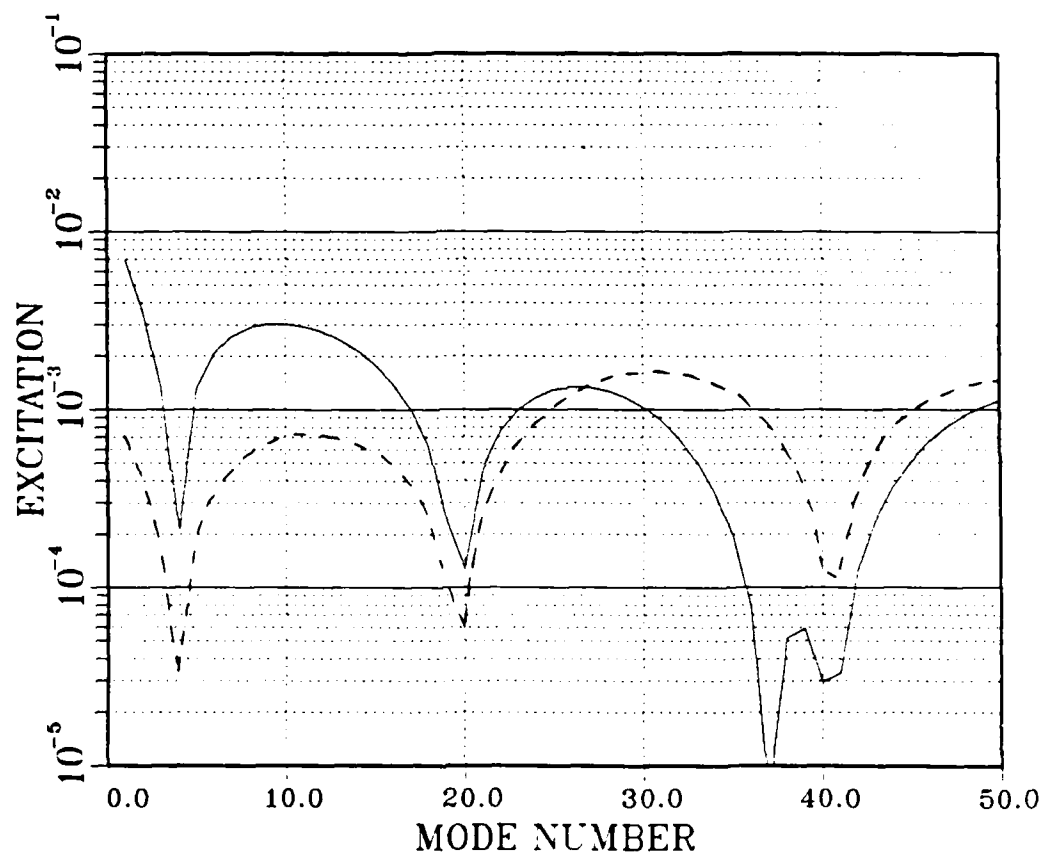


Figure 38. Relative excitation of 20Hz modes for receivers at points 2 (—) and 5 (----) in the shadow region.

avoids solving the range-dependent problem directly, its principal value rests in the insight gained into the fluctuation process. In this section, we will construct a very simple fluctuation model based on just one of the properties observed in the eigenvalue-shift work.

In Chapter V, we saw that the field structure in the shadow region comprised two or three dominant components, which produced a rather simple interference pattern. Furthermore, the fluctuating signal level at one of the points in the shadow (see Figure 30, 20Hz curve) appeared to be the result of two nearly equal components with variable relative phase. Finally, the eigenvalue shift always affected a few of the lowest order modes significantly more than the other modes (see Figures 33 and 34). These observations suggest that a model consisting of the vector sum of two, unequal amplitude components may be able to describe the signal level fluctuations if the relative phase of these components is varied according to the eigenvalue shift calculations.

We have, then, a sum of two vectors of magnitude P_0 and σP_0 with relative phase ϕ . The resultant magnitude is

$$P = P_0 \sqrt{1 + \sigma^2 + 2\sigma \cos \phi}, \quad (7.4)$$

and the average resultant for ϕ varying over some range from ϕ_1 to ϕ_2 is

$$\bar{P} = \left| (\phi_2 - \phi_1)^{-1} \int_{\phi_1}^{\phi_2} P d\phi \right|, \quad (7.5)$$

or

$$\bar{P} = P_0 \left| 2(1 + \sigma) \left[E(\phi_2/2, r) - E(\phi_1/2, r) \right] / (\phi_2 - \phi_1) \right|, \quad (7.6)$$

where E is the incomplete elliptic integral of the second kind and

$$r = 2\sqrt{\sigma} / (1 + \sigma). \quad (7.7)$$

The resulting fluctuation magnitude can be computed by integrating to find the mean-square amplitude difference (see Equation (3.12))

$$V^2 = -1 + \left[1 + \sigma^2 + 2\sigma(\sin \phi_2 - \sin \phi_1) / (\phi_2 - \phi_1) \right] (P_0 / \bar{P})^2. \quad (7.8)$$

7.3.1 Predictions at saturation

The maximum fluctuation range results when ϕ varies from $-\pi$ to $+\pi$ (or more, of course); this is the saturation limit for this model. Because of symmetry, we can calculate the saturation limit by setting ϕ_1 equal to zero and ϕ_2 equal to π . Abramowitz and Stegun (1965) give a convenient polynomial approximation for $E(\pi/2, r)$ so that P may be cal-

culated easily. If the two components are equal (that is, $\sigma = 1$), then the fluctuation magnitude V is equal to 0.48. This is an absolute limit on V for this simple model and it agrees quite well with the usual saturation limit of 0.52 (Skudrzyk, 1957). Figure 39 gives the relationship between V and σ . As we can see, if the two dominant field components are unequal in amplitude, the fluctuation magnitude can be well below 0.52 even at saturation.

As a check of the validity of the two-component model, let us take the minimum and maximum amplitudes of the fluctuation time history curves for 20Hz and compute the fluctuation magnitude using Equation (7.8). If we take, in particular, the curves corresponding to points 2 and 5 in the shadow region (Figures 29 and 30), we find that the minimum and maximum levels at point 2 are -4.1dB and -1.0dB respectively while those at point 5 are -25.9dB and -8.9dB. Consequently, σ is 0.18 for point 2 and 0.75 for point 5. The corresponding fluctuation magnitudes computed by Equation (7.8) are then 0.12 and 0.43, respectively. These values are essentially identical to those computed by the finite-difference model and shown in Figure 32. While this demonstrates the consistency of the two-component method, the fluctuation time history minima and maxima are not easy to calculate and this is not a practical way to compute V .

To apply the two-component model to the problem considered here, a practical rule for selecting the two components must be established. The primary indicator for separating the two components is the relative shift in eigenvalue of the modes as given by the perturbation weight function. (See, for example, Figure 34.) For the particular perturba-

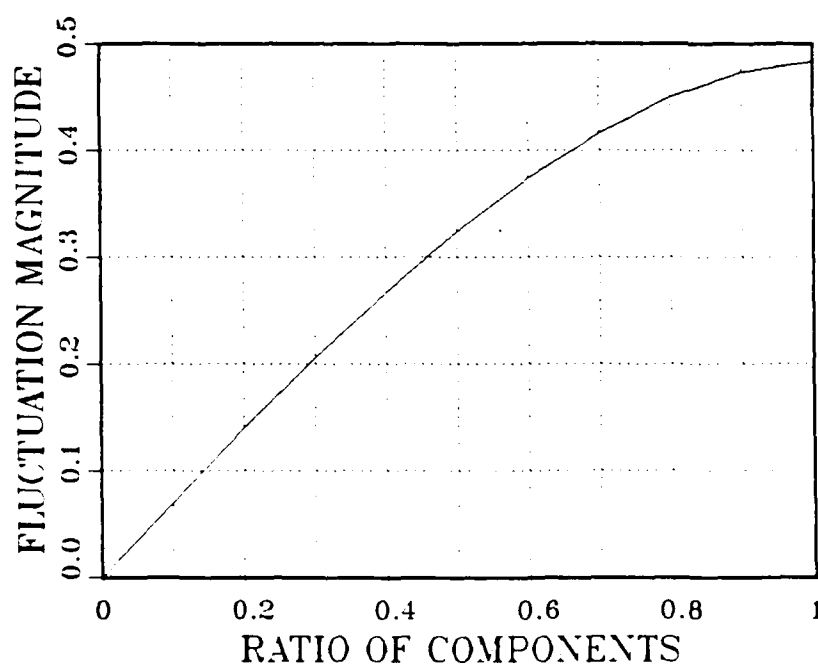


Figure 39. Prediction of fluctuation magnitude at saturation by two-component model.

tion function used in this analysis, the shift is always greatest for the low-order modes. The eigenvalues of the modes near this peak in the perturbation weight curve have approximately the same shift; these shifts are correlated with respect to the perturbations. This can be seen in a qualitative way by examining the three lowest modes in Figure 24. Although they rotate in the plane from diagram to diagram, they rotate as a group with no significant shift relative to one another.

At both 5 and 20Hz, the first component would consist of several of the lowest modes; however, not all of these modes are significant. The mode amplitude or excitation curve (see Figure 37) drops rapidly beyond the first mode so only a few modes will contribute to the first component. If the perturbation weight curve and the mode excitation curve are multiplied together, the mode number for which this composite curve drops to $1/e$ times the value at the first mode can be used as a dividing point between the two components. At 5Hz, there are two modes below this limit while, at 20Hz, there is only one.

At 20Hz, we will identify the lowest mode as one component and the sum of the rest of the modes as the second component. From the ratio of the magnitudes, we can compute σ and, therefore, V since, at 20Hz, the fluctuations have saturated. The results are shown in Figure 40: the dashed lines give the fluctuation magnitude calculated by eigenvalue shift and the circles give those values calculated by the two-component model. Considering the coarse nature of the two-component model, the agreement is good. Notice that we only had to compute the eigenvalue shift for the first several modes to determine whether or not saturation was taking place. Hence, the two-component calculation is easy to perform.

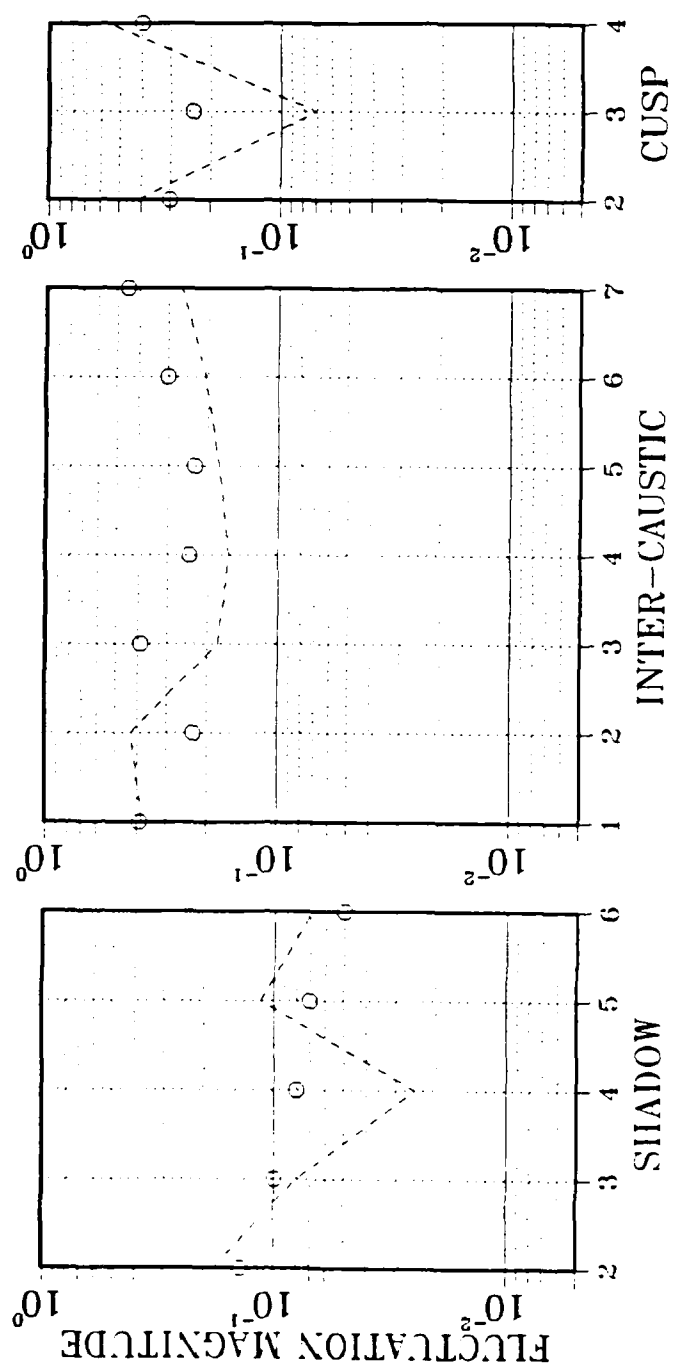


Figure 40. Fluctuation magnitude calculations by the two-component model (circles) and by the complete eigenvalue-shifted mode sum (dashed lines) at 20Hz.

7.3.2 Predictions below saturation

At 5Hz, we will take the sum of the lowest two modes for the first component. (The following calculations are not very sensitive to the number of modes selected for the first component; this is a good feature of this model.) Since the fluctuations are not saturated at 5Hz, we also need the unperturbed relative phase between the components and an estimate of the phase change with perturbation. To compute this latter quantity, we can take the perturbation weight from Figure 33 and convert it to phase change by Equation (7.3). We can compute the unperturbed relative phase from the magnitude and phase of the sum of the first two modes and the magnitude and phase of the entire mode sum from the normal-mode solution. The elliptic integrals in Equation (7.6) have no convergence problems, so they can be calculated by simple numerical integration. Figure 41 gives the results of this calculation (circles) as compared to the eigenvalue shift results (dashed lines). As at 20Hz, the agreement is good.

From these results, it is clear that the two-component model is of some value in predicting the fluctuation magnitude for focused, strongly diffractive fields with range-dependent perturbations. Using the perturbation weight calculations (basically an expansion of the altitude variation of the perturbations as a series of the mode eigenfunctions), we can find the expected phase change between components and from an unperturbed normal-mode solution, we can compute the relative magnitudes and starting phases of the two components.

While this procedure is simple, it is essentially restricted to fluctuations below saturation or just at saturation. For strongly saturated

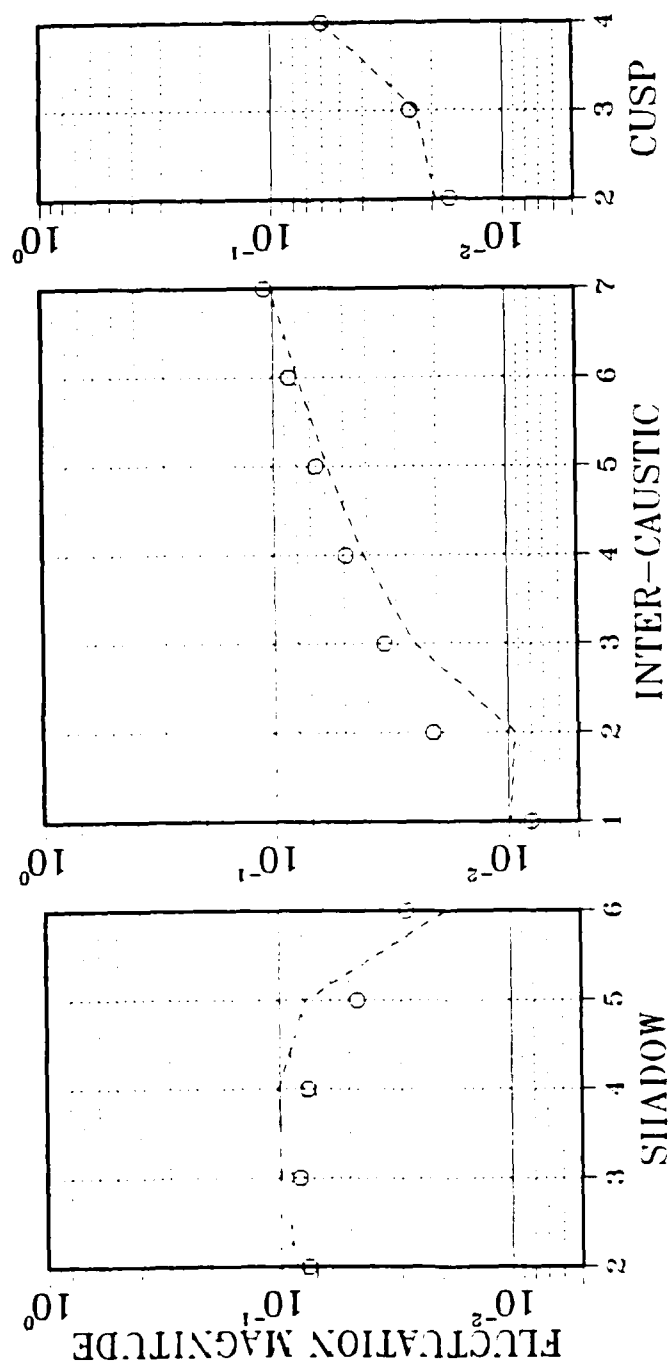


Figure 41. Fluctuation magnitude calculations by the two-component model (circles) and by the complete eigenvalue-shifted mode sum (dashed lines) at 5Hz.

fields, there will be more than two significant field components. A multi-component model could, of course, be constructed, but the complications introduced would limit its utility. Also, remember that the range-dependence of the perturbations is only included in a very crude manner; this weakness probably accounts for much of the discrepancy between the finite-difference results and the eigenvalue shift results in Figure 32.

7.4 Correspondence to Fluctuation Parameters

Before leaving the analysis of signal fluctuations, let us briefly consider the implications of the \mathcal{A} - \mathcal{F} parameters. As we have discussed, these parameters may not be useful for describing the fluctuations in detail because the parameters are based on simple ray theory and, at the frequencies of interest here, wave effects predominate. We can, at least, compare these parameters to the characteristics of the fluctuations predicted by the wave theory models.

For the model of the planetary boundary layer used here, a simple approximate form for \mathcal{F} will suffice. The perturbation component μ is given by Equations (5.5), (5.8) and (3.15) as

$$\mu(x, z, t) = u(z) \cos[\pi(x + v_a t)/\hat{z}] \quad . \quad (7.9)$$

Since the frequencies of interest correspond to long wavelength propagation that will sample a very broad swath rather than a narrow ray, we can approximate the ray path as a horizontal line and use vertically averaged properties. In this way, Equation (3.14) reduces to

$$\Phi = 2 \hat{z} f u(z_0)/c \quad . \quad (7.10)$$

If we use an average of 1m/s for $u(z_0)$ (based on a peak value of 3m/s), 70m for \hat{z} and 350m/s for c , then

$$\Phi = 0.4 f \quad . \quad (7.11)$$

The calculation of \mathcal{A} is based on Equation (3.16) and the caustic extension, Equation (3.19). As such, these \mathcal{A} values differ considerably from values calculated from the usual \mathcal{A} definition. Figure 42 shows the difference between these two methods of \mathcal{A} calculation. In each case, the parameters are calculated in range from one caustic to the other (through the inter-caustic zone) and at three different frequencies. At 1 Hz the results are radically different. The standard calculation shows peaks at the caustics (at all frequencies, in fact) whereas the extended calculation peaks near the middle. At 50Hz the left caustic is treated differently while the results are similar on the right (the stronger caustic). Finally, at 1kHz, the comparison is quite good. Of course, as the frequency increases, ray theory becomes more accurate.

In Figure 43, the range of $\mathcal{A}-\Phi$ parameters encountered in this investigation of the zone between two caustics is shown. Based on the assumption that ray acoustics is valid for the unperturbed medium, the various regions of $\mathcal{A}-\Phi$ space represent different types of induced sig-

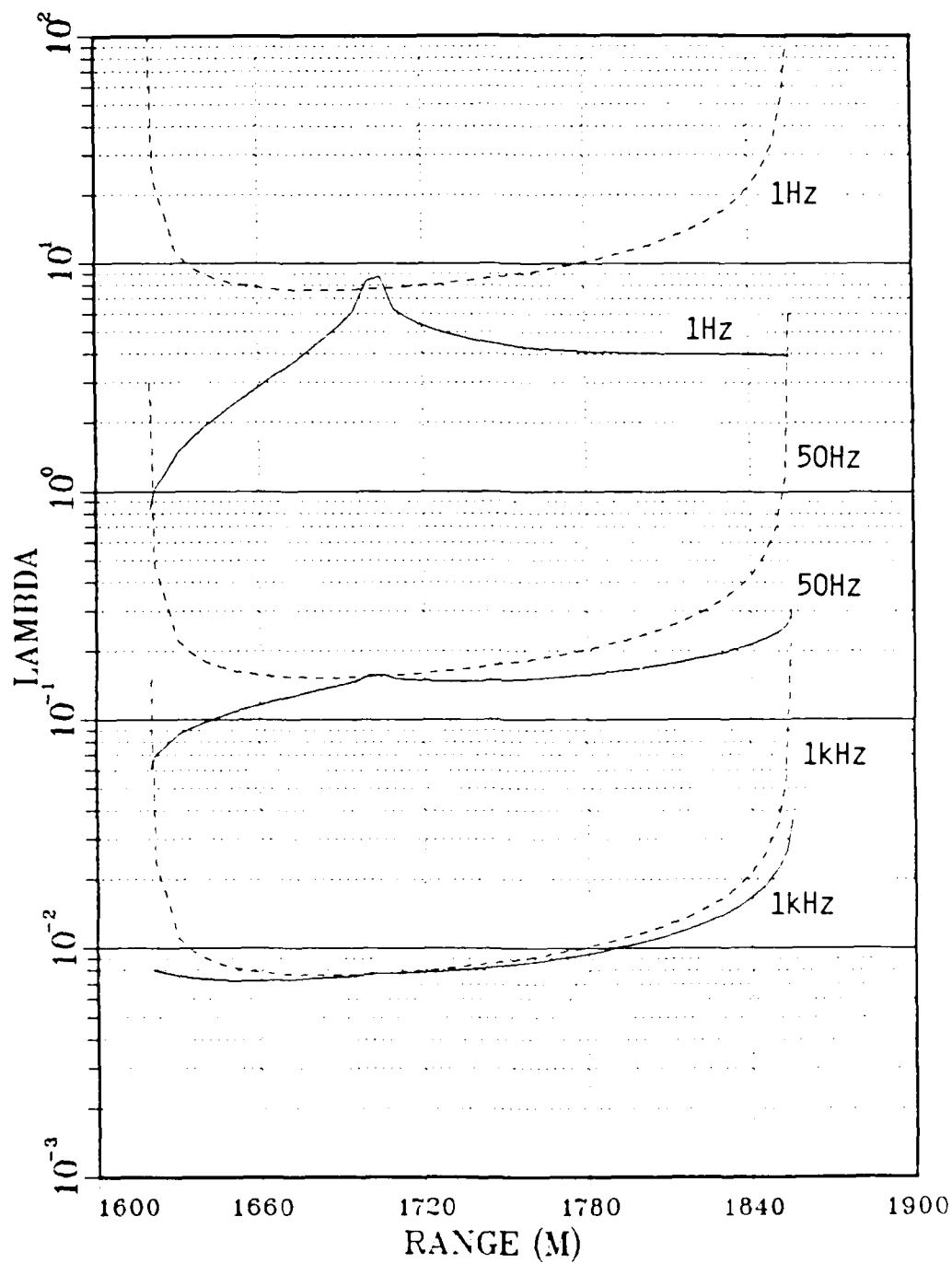


Figure 42. Fluctuation diffraction parameter Λ computed by standard form (----) and by caustic-extended calculation (—).

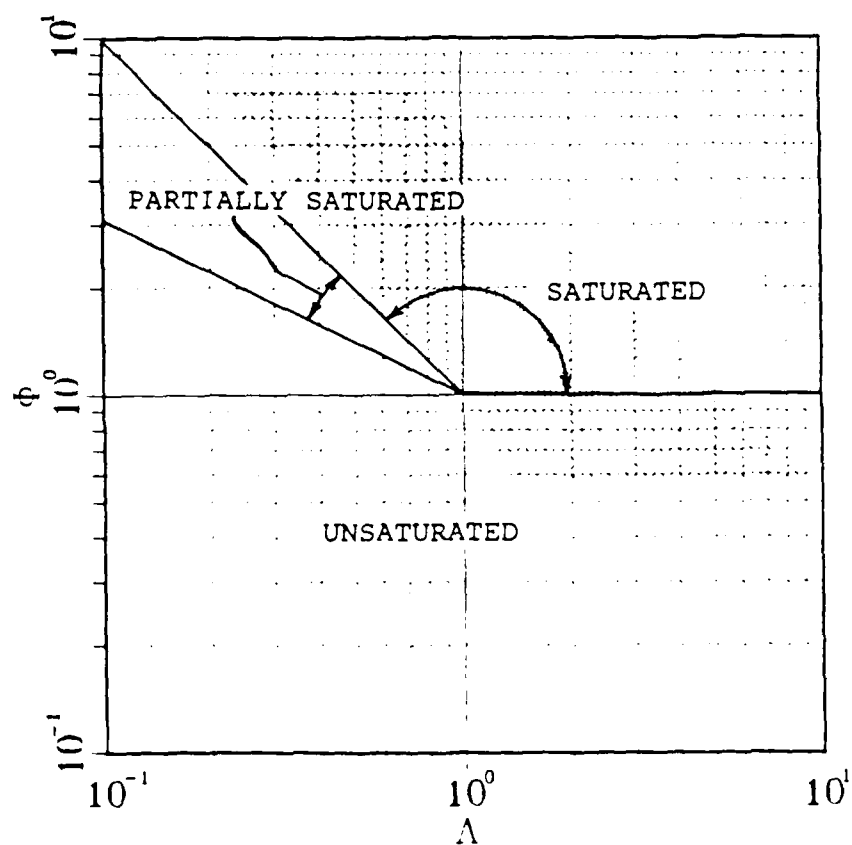


Figure 43. $\Lambda - \Phi$ space showing range of fluctuation parameters encountered in this investigation (shaded area).

nal fluctuation. The area marked "unsaturated" indicates that the received signal is dominated by phase fluctuations rather than amplitude fluctuations and that an increase in perturbation level will increase the signal variability. In this region and below $\mathcal{A} = 1$, the ray path is well represented by a single, displaced path (again, if the propagation in general can be adequately described by ray theory). Above $\mathcal{A} = 1$, the effects are primarily diffractive: a single displaced path could not be identified.

The region labelled "partially saturated" represents ray displacements less than the vertical correlation length of the perturbations. Hence, there is partially correlated multipath. In the "saturated" region, the signal fluctuation level should be roughly constant regardless of the amplitude of the perturbations. The multiple paths are completely uncorrelated.

Overlaid on this diagram is a shaded area that represents the range of \mathcal{A} and \mathcal{F} that are encountered in the illuminated region between the ascending and connecting limbs of the caustic (see Figure 15). According to the \mathcal{A} - \mathcal{F} theory, then, the range of parameters for this investigation encompasses the transition from unsaturated diffractive fluctuation through partial saturation to full saturation. Therefore, we can expect to see significant phase fluctuations at low frequency (2 to 5Hz) and significant amplitude fluctuations at high frequency (10 to 25Hz). This is qualitatively consistent with the behavior of the fluctuations seen in the previous sections but the 20Hz fluctuations are only just saturated whereas the \mathcal{A} - \mathcal{F} calculation predicts saturation above 5Hz.

These predictions based on \mathcal{A} - \mathcal{I} theory should be tempered by the fact that ray theory is assumed to be adequate for describing the unperturbed propagation. At the frequencies of interest here, this assumption is probably a poor one. For example, the calculated values of the displacement distance R for the perturbed ray path are often so large that the path type would change completely before destructive interference could take place: the calculation of R based on small vertical displacements can be in considerable error.

Chapter VIII

CONCLUSIONS

Many of the characteristics of a convergent and strongly diffractive field have been identified in the preceding analysis. Clearly, when the wavelength is of the same order as the characteristic dimensions of the region of convergence, the field must be treated as a wave field. Consequently, a number of wave theory techniques have been used to analyze both the steady-state and the fluctuating nature of this field. In this final chapter, the conclusions are summarized in three groups: one covering the actual calculation of strongly diffractive fields, another covering the structure of the unperturbed wave field, and a third that covers the perturbation-induced fluctuations.

Several methods are used to calculate the pressure distribution in the focused field. Except for some modifications to expedite the mode eigenvalue search, the normal-mode solution is a standard technique. Two other methods are introduced in this work. These are: a finite-difference solution of the time-dependent wave equation for acoustics and a second-order asymptotic correction to ray theory. Concerning all of the methods used, the following points are significant:

1. The finite-difference technique is useful particularly for range-dependent problems; however, it is limited to low frequency by cost and computer storage requirements. Design criteria are outlined in section 5.4. As formulated here, the technique has no

numerical dissipation and limited, isotropic dispersion error. Also, it is developed for two-dimensional Cartesian coordinates although there is no inherent difficulty in modifying the technique for axisymmetric cylindrical coordinates.

2. The second-order asymptotic correction to ray theory given by Equation (2.31) properly predicts the field structure in the vicinity of two closely spaced caustics at the upper frequency limit of this strong diffraction regime. The procedure could be extended to any analysis in which an integral representation has three saddle points in close proximity. (The standard caustic correction applies to two neighboring saddle points, each saddle point corresponding to a classical ray.)
3. Different components of the field can be identified by examining the mode sum while, at the frequencies considered here, the ray picture is of very limited value even with simple asymptotic (caustic) correction.

Ray theory normally gives a reasonable representation, at least qualitatively, of the sound field from a point source in an inhomogeneous medium. In this study, however, the wavelength is of the same order as the separation of the ray-theory caustics and so diffractive interference plays a controlling role. Over this regime of strong diffraction, these conclusions are relevant:

1. Shadow zones have definite interference structure. While no rays are predicted at all by ray theory, there actually are contributions from the diffractive spreading of several classical rays

according to the spreading factor in Equation (2.21) and a contribution from the evanescent "tails" of the lowest-order modes.

2. Multiple caustics blend into a smooth, featureless enhancement. In spite of the classical prediction of three rays in the interior of this region, there is only one distinct wave component besides the weak contribution from the direct path. The point at which the multiple caustic structure will start to be observed can be predicted by the results of the second-order asymptotic correction through Equation (2.33) for the X parameter approximately equal to -4 .
3. The structure of the overall field is determined by the interference of distinct mode groups and these groups retain their identity over some finite spatial scale. It is the proper identification of these groups that leads to correct interpretation of the field as well as providing a basis for understanding signal fluctuations. These structural details were discussed at length in Chapter VI.

The perturbations introduced into the planetary boundary layer model do not lend themselves to asymptotic treatment for two reasons: first, there is significant variation in the perturbation function over a wavelength; and, second, the perturbation strength includes the critical region of transition into saturation. Consequently, not only must the deterministic field be analyzed with due regard to wave phenomena; the diffraction effects introduced by the perturbations must also be considered. Regarding the perturbation-induced signal fluctuations, the following conclusions can be drawn:

1. The response of the field to perturbations is related to two features of the unperturbed field: the number of dominant components or mode groups (for example, one major group and the direct path in the inter-caustic zone), and the relative excitation of these groups as given by the mode amplitudes.
2. The specific influence of a given perturbation function is related to that function's Fourier expansion as a series of mode eigenfunctions. The expansion coefficients given by Equation (3.25) determine the allowable phase shift of the mode groups.
3. A simple, two-component model of the fluctuation mechanism (see Equation (7.8)) produces as accurate an estimate of the fluctuation magnitude below saturation as a complete perturbed-mode solution. One component is identified by the peak in the perturbation weight curve while the other comprises the remainder of the mode sum. The magnitude of the components can be calculated from the appropriate partial sum of the unperturbed modes and the relative phase shift is given by the peak value of the perturbation weight function.
4. The onset of saturation is determined by the frequency (or range) at which the perturbation weight function becomes unity for some mode. However, at the onset, the fluctuation magnitude can be well below the usual limit of 0.52 if the components are unequal in magnitude. Beyond saturation, the two-component model loses validity.
5. The signal amplitudes in the shadow zone are subject to severe fading because of the multi-component structure there. Also

there are strong variations in the field levels with position.

(See Chapter VI.)

6. The presence of a single dominant mode group in the strong enhancement region between caustics means that, at the higher frequencies, the fluctuation magnitude is lower than near the edges or outside of that region.
7. Any range dependence in the fluctuation magnitude is masked by the effects of the rather rapid spatial changes in field structure.

While a number of important results concerning strong diffraction have been obtained, many areas for additional work have become apparent. For example, this investigation has examined only amplitude fluctuations. It would be useful to study phase fluctuation characteristics below saturation; the two-component model is well suited to this. Also, there is significant interest in the inversion of acoustic data to determine physical properties of the medium. The effects of both amplitude and phase fluctuations on these inversion processes should be examined.

Several improvements in and extensions of the solution techniques are suggested. The method for handling the range variation in perturbations is rather crude; this should be improved, if possible. Also, for frequencies somewhat higher than those considered here, a useful ray model could be constructed using the second-order asymptotic correction so that multiple caustics as well as cusps in caustics could be treated. Finally, since the utility of the finite-difference model in two-dimen-

sional Cartesian coordinates has been demonstrated, it should be reformulated in axially symmetric cylindrical coordinates.

Hopefully, this investigation will provide the ground work for additional research into the mechanisms and effects of strong diffraction.

REFERENCES

- Abramowitz, Milton and Irene Stegun, Handbook of Mathematical Functions, Dover Publications, NY, 1965.
- Alterman, Z. and F. Karal, "Propagation of elastic waves in layered media by finite difference methods," Bull. Seism. Soc. Am. 58, 367, 1968.
- Andersen, A. H. and A. C. Kak, "Digital ray tracing in two-dimensional refractive fields," J. Acoust. Soc. Am. 72, 1593, 1982.
- Bedard, A. J. and G. E. Greene, "Case study using arrays of infrasonic microphones to detect and locate meteors and meteorites," J. Acoust. Soc. Am. 69, 1277, 1981.
- Beer, Tom, Atmospheric Waves, Wiley and Sons, NY, 1974.
- Biot, M. A. and I. Tolstoy, "Formulation of wave propagation in infinite media by normal coordinates with an application to diffraction," J. Acous. Soc. Am. 29, 381, 1957.
- Brekhovskikh, L. M., Waves in Layered Media, 2nd ed., Academic Press, NY, 1980.
- Brekhovskikh, L. M. and Y. Lysanov, Fundamentals of Ocean Acoustics, Springer-Verlag, NY, 1982.
- Brown, E. H. and S. F. Clifford, "On the attenuation of sound by turbulence," J. Acoust. Soc. Am. 60, 788, 1976.
- Brown, J. D., "Continuation of wind profile measurements at the Mod-1 site, Boone, NC," Final Report B-93472-A-P, Solar Energy Research Institute, Golden, Colo., 1980.
- Bucker, Homer P., "Sound propagation in a channel with lossy boundaries," J. Acoust. Soc. Am. 48, 1187, 1970.
- Butler, D. S., "The numerical solution of hyperbolic systems of partial differential equations in three independent variables," Proc. Roy. Soc. A255, 232, 1960.
- Chernov, L. A., Wave Propagation in a Random Medium, (trans. by R. A. Silverman), McGraw-Hill, NY, 1960.

- Cooney, P. J., E. P. Kanter, and Z. Vager, "Convenient numerical technique for solving the one-dimensional Schrodinger equation for bound states," *Am. J. Phys.* 49, 76, 1981.
- Courant, R., K. Friedrichs and H. Lewy, "On the partial difference equations of mathematical physics," (trans. from *Math. Ann.* 100, 32, 1928, by Phyllis Fox), Report NYU-7689, Institute of Mathematical Sciences, New York University, 1956.
- Ewing, W. M., W. Jardetzky, and F. Press, Elastic Waves in Layered Media, McGraw-Hill, NY, 1957.
- Flatte, S. M. (ed), Sound Transmission through a Fluctuating Ocean, Cambridge University Press, Cambridge, 1979.
- Fraser, A. B., and W. H. Mach, "Mirages," *Sci. Amer.* 234, 102, 1976.
- Gabrielson, T. B., "Impulse response of the ocean floor: mathematical modeling," Naval Air Development Center Technical Report NADC-82254-30, April 1983.
- Gradshteyn, I. S. and I. W. Ryzhik, Tables of Integrals, Series and Products, Academic Press, NY, 1965.
- Guthrie, K. M., "The propagation of SOFAR signals," PhD Thesis, University of Auckland, 1974.
- Ingard, U. and G. C. Maling, Jr., "On the effect of atmospheric turbulence on sound propagation over the ground," *J. Acoust. Soc. Am.* 35, 1056, 1963.
- Kelley, Neil D., "Acoustic noise generation by the DOE/NASA Mod-1 wind turbine," Wind Turbine Dynamics Workshop, Cleveland, Ohio (24-26 Feb 1981), NASA Conference Publication 2185, 1981.
- Kelley, N. D., R. R. Hemphill and H. E. McKenna, "A methodology for assessment of wind turbine noise generation," *J. Solar Energy Engineering ASME* 104, 112, 1982.
- MacCormack, R. W., "Numerical solution of the interaction of a shock wave with a laminar boundary layer," in *Proc. 2nd Inter. Conf. on Numerical Methods in Fluid Dynamics* (M. Holt, ed.), Lecture Notes in Physics 8, Springer-Verlag, NY, 1970.
- Milder, D. M., "Ray and wave invariants for SOFAR channel propagation," *J. Acoust. Soc. Am.* 46, 1259, 1969.
- Moretti, G., "The λ -scheme," *Computers and Fluids* 7, 191, 1979.
- Panofsky, H. A., and J. A. Dutton, Atmospheric Turbulence, Wiley-Interscience, NY, 1984.

- Pearcey, T., "The structure of an electromagnetic field in the neighborhood of a cusp of a caustic," *Philos. Mag.* 37, 311, 1946.
- Pierce, Allan D., "Extension of the method of normal modes to sound propagation in an almost-stratified medium," *J. Acoust. Soc. Am.* 37, 19, 1965.
- Porter, Michael and Edward L. Reiss, "A numerical method for ocean-acoustic normal modes," *J. Acoust. Soc. Am.* 76, 244, 1984.
- Reynolds, A. C., "Boundary conditions for the numerical solution of wave propagation problems," *Geophysics* 43, 1099, 1978.
- Roth, S. David, "Acoustic propagation in the surface layer under convectively unstable conditions," Final Report to USDA Forest Service (Grant 23-513), The Pennsylvania State University, 1983.
- Sachs, D. A. and A. Silbiger, "Focusing and refraction of harmonic sound and transient pulses in stratified media," *J. Acoust. Soc. Am.* 49, 824, 1971.
- Schlichting, H., Boundary-Layer Theory, McGraw-Hill, NY 1979.
- Skudrzyk, Eugen, "Scattering in an inhomogeneous medium," *J. Acoust. Soc. Am.* 29, 50, 1957.
- Tappert, F. D., "The parabolic equation approximation method," in Wave Propagation and Underwater Acoustics, (ed. J. B. Keller and J. S. Papadakis), Springer-Verlag, NY, 1977.
- Tatarskii, V. I., Wave Propagation in a Turbulent Medium, (trans. R. A. Silverman), McGraw-Hill, NY, 1967.
- Tatarskii, V. I., The Effects of a Turbulent Atmosphere on Wave Propagation, trans. and publ. by the Israel Program for Scientific Translation, Ltd., Jerusalem, 1971.
- Tempest, W., Infrasound and Low Frequency Vibration, Academic Press, London, 1976.
- Tennekes, H. and J. L. Lumley, A First Course in Turbulence, MIT Press, Cambridge, Mass., 1972.
- Thomson, Dennis W., "Analysis and modeling of atmospheric propagation of acoustic noise emitted by the Mod-1 wind turbine," Report to the Solar Energy Research Institute (Contract XE-1-1138-1), The Pennsylvania State University, 1983.
- Thomson, Dennis W., personal communication, 1984.
- Urlick, R., J., Sound Propagation in the Sea, Government Printing Office, Washington, 1979.

- Vichnevetsky, R. and J. Bowles, Fourier Analysis of Numerical Approximations of Hyperbolic Equations, SIAM, Philadelphia, 1982.
- von Mises, R., Mathematical Theory of Compressible Fluid Flow, Academic Press, NY, 1958.
- von Neumann, J. and R. D. Richtmyer, "A method for numerical calculation of hydrodynamic shocks," J. Appl. Phys. 21, 232, 1950.
- Weber, Mark E. and William L. Donn, "Ducted propagation of Concorde-generated shock waves," J. Acoust. Soc. Am. 71, 340, 1982.

Appendix A

TRANSPARENT-BOUNDARY CONDITION

Reynolds (1978) gives a finite-difference approximation for a nonreflecting boundary (i.e., completely transmitting boundary) by factoring the differential operator of the wave equation and then searching for a weighted-difference scheme that minimizes the reflection coefficient over some range of incident angle. The condition at the lower boundary ($y = 0$) is given by

$$p'_{11} = (1 - q)(p^o_{11} - p^{-1}_{12}) + (1 + q)p^o_{12} - qp^{-1}_{13} \quad . \quad (A.1)$$

At $y = Mh$ (the upper boundary) the condition is

$$p'_{1M} = (1 - q)(p^o_{1M} - p^{-1}_{1,M-1}) + (1 + q)p^o_{1,M-1} - qp^{-1}_{1,M-2} \quad . \quad (A.2)$$

The notation here corresponds to that of section 3.1.3.

Appendix B

GRADIENT SCALING

By compressing the horizontal scale of the finite-difference grid while maintaining the vertical scale, the efficiency of the numerical solution can be improved. The horizontal scale change is given by the change in range between a ray that vertexes at some depth before scaling and the ray that vertexes at the same depth after scaling.

For a constant sound-speed gradient g , the range to a vertex is

$$x = \sqrt{c_v^2 - c_o^2} / g, \quad (B.1)$$

where c_v is the vertex speed of the ray. If the sound-speed profile is adjusted so that

$$\tilde{c}_1 = c_o + \alpha(c_1 - c_o), \quad (B.2)$$

then the gradient is scaled by

$$\tilde{g} = \alpha g, \quad (B.3)$$

and

$$\tilde{x} = \sqrt{[c_0 + \alpha(c_v - c_0)]^2 - c_0^2} / \alpha g \quad . \quad (B.4)$$

For c_v approximately equal to c_0 as would be the case in the atmosphere or the ocean for low angle rays

$$\tilde{x} \simeq x / \sqrt{\alpha} \quad . \quad (B.5)$$

Thus, the desired range scale factor is computed from Equation (B.5) and applied to the profile according to Equation (B.2).

The perturbations must also be scaled so as to retain the same root-mean-square phase change over equivalent distances. This phase change is directly proportional to range so the perturbation amplitude must be multiplied by $\sqrt{\alpha}$.

FILMED
0-8